

# Institute of Experimental and Applied Physics

University of Kiel

## Solar Wind Heavy Ion Measurements with SOHO/CELIAS/CTOF

Master Thesis

Nils Peter Janitzek

Matriculation Number: 901905

**Supervisor** Prof. Dr. Wimmer-Schweingruber  
**First Investigator** Prof. Dr. Wimmer-Schweingruber  
**Second Investigator** Prof. Dr. Bonitz

## ABSTRACT

Solar wind ions with an atomic number  $Z > 1$  are referred to as heavy ions which, with the exception of helium, represent a fraction of less than 1% of all solar wind ions and therefore can be regarded as test-particles, only reacting to but not driving the dynamics of the solar wind plasma. Therefore they are considered as perfectly suited diagnostic tool for plasma wave phenomena both in the solar atmosphere and the extended heliosphere. The presence of a systematic velocity difference between heavy ions and the solar wind bulk protons, called differential streaming, is anticipated with the presence of ion-cyclotron waves which both accelerate and heat the heavy ions preferentially and might play a key-role in coronal heating processes, which are still not well understood. In this work we investigate the differential streaming of oxygen, silicon and iron ions measured with the Charge Time-OF-Flight (CTOF) sensor of the Charge, EElement and Isotope Analysis System (CELIAS) aboard the SOlar and Heliospheric Observatory (SOHO) situated at the Lagrange Point L1. The CTOF instrument is a Time-of-Flight mass spectrometer which measures heavy ions in the energy-per-charge range between 0.3 and 34.7 keV/nuc and is able to determine the ion's mass, charge and velocity parallel to the spacecraft-sun connection line. Due to its high geometry factor the measurement of heavy ion 1d velocity distributions can be conducted with an unprecedented cadence of 5 minutes. In this thesis an in-flight calibration of the CTOF sensor is performed characterizing the instrument response to all relevant solar wind ions. In particular a sophisticated response model for iron ions is developed. Furthermore two different methods for the count rate analysis are presented and are compared for the case of iron ions. We finally find evidence for differential streaming up to 40-50 km/s in the fast solar wind for all investigated ions, which are  $O^{6+}$ ,  $Si^{7+}$ ,  $Fe^{8+}$ ,  $Fe^{9+}$ , and  $Fe^{10+}$ . This result is in good agreement with studies of Berger et al. (2011) and Ipavich et al. (1986). However it contradicts a former study by Hefti et al. (1998) also conducted with CTOF but based on on-board post-processed data which was found to be less accurate than the raw PHA data, which we used in this work.

## ZUSAMMENFASSUNG

Sonnenwindionen mit einer Kernladungszahl  $Z > 1$  werden als Schwere Ionen bezeichnet. Mit Ausnahme von Helium stellen sie einen Anteil von weniger als 1% aller Ionen im Sonnenwind, weshalb sie als Testteilchen betrachtet werden können, die zwar auf die Dynamik des Sonnenwindplasmas reagieren, diese aber nicht nennenswert beeinflussen. Daher stellen sie ein sehr gut geeignetes Diagnostik-Werkzeug für Plasmawellenphänomene dar, sowohl in der Sonnenatmosphäre als auch in der gesamten Heliosphäre. Die Existenz einer systematischen Geschwindigkeitsdifferenz zwischen Schweren Ionen und den Sonnenwindprotonen, die als Differentielles Strömen bezeichnet wird, wird mit der Anwesenheit von Ion-Zyklotron Wellen in Verbindung gebracht, welche die Schweren Sonnenwindionen sowohl beschleunigen als auch heizen und die eine Schlüsselrolle für Koronale Heizprozesse spielen könnten, welche noch immer nicht vollständig verstanden sind. In dieser Arbeit untersuchen wir das Differentielle Strömen von Sauerstoff-, Silizium- und Eisen-Ionen, die mit dem Charge Time-OF-Flight (CTOF) Sensor des Charge, EElement and Isotope Analysis Systems (CELIAS) an Bord des SOlar and Heliospheric Observatory (SOHO) gemessen wurden, welches sich am Lagrangepunkt L1 befindet. Das CTOF Instrument ist ein Flugzeit-Massen-Spektrometer, das die Schweren Ionen im Energie-pro-Ladung-Bereich zwischen 0.3 and 34.7 keV/nuc misst und in der Lage ist, die Ionenmasse, Ionenladung und Ionengeschwindigkeit parallel zur Verbindungsleitung Sonde-Sonne zu bestimmen. Aufgrund seines hohen Geometriefaktors ist die Messung der 1d-Geschwindigkeitsverteilungen von Schweren Ionen mit einer nie zuvor erreichten Kadenz von 5 Minuten möglich. In dieser Arbeit wird eine In-Flight Kalibrierung des CTOF Sensors durchgeführt, die die Instrumentantwort für alle relevanten Sonnenwindionen charakterisiert. Insbesondere wird ein ausgefeiltes Modell für die Antwort der Eisen-Ionen entwickelt. Weiterhin werden zwei verschiedene Modelle für die Zählratenanalyse vorgestellt und für die Eisen-Ionen verglichen. Abschließend finden wir ein Differentielles Strömen von bis zu 40-50 km/s im schnellen Sonnenwind für alle untersuchten Ionen. Diese sind im Einzelnen  $O^{6+}$ ,  $Si^{7+}$ ,  $Fe^{8+}$ ,  $Fe^{9+}$  und  $Fe^{10+}$ . Dieses Ergebnis ist in guter Übereinstimmung mit den Studien von Berger et al. (2011) und Ipavich et al. (1986). Es steht jedoch im Widerspruch zu einer Studie von Hefti et al. (1998), welche ebenfalls mit dem CTOF Sensor durchgeführt wurde, welche allerdings auf an-Bord nachverarbeiteten Daten basiert, die sich als weniger genau als die hier verwendeten unverarbeiteten PHA Daten herausstellten.

# Contents

<b>1</b>	<b>Theoretical Background</b>	<b>1</b>
1.0.1	Solar Wind Investigation History and Composition . . . . .	1
1.0.2	Fast and Slow Solar Wind . . . . .	2
1.0.3	The Interplanetary Magnetic Field . . . . .	2
1.0.4	Scientific Interest of Heavy Ions: Differential Streaming . . . . .	4
1.0.4.1	Resonant Wave-Particle Interaction . . . . .	6
1.0.4.2	Measuring the Differential Streaming of Heavy Ions with High-Time Resolution . . . . .	9
1.1	Measurement of Heavy Ions with a Solid State Detector . . . . .	10
1.1.1	Physics of a Solid State Detector . . . . .	10
1.1.2	SRIM Simulation Package . . . . .	13
<b>2</b>	<b>The CELIAS Experiment aboard SOHO</b>	<b>14</b>
2.1	The Solar and Heliospheric Observatory . . . . .	14
2.2	The CELIAS Experiment . . . . .	14
<b>3</b>	<b>The CELIAS/CTOF Sensor</b>	<b>17</b>
3.1	Principle of Operation . . . . .	17
3.2	CTOF Data . . . . .	21
<b>4</b>	<b>In-Flight-Calibration of the CTOF-Sensor</b>	<b>23</b>
4.1	Time-of-Flight Calibration for Solar Wind Ions . . . . .	23
4.1.1	Selection of the Reference Ions . . . . .	24
4.1.2	Fit of the Reference Ions . . . . .	25
4.1.3	Calculation of the ToF Peak Positions with TRIM . . . . .	29
4.1.4	Calibration of the ToF Peak Widths . . . . .	34
4.2	Solid State Detector Calibration for Solar Wind Ions . . . . .	37
4.2.1	SSD Calibration Model . . . . .	37
4.2.2	Simulation of the Energy Peak Positions with TRIM . . . . .	38
4.2.2.1	Total Ionization Loss of Ions in the Silicon Layer . . . . .	38
4.2.2.2	Simulation of the SSD Dead-Layer . . . . .	43
4.2.2.3	Influence of Carbon Foil and Entrance System on the SSD Signal . . . . .	46
4.2.3	SSD Simulation Results . . . . .	48
4.2.3.1	Comparison with Pre-flight Calibration Data . . . . .	52
4.2.4	SSD Calibration Results . . . . .	54
4.2.5	Calibration of the Energy Peak Widths . . . . .	57
4.3	An Improved Peak Shape Model for Iron Ions . . . . .	58

4.3.0.1	Parametrization of the Peak Width Parameters for Iron Ions . . . . .	61
<b>5</b>	<b>Data Analysis</b>	<b>64</b>
5.1	Count Rate Analysis with Box Rates . . . . .	64
5.2	Count Rate Analysis with Poisson-Fits . . . . .	67
<b>6</b>	<b>Results</b>	<b>72</b>
6.1	Differential Streaming of Heavy Ions Derived from Box Rates . . . . .	72
6.2	Differential Streaming of Iron Ions Derived from Poisson-Fits . . . . .	77
<b>7</b>	<b>Discussion and Conclusions</b>	<b>82</b>
<b>A</b>	<b><i>SRIM/TRIM Tables and Plots</i></b>	<b>87</b>
<b>Bibliography</b>		<b>93</b>
<b>Acknowledgements</b>		<b>97</b>

# Chapter 1

## Theoretical Background

### 1.0.1 Solar Wind Investigation History and Composition

The first widely noticed postulation of a continuous plasma stream released from the Sun was made by Biermann in the early 1950s [1] in order to explain the observations of cometary tails pointing radially away from the Sun. Experimental evidence for the theory was given a decade later in the 1960s by the first in-situ measurements of the solar wind by the Russian Luna 2 spacecraft [2]. Shortly thereafter Neugebauer and Snyder [3],[4] found from measurements of the Mariner 2 spacecraft that beside electrons and protons which represent about  $\sim 95\%$  of all solar wind ions there exists a significant  $\text{He}^{2+}$  component in the wind which accounts for the remaining 5%. The discovery of other elements than hydrogen and helium in the solar wind was then made in 1968 by Bame et al. [5] of the Los Alamos Group who found oxygen ions measured by the Vela satellites. In the following Geiss et al. developed the famous solar wind trapping experiment [6], [7], which was performed by astronauts of the Apollo 11 mission who deployed an aluminium foil on the lunar surface and returned it to Earth for composition analysis. The experiment led to the discovery of several noble gases up to xenon, however in negligible proportion to helium and hydrogen. Today there exists evidence for a number of further elements in the solar wind such as C, N, Mg, Si, S, and Fe which could be also observed with remote sensing instruments on the SOHO spacecraft [8]. SOHO also found traces of P, Ti, Cr and Ni [9]. However, all these elements on the whole account for a fraction of less than 1% of all particles in the solar wind and therefore they are sometimes subsumed under the term *minor ions* [10].

### 1.0.2 Fast and Slow Solar Wind

The solar wind can be divided into two components: slow wind and fast wind. The slow wind is observed from velocities around 300 km/s up to velocities above 400 km/s while the fast wind is measured at velocities around 500 km/s in the ecliptic while even up to more than 800 km/s out of the ecliptic [11], [12]. The two components also have different source regions: The fast wind originates from coronal holes which are regions of open magnetic field lines situated at high latitudes on the quiet Sun while the slow wind originates from low latitudes where the solar magnetic field consists of closed field lines. Therefore, its origin is still under debate while the most promising candidates are the boundaries of coronal holes [13] where the solar wind plasma can be released in the course of reconnection processes in the corona and the edges of active regions [14]. Because in the closed field line structures the coronal electrons can be heated more efficiently the electron temperatures are significantly higher in these regions than in coronal holes lying at  $1.4\text{--}1.6 \cdot 10^6$  K compared to  $8 \cdot 10^5$  K. Therefore, the ionic charge state composition in the slow wind is shifted to higher mean charge states compared to the fast wind [15]. Furthermore also the elemental abundances vary from slow to fast solar wind streams: Even if in both types the elements with low first ionization potential (FIP) are enriched with respect to elements with high FIP compared to photospheric abundances, this effect is stronger by a factor of 2 in the slow solar wind [10]. Since the first ionization energies can be overcome by the kinetic energy of the electrons already at comparably low temperatures the FIP fractionation process is supposed to happen already in the relatively cold solar chromosphere.

### 1.0.3 The Interplanetary Magnetic Field

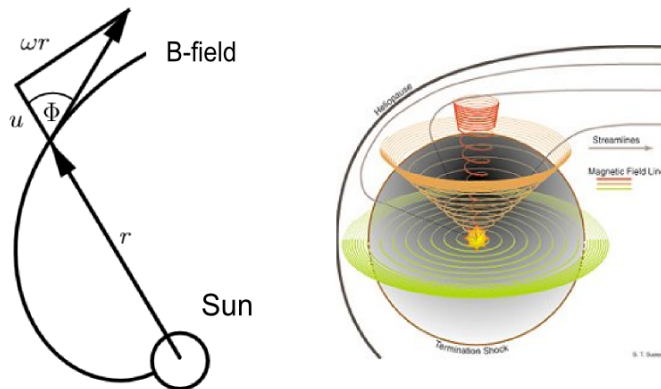


FIGURE 1.1: Simple model of the interplanetary magnetic field within and out of the ecliptic. The pictures are taken from [16], [17].

Despite most of the described features in the previous paragraph, in a first approximation one can see the solar wind as a steady plasma flow and assume that individual plasma "packages" propagate radially away from the Sun at a constant solar wind speed  $v_{sw}$ . The magnetic field lines are frozen-in in the solar wind or in other words the particles carry the field outwards. However, because the Sun is rotating with an angular speed  $\omega \approx 2\pi/T_C$  with reference to the Earth the interplanetary B-field forms an Archimedian spiral [18] as shown in figure 1.1, which is also called Parker Spiral. The angle between the Sun-Earth connection line and the spiral is called Parker angle and can be calculated to

$$\tan(\Phi) = -\frac{\omega r}{v_{sw}} \quad (1.1)$$

which is dependent on the solar wind speed and on the distance to the Sun. For an average solar wind speed  $v_{sw} = 450 \text{ km/s}$  and  $r = 150 \cdot 10^6 \text{ km} = 1 \text{ AU}$  we find a mean Parker angle of  $\sim 43^\circ$  at Earth, as well as at the Lagrange Point L1 which is situated on the Earth-Sun connection line at about  $1.5 \cdot 10^6 \text{ km}$  away from the Earth. Note that the absolute value  $B$  of the interplanetary magnetic field is decreasing with distance to the Sun and at 1 AU we measure values of around 5 nT. Taking into account an average solar wind proton density on the order of  $\rho_N = 5 \text{ cm}^{-3}$  [11] we obtain an Alfvén speed (see Eq. (1.3)) on the order of  $\sim 50 \text{ km/s}$  in the vicinity of the Earth [19]. We finally point out that this simple model does not account for the wide range of dynamics in the solar wind, propagating from the solar atmosphere throughout the heliosphere and also originating from the interplay of slow and fast solar wind as described in the previous paragraph eventually leading to Corotating Interaction Regions (CIRs) nor does it include any interaction with ambient plasma waves. Therefore, the derived quantities such as the direction and absolute value of the B-field, as well as the ambient Alfvén speed are actually highly variable in time.

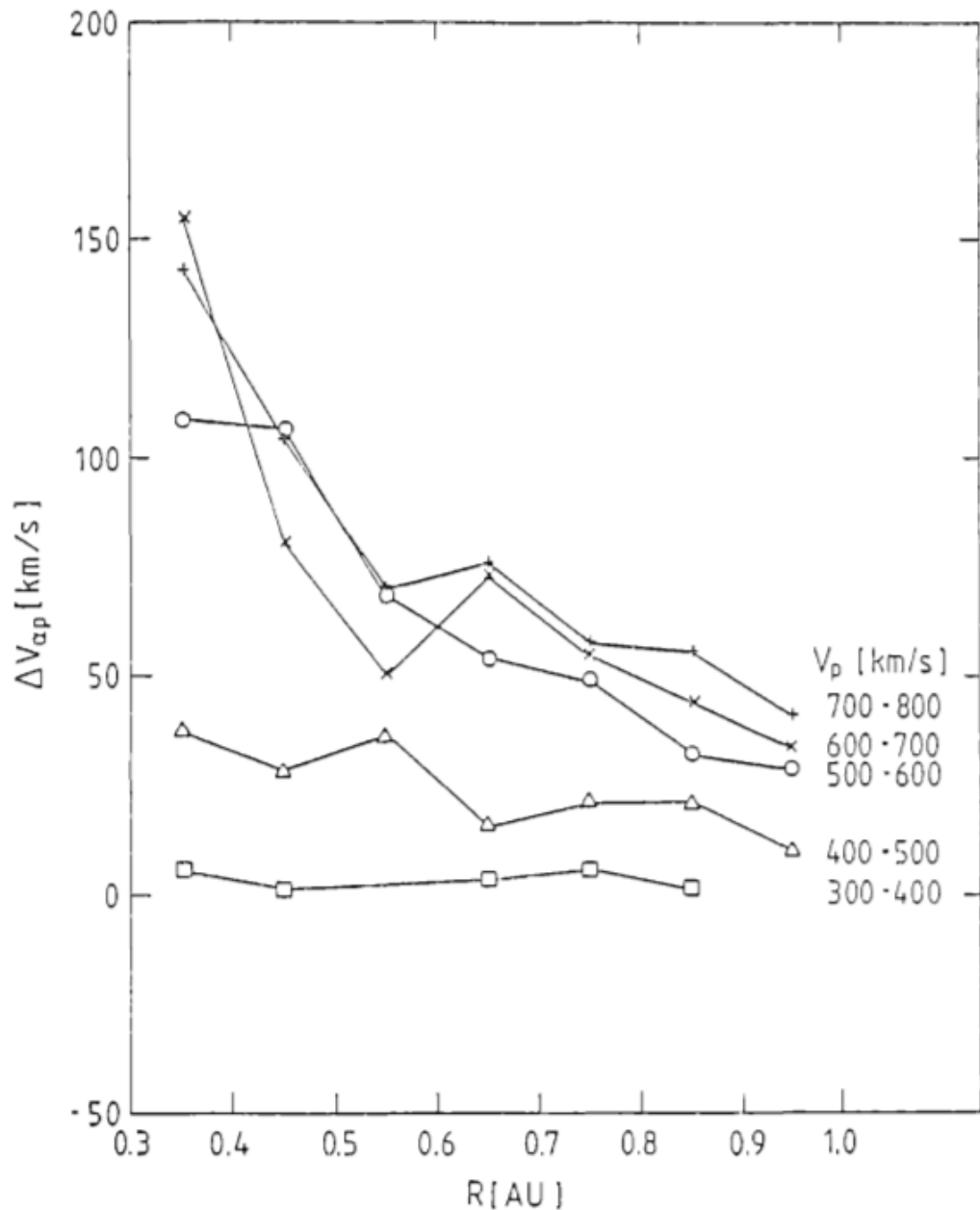


FIGURE 1.2: Differential streaming of helium ions observed with the Helios spacecraft [20] at distances between 0.3 and 1 AU from the Sun.

#### 1.0.4 Scientific Interest of Heavy Ions: Differential Streaming

One of the early observations of a systematic velocity difference between heavy ions and the solar wind bulk protons which we refer to as *differential streaming* was done with the two Helios spacecraft which were in operation from the mid 1970s until 1979 (in the case of Helios B) and 1985 (in the case of Helios A) and which came as close as

0.3 AU to the Sun. As can be seen in figure 1.2 Marsch et al. observed velocity differences between  $\text{He}^{2+}$  and the protons up to 150 km/s in the fast solar wind while in the slow wind they measured differences up to 40 km/s. One recognizes that the observed velocity differences show a strong dependence on the distance to the Sun. From considerations in the next section it can be shown that this dependence is related to the local Alfvén speed which is decreasing with distance to the Sun as the absolute value of the local interplanetary B-field does. However, before going into details we shortly point out the specific interest in the measurement of differential streaming.

As it will be shown in the following section, the presence of a systematic positive ve-

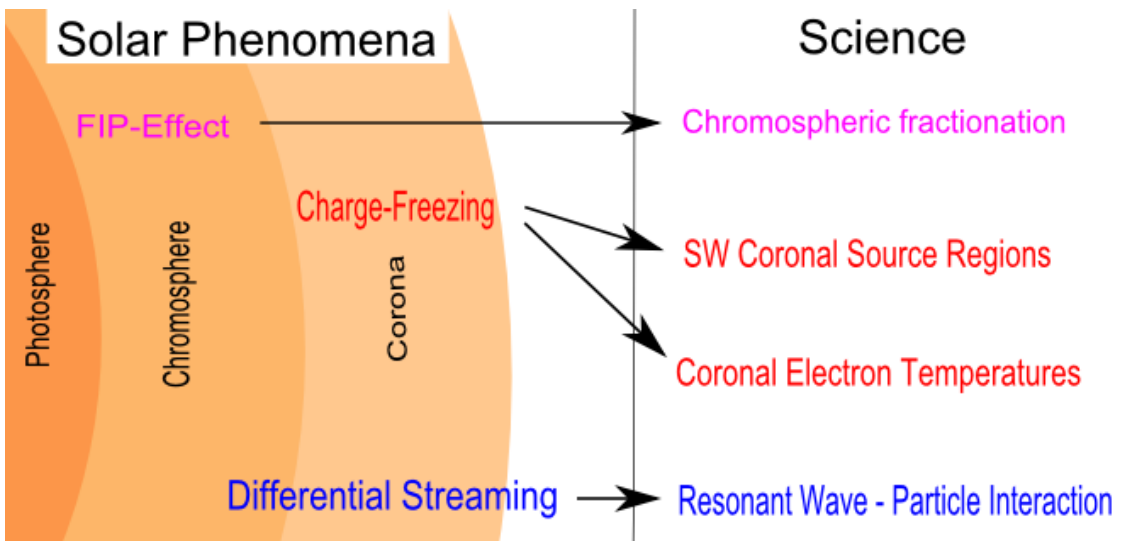


FIGURE 1.3: Solar and heliospheric phenomena which are of scientific interest in the context of solar wind heavy ion measurements. In this thesis we concentrate on differential streaming which is closely linked to resonant wave-particle interactions.

locity difference between solar wind heavy ions and protons can be explained by the preferential acceleration of the first by resonant wave-particle interactions with ion-cyclotron waves originating from instabilities in the solar wind proton stream e.g. from occurring non-Maxwellian shapes of the proton velocity distribution functions (VDF) such as measured in [21]. These ion cyclotron waves which represent the high frequency branch of the Alfvénic mode as shown in figure (1.5) have been suggested by [22],[23] to play a key-role in the heating mechanism of the corona by transporting energy from the flaring magnetic network in the lower solar transition region and efficiently releasing it through rapid dissipation in the corona within a fraction of a solar radius [24]. This idea has been corroborated in a two-fluid turbulence model [25], where the authors also included parametric studies of the wind properties [26] in dependence on the average wave amplitude at the coronal base. However, there is no knowledge about the plasma wave spectra in the corona yet. As a consequence, all models have to make assumptions about the spectrum of the waves injected at the

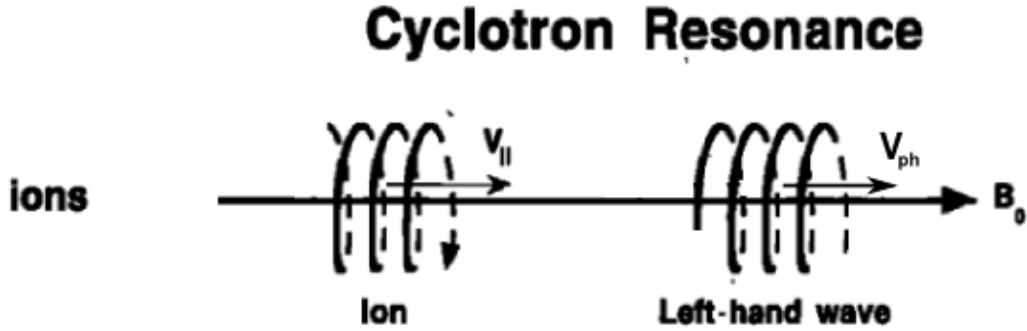


FIGURE 1.4: Resonant interaction between ion-cyclotron waves and solar wind ions after [28].

coronal base for which a power-law is often assumed (see figure (1.6)). The intensity of this spectrum, however, can be constrained from extrapolations of solar wind in-situ measurements [27]. Therefore, the experimental measurements such as the one we are performing with CTOF are not only needed in order to corroborate the presence of relevant wave phenomena in the solar wind but are also necessary to provide constraints on the modeling of the complex processes in the solar atmosphere.

#### 1.0.4.1 Resonant Wave-Particle Interaction

In the dilute solar wind plasma in interplanetary space we can neglect particle collisions, however, there exists the possibility of wave-particle interactions. A special case is the resonant interaction between ions and left-hand polarized ion-cyclotron waves, which in the the solar wind are virtually carried by the bulk protons and we thus explicitly treat proton-cyclotron waves in the following even if there can exist additional waves carried by the alpha-particles. The proton-cyclotron waves can be derived in a magnetized two-fluid plasma model [29] and their dispersion relation can be written in a simplified form as:

$$\frac{k_{\parallel}^2 v_A^2}{\Omega_p^2} = \frac{\omega^2}{\Omega_p(\Omega_p - \omega)} \quad (1.2)$$

where  $k_{\parallel}$  is the wave-vector component parallel to the magnetic field,  $\omega$  is the wave frequency,

$$v_A = \sqrt{\frac{B^2}{\mu_0 \rho}} \quad (1.3)$$

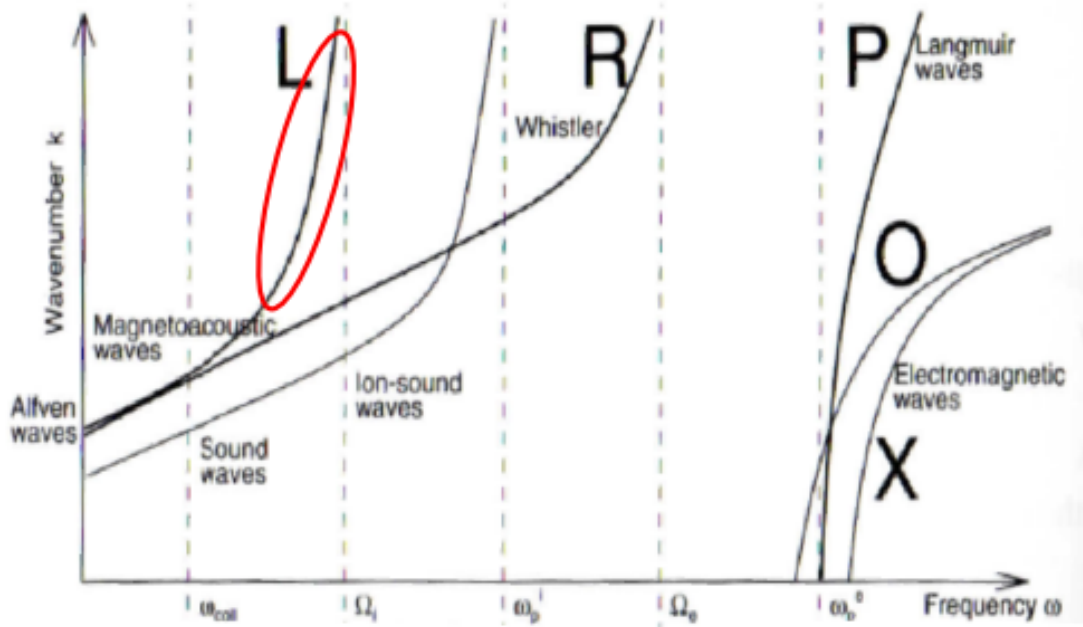


FIGURE 1.5: Dispersion relations for different waves in a magnetized plasma after [30]. The proton cyclotron mode is marked by the red ellipse.

is the local Alfvén speed (which depends on the ambient plasma density  $\rho$ ) and

$$\Omega_p = \frac{q_p B}{m_p} = \frac{eB}{m_p} \quad (1.4)$$

is the proton gyrofrequency. One can immediately see that the expression (1.2) diverges when  $\omega$  approaches  $\Omega_p$  while it becomes the dispersion relation of Alfvén waves

$$k_{\parallel}^2 v_A^2 = \omega^2 \quad (1.5)$$

if  $\omega \ll \Omega_p$ . Therefore, the proton-cyclotron wave can be interpreted as high-frequency mode of the Alfvénic solution, which is illustrated in figure (1.5).

Ions other than protons can now resonantly interact with the proton-cyclotron wave as sketched in figure 1.4, because their gyrofrequencies  $\Omega_i$  are smaller than the proton gyrofrequency due to their larger  $m/q$ -ratio which enables them to fulfill the resonance condition:

$$k_{\parallel} v_{\parallel} - \omega = n \cdot \Omega_i \quad (1.6)$$

where  $n$  is an integer,  $v_{\parallel}$  is the ion's velocity parallel to  $B$  and  $\Omega_i$  is the ion gyrofrequency. For  $n = 1$  the strong interaction is intuitively clear since in its reference frame

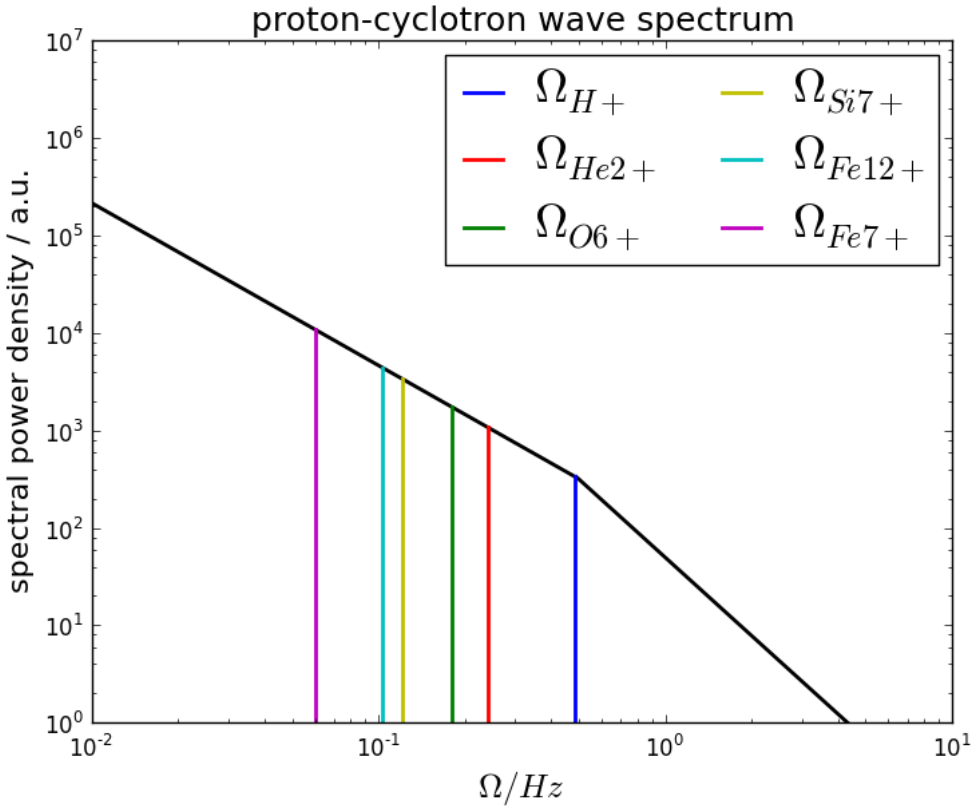


FIGURE 1.6: Example of an assumed proton-cyclotron wave spectrum. Additionally the gyrofrequencies of typical solar wind ions are plotted.

the ion feels a stationary electromagnetic field when gyrating in the same sense and at the same frequency as the electromagnetic field vector of the wave (see figure 1.4). Note that in principle an ion can both lose and gain energy in dependence on the relative orientation of field and ion velocity vector perpendicular to  $B$ , however an ensemble of particles gains energy when having slightly lower kinetic energy whereas it loses energy when it has slightly more energy than the wave. This is due to the fact that the particles of the first ensemble stay longer in the vicinity of the resonance condition when they gain energy compared to those who lose energy and vice versa for particles of the second ensemble. In addition to these considerations one can see from figure 1.6 that if we assume a spectrum which decreases monotonically with frequency, the ions with larger  $m/q$ -ratios can interact with modes of increased power compared to those with small mass-per-charge values. One therefore qualitatively expects them to be preferentially accelerated.

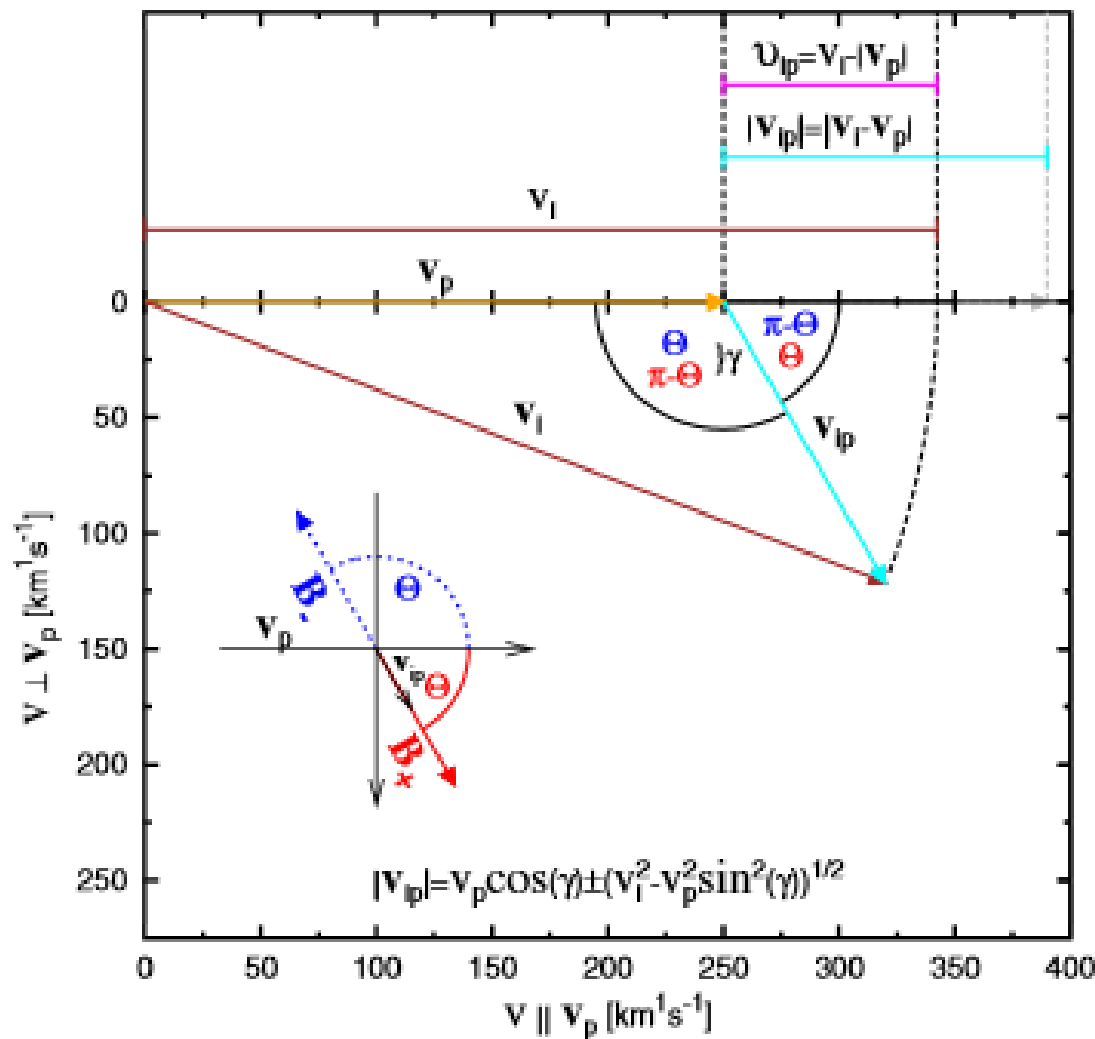


FIGURE 1.7: Relation between the measured (pink) and the actual (cyan) differential streaming in dependence of the ambient magnetic field at the spacecraft site. The picture is taken from [31].

#### 1.0.4.2 Measuring the Differential Streaming of Heavy Ions with High-Time Resolution

Since the solar wind expands radially from the Sun, all solar wind instruments on a 3-axis stabilized spacecraft, as it is the case for the SOlar and Heliospheric Observatory (SOHO), are also pointing radially to the Sun. However, as described in [31] the preferential acceleration of heavy ions acts parallel to the local interplanetary magnetic field and therefore, the differential speed vector is always a tangent to the B-field vector (see figure 1.7), which was derived to be about  $43^\circ$  for an average solar wind speed of 450 km/s at 1 AU. Unfortunately this average angle is meaningless over longer time periods because firstly the solar wind speed in the ecliptic plane varies between  $\sim 300$

and  $\sim 700$  km/s tilting the Parker angle of about 10 degrees but secondly and even more important the B-field direction is varying significantly on minute scale [31] so that one does not only measure a projection of the actual differential streaming but a projection quickly changing with time. To have a chance to correct for these effects one aims to measure with a high time resolution. However, this is difficult to achieve for heavy ion measurements since they are that rare in the solar wind so that the statistics decrease to critically low values. State-of-the-art solar wind instruments like ACE/SWICS are able to measure with a cadence of 5 instrument cycles per hour corresponding to 1 measurement cycle each 12 minutes. The CTOF sensor which is used in this study reaches an unprecedented cadence of 12 instrument cycles per hour corresponding to one cycle each 5 minutes. In order to simplify the writing in the following we synonymously use the term cadence for the time in between two measurement cycles, so that e.g. CTOF measures with 5-minute cadence. The CTOF sensor was already used in an earlier study of solar wind heavy ions by S. Hefti [32], which is shown in figure 1.8. As can be seen from the upper left histogram where the obtained ion velocities are plotted against the measured proton velocity the author finds a positive differential streaming for  $O^{6+}$  but there is no significant differential streaming found for  $Si^{7+}$  and  $Fe^{9+}$  which are (slightly misleading) plotted against  $O^{6+}$  in the upper right and in the lower left panel and against each other in the lower right histogram. However, one has to point out that this study was done with so-called matrix rate data, which are not the raw count rates measured by the sensor but instead these are already on the space-craft post-processed data by an algorithm that automatically distinguishes the different ions from each other based on a few pre-flight calibration measurements and mainly on simulations of the sensor response as described in [33], [34], [35]. Unfortunately, it was later found that the used algorithm is not precise enough to accurately measure the differential streaming of several heavy ions such as e.g. iron ions (L. Berger, H. Gruenwaldt, personal communication: (2014)).

## 1.1 Measurement of Heavy Ions with a Solid State Detector

### 1.1.1 Physics of a Solid State Detector

A solid state detector as sketched in figure (1.9) usually consists of a front contact followed by a p-n junction [36]. The p-n-junction leads to the creation of an electric field due to the diffusion from electrons into the p-region and holes into the n-region. In this context the depletion region is formed (here in the n-region) which is the sensitive volume of the detector and which can be even enlarged when operating the detector in

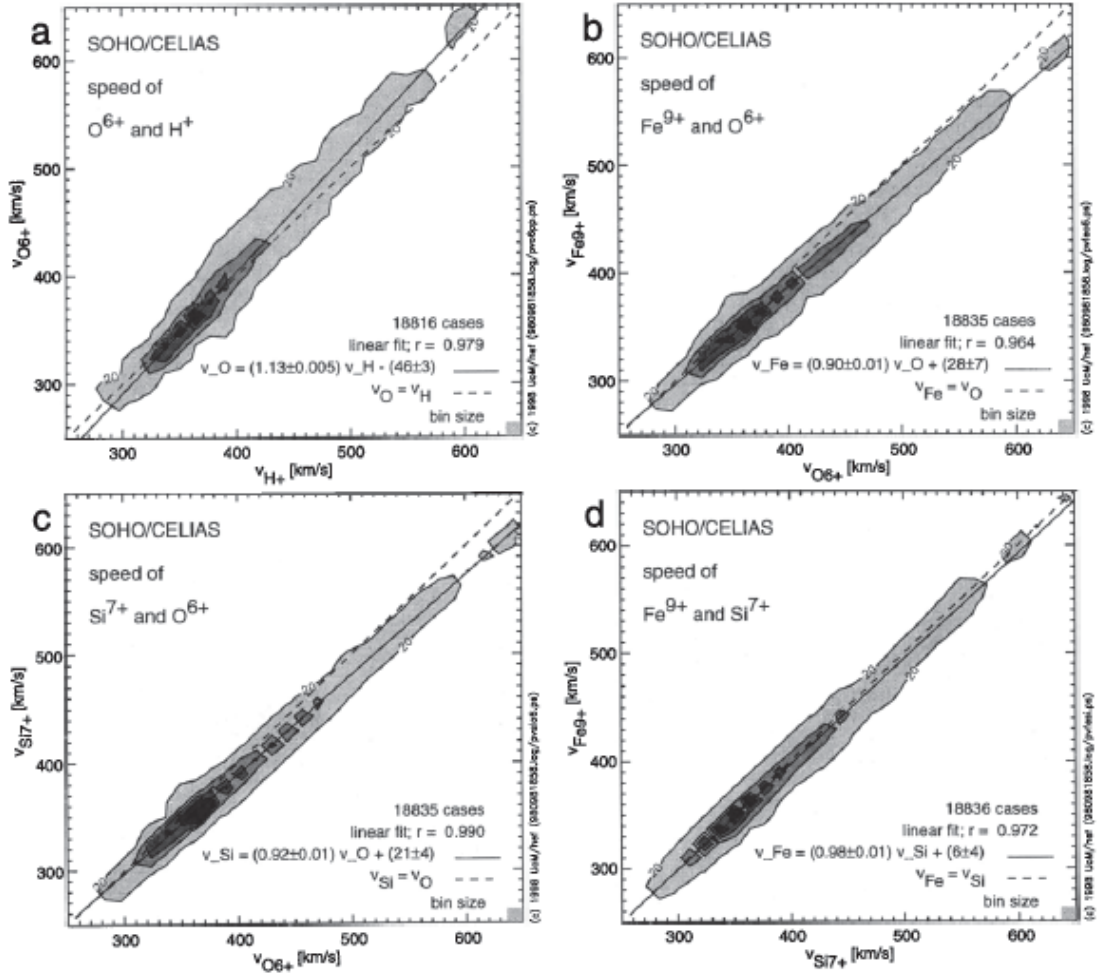


FIGURE 1.8: Differential streaming of  $O^{6+}$ ,  $Si^{7+}$ , and  $Fe^{9+}$  as measured by [32]. Note that only in the upper left panel the ion velocity is plotted against the proton velocity.

In the other 3 panels the different ion velocities are plotted against each other.

bias mode as it is usually done. If now a particle enters the active area of the SSD it can create electron hole pairs which then travel along the electric field and cause a charge pulse in the read-out electronics. However, even if the particle fully stops in the SSD the detected energy in the SSD does not equal the particle's energy before entering the SSD because of two reasons [37] :

- The particle loses energy to the insensitive front contact (dead-layer).
- Only the part of the energy deposit which is spent on the creation of conduction electrons within the SSD depletion region contributes to the measured electronic signal. This part is called *electronic* or *ionization loss*. All other deposited energy going into nuclei lattice vibrations (phonons) via elastic collisions with the SSD nuclei and into structural damage of the SSD is lost for the measurement.

This effect is called *pulse height defect (PHD)* and is also denoted to the lost fraction of the signal. We here refer to its complement  $1 - \text{PHD}$  as *pulse height fraction (PHF)* which we will also denote with  $\eta(Z, v)$  in formulas. The PHD is in principle dependent on both the atomic number of the particle and its velocity but not on the charge of the particle since soon after entering the SSD the particle obtains an equilibrium charge state, called the *effective charge* [38]. Quantitatively speaking the important quantity is the ratio between the particle velocity and the target Fermi velocity [39]: When the incident ion is moving much faster than the fastest target electrons the ion's own co-moving electrons feel a net field from the static target charges and get stripped from the ion. If on the other hand the ion velocity is lower than the Fermi speed, the target electrons can efficiently react to the electronic perturbation of the incident ion and stick to it until we have a neutral atom passing through the target.

Finally we can relate the electronic stopping powers ( $dE/dx_{el}$ ) to the PHF as follows:

$$\eta(Z, v) \cdot E_{in} = E_{SSD} = E_{el}^{ion} + E_{el}^{rec} = \int_{x_0}^{x_{range}} \left( \frac{dE_{el}}{dx} \right)_{ion} dx + \int_{x_0}^{x_{range}} \left( \frac{dE_{el}}{dx} \right)_{rec} dx \quad (1.7)$$

where  $E_{in}$  is the incident energy of the ion,  $x_0$  is the entering point of the ion into the target and  $x_{range}$  is its stopping point. Note that additionally to the direct electronic loss of the ion  $E_{el}^{ion}$  there is a second electronic contribution  $E_{el}^{rec}$  from the target recoils, created by elastic collisions between the incident ion and the target nuclei, which by themselves start to propagate through the target if the transferred energy exceeds the lattice binding energy and which are then able to transfer their energy to the target electrons.

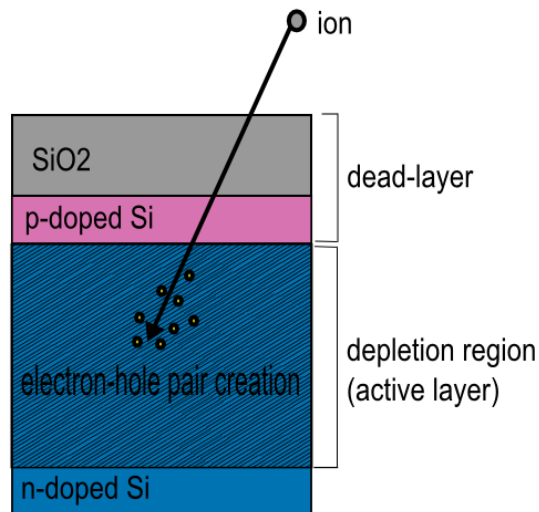


FIGURE 1.9: Solid State Detector Scheme.

### 1.1.2 SRIM Simulation Package

SRIM (Stopping and Range of Ions in Matter) is a scientific software package which calculates the stopping and range of ions from keV energies up to several GeV in matter using a quantum mechanical treatment of ion-atom collisions. The main program in the SRIM package is TRIM which is a Monte-Carlo code simulating the TRansport of Ions in Matter. It can be applied to simple geometries and a wide range of materials included in the program library. However, the target material is always assumed to be amorphous so that no crystalline effects such as channeling can be simulated. For further information the reader is referred to the comprehensive SRIM User Manual [39].

## Chapter 2

# The CELIAS Experiment aboard SOHO

### 2.1 The Solar and Heliospheric Observatory

The Solar and Heliospheric Observatory (SOHO) was built to resolve several long-standing problems in solar physics such as the coronal heating problem and the acceleration of the solar wind. Both topics are of special interest for the in-situ community which provided three particle instruments, among them the CELIAS instrument (see figure (2.1)). Furthermore the spacecraft is suited with helioseismological and remote sensing instruments which add up to a complete scientific payload of 11 instruments [35].

SOHO was launched in December 1995 and is still in operation. It is situated on an orbit close to L1 and is a 3-axis stabilized spacecraft, which means that all particle instruments point in their fixed direction all the time which is in contrast to e.g. the Advanced Composition Explorer (ACE) or the Helios spacecraft which are/were all spinning around their axis.

### 2.2 The CELIAS Experiment

The *Charge, Element, and Isotope Analysis System* (CELIAS) [33] aboard SOHO was built by the University of Bern in cooperation with the Max-Planck-Institute for Solar System Research in Katlenburg-Lindau (former Institute for Aeronomy) and consists of

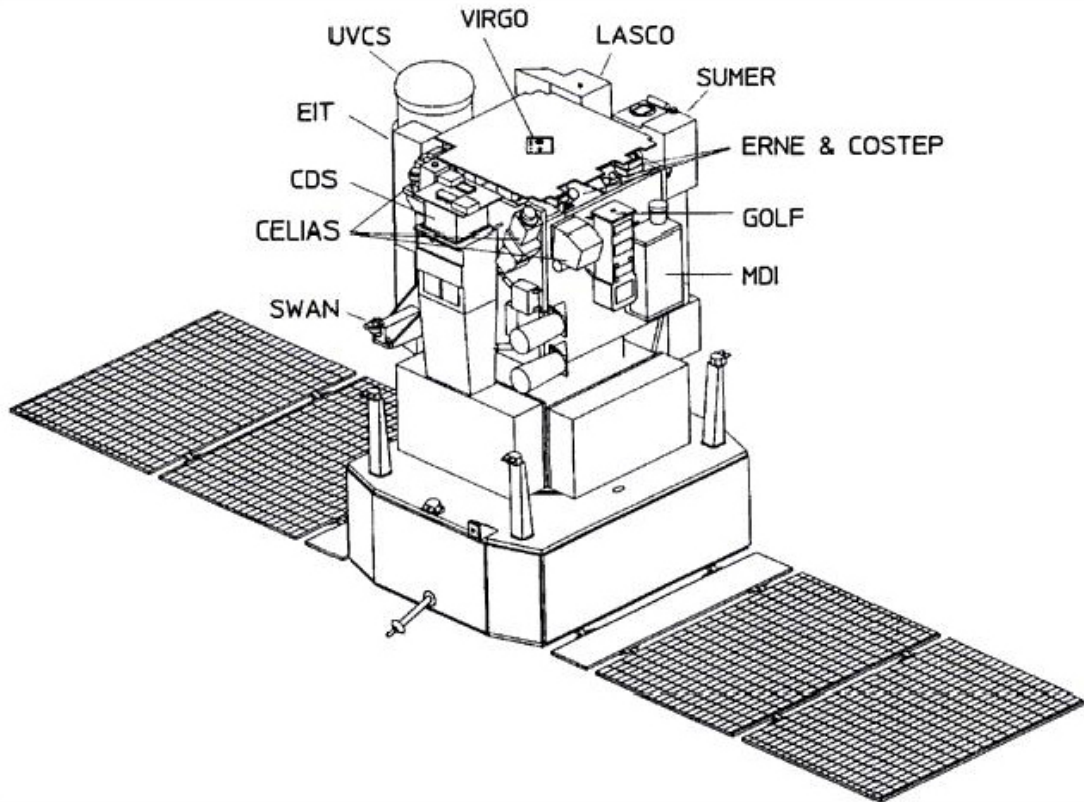


FIGURE 2.1: Overview of the SOHO spacecraft with its scientific payload. The picture is taken from [35].

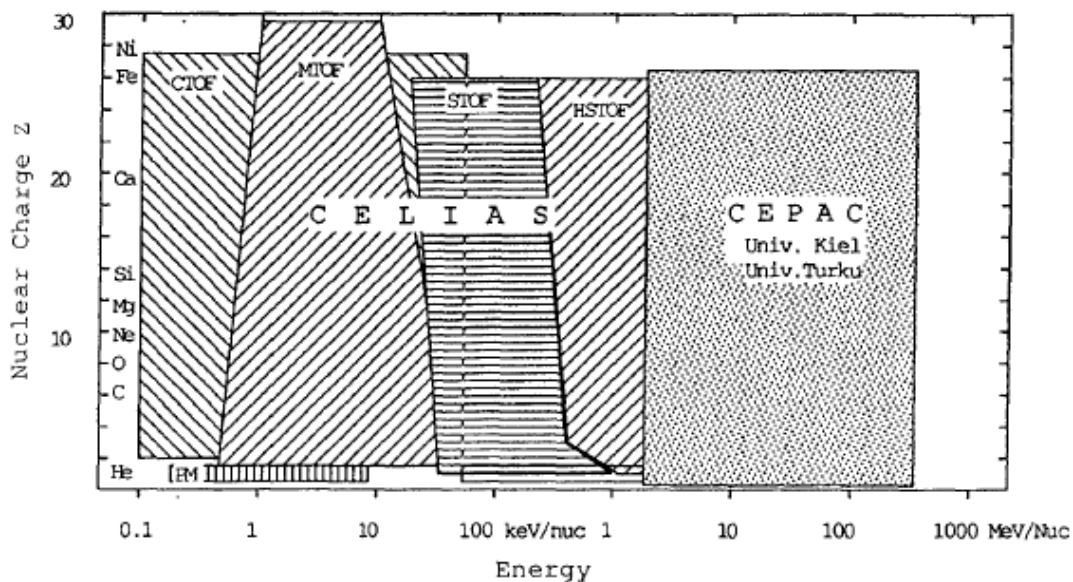


FIGURE 2.2: Energy range coverage of the CELIAS sensors and the CEPAC package, taken from [33]. CELIAS measures particles at solar wind speeds, as well as pick-up ions and suprathermal particles. CEPAC is a cooperation of the University of Turku and the University of Kiel and measures the high energy particles.

four different sensors which all investigate ions within or slightly above the solar wind energy range. These sensors are the Charge Time-OF-Flight sensor (CTOF), the Mass Time-OF-Flight sensor (MTOF), the Suprathermal Time-OF-Flight (STOF) sensor and the Proton Monitor (PM). Here we concentrate on the CTOF sensor and the Proton Monitor:

**CTOF** CTOF is a linear time-of-flight mass spectrometer with remarkable time-of-flight resolution which allows for a very good separation of heavy ions in mass-per-charge. Furthermore it has a large geometry factor by blending out the solar wind protons. Unfortunately the instrument suffered a serious failure already on DOY 230 1996, so that it delivered only data during a few months around solar minimum in 1996. For a more detailed description of the CTOF sensor see the following section.

**PM** The Proton Monitor is integrated in the MTOF housing and measures the proton mean speed, temperature and particle density with a time resolution of about one minute. Since the proton parameters of the solar wind at L1 are well-known today, the PM data is not of great interest itself, but serves as solar wind plasma parameter reference for the other three sensors. In this work the analysis of the heavy ion differential streaming is done by comparison of the CTOF data with the PM data. For our analysis we used five-minute averaged PM data which we synchronized with the CTOF data.

# Chapter 3

## The CELIAS/CTOF Sensor

### 3.1 Principle of Operation

The CTOF sensor is a linear time-of-flight mass-spectrometer based on the carbon-foil technique which was already successfully applied in e.g. the Solar Wind Ion Composition Sensor (SWICS) on the Ulysses spacecraft. A cross-section of the CTOF instrument is shown in figure 3.1. CTOF measures heavy ions in the energy-per-charge range between 0.3 and 34.7 keV/nuc and is able to determine the ion's mass  $m$ , its charge  $q$  and its velocity component parallel to the spacecraft-Sun connection line which we denote as  $v$ . To unambiguously determine the three quantities, three measurements are performed successively on the incident ions. These are illustrated in figure (3.2): An incoming ion is first analyzed for its energy-per-charge ( $E/q$ ) value in the electrostatic analyzer (ESA) which we also refer to as the entrance system. Second it is accelerated by a post-acceleration high voltage  $U_{acc}$  on the order of 23 kV before it penetrates a thin carbon foil releasing secondary electrons from the foil which are then collected to trigger a start pulse for the time-of-flight (ToF) measurement. When the ion reaches the solid state detector after its passage through the ToF section it creates secondary electrons at the SSD surface which trigger the stop pulse for the ToF measurement. The time interval between the two pulses is denoted as  $\tau$ . Finally the residual kinetic energy of the ion  $E_{SSD}$  is measured in the solid state detector.

In order to measure the several ion species at different velocities the electrostatic analyzer can be stepped through different energy-per-charge values by changing the applied voltage after:

$$\frac{1}{2} \cdot \frac{m}{q} \cdot v^2 = \left( \frac{E}{q} \right)_j = U_j = U_0 r^{s_{max}-j} \quad (3.1)$$

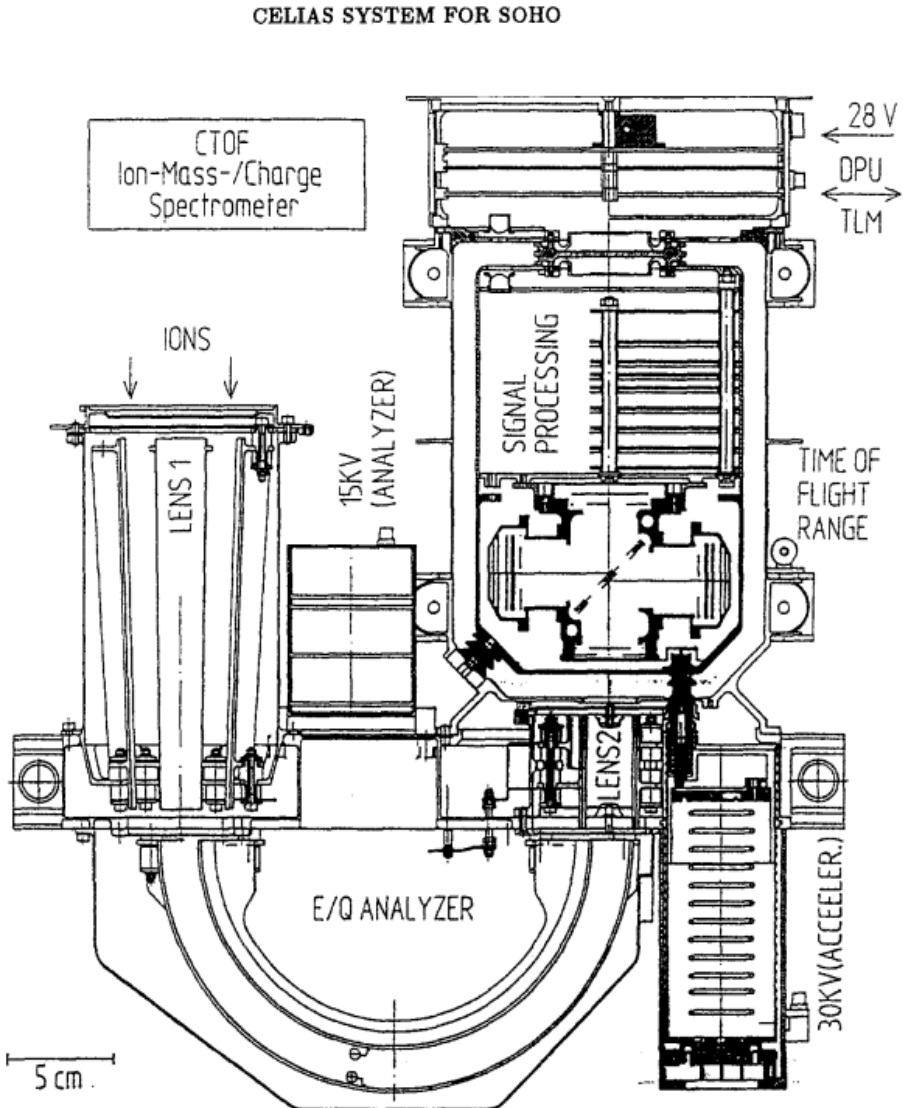


FIGURE 3.1: CTOF cross-section, from [33].

where  $j$  is the ESA ( $E/q$ -) step number obtaining values from 0 to  $s_{max} = 116$ ,  $U_0 = 0.331095$  kV is the lowest applied voltage at step 116 and  $r = 1.040926$  is a dimensionless scaling parameter. All values are taken from [34], [35]. At a fixed energy-per-charge step the residual energy measurement can be plotted against the ToF measurement of each particle leading to 2-dimensional histograms as shown in figure 3.3 which we call *ET-matrices*. Since each ion species is defined by its mass and charge, its velocity (and kinetic energy) is determined by the ESA step and therefore, all ions of the same species ideally end up in the same bin of the ET matrix. Or if we interpret it the other way around, from the ions' positions in the ET-matrix we could unambiguously determine

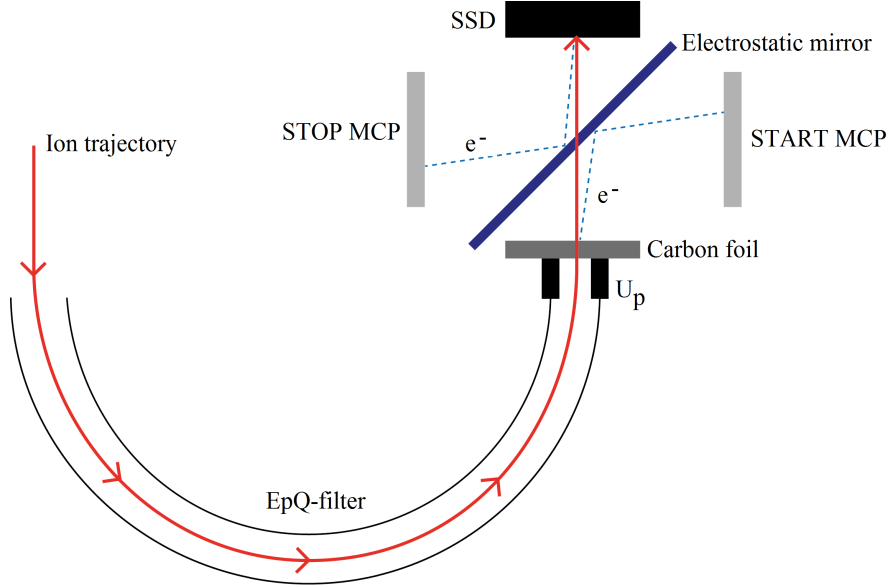


FIGURE 3.2: CTOF measurement scheme, from [40].

their mass end charge by

$$\frac{m}{q} = 2 \cdot \frac{\tau^2}{L_\tau^2} \left[ \left( \frac{E}{q} \right) + U_{acc} \right] \quad (3.2)$$

$$m = 2 \cdot \frac{\tau^2}{L_\tau^2} \cdot E_{SSD} \quad (3.3)$$

where with  $L_\tau = 70.5$  mm as the known length of the time-of-flight section all quantities are given. In such a case the in-flight calibration of the sensor would be straightforward by just calculating all ions' position  $(\tau, E_{SSD})$  in the ET-matrix by putting their given mass and charge into Eq. (3.2) and (3.3).

Unfortunately this is not the case for the real instrument in which the particles (1) lose a non-negligible part of their energy in the carbon foil and (2) do not convert their complete kinetic energy into the measured SSD energy signal. Both processes depend on the ion's atomic number and velocity prior to the foil and the SSD, respectively, and can be understood with the considerations concerning the interaction of charged particles in matter, made in chapter 1. Therefore, Eq. (3.2) and (3.3) transform to:

$$\frac{m}{q} = 2 \frac{\tau^2}{L_\tau^2} \left[ \left( \frac{E}{q} \right) + U_{acc} - \frac{\Delta E(v, Z)}{q} \right] \quad (3.4)$$

$$m = 2 \cdot \frac{\tau^2}{L_\tau^2} \cdot \frac{E_{SSD}}{\eta(v, Z)} \quad (3.5)$$

where  $\Delta E(v, Z)$  is the ion's energy loss in the carbon foil and  $\eta(v, Z)$  its pulse height fraction in the SSD. The appearance of these terms which are dependent on the ion velocity and which cannot be calculated analytically, makes an accurate in-flight calibration of the CTOF sensor relatively complicated. The route to go is the simulation of  $\Delta E$  and  $\eta$  with TRIM.

As can be seen from figure 3.3, where we marked some of the most abundant solar

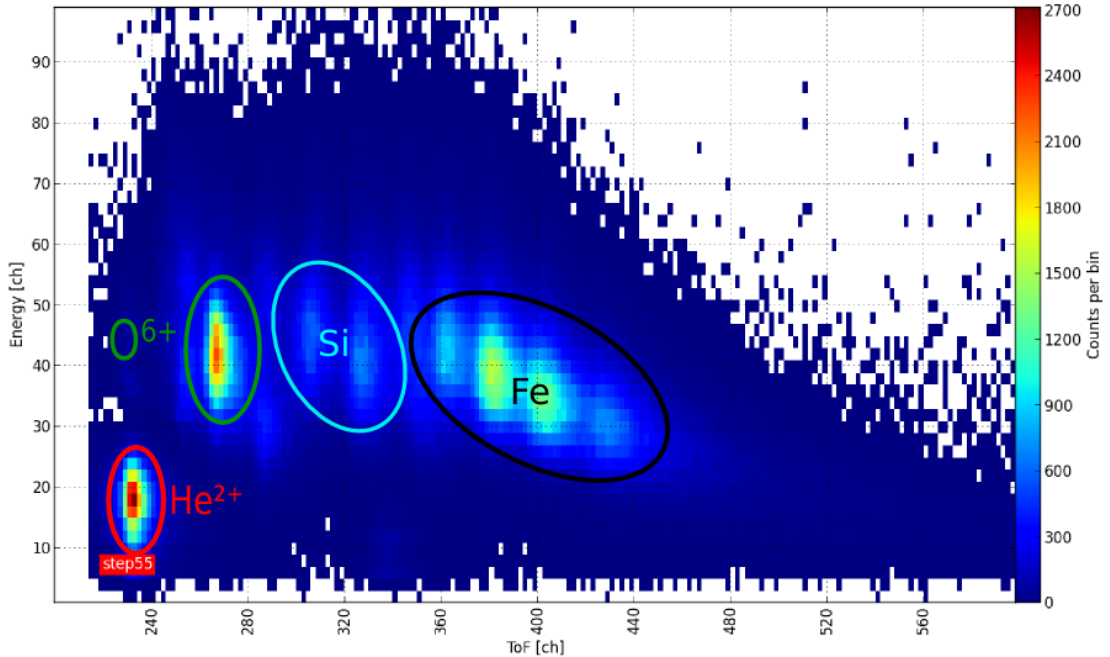


FIGURE 3.3: CTOF ET matrix in E/q-step 55 with some of the most abundant solar wind ions.

wind ions, the different ion peaks have finite widths both in ToF and energy. These arise due to straggling in both the carbon foil and the solid state detector. Also other factors could possibly cause a spread both in the time-of-flight and energy signal such as the width of the velocity window, also called the velocity acceptance, of the electrostatic analyzer. This is given in [35] by

$$\Delta v/v = 1.2\% \quad (3.6)$$

where  $\Delta v$  scales linearly with velocity which means that the absolute acceptance is larger for faster particles. Further factors influencing the observed signal widths are the signal shapes of the read-out electronics, which in a good instrument, however, should have been chosen small enough not to be the limiting resolution factor. Before starting

with the calibration we have a short look on the raw CTOF pulse height analysis (PHA) data to motivate the relatively sophisticated calibration procedure.

### 3.2 CTOF Data

In figure 3.4 on the left it is shown the ET-matrix for ESA step 50 for the 70-day measurement period DOY 150 1996 - DOY 220 1996 whereas on the right it is displayed the ET-matrix for the same E/q-step but for the much shorter 5-minute time interval of min 149 - 154 of DOY 213 1996. The time interval DOY 150 - 220 1996 is selected for this work, because it is one of two extended time intervals of several months in which CTOF was operated without adjustment changes in the applied post-acceleration voltage. Although the final instrument failure appeared on DOY 230 1996 the count rate data showed an increased noise level for the last ten days of operation already from DOY 221 1996 on, so that we excluded this time period. Furthermore on DOY 180 1996 a Coronal Mass Ejection (CME) passed SOHO for several hours, leading to completely different plasma conditions within this short time period, which is therefore excluded from this study, as well. We refer to the 70-days accumulated data as *long-time data*, while all data accumulated over several minutes only will be referred to as *short-time data*. In figure 3.4 we can see that while in the long-time data one can already recognize

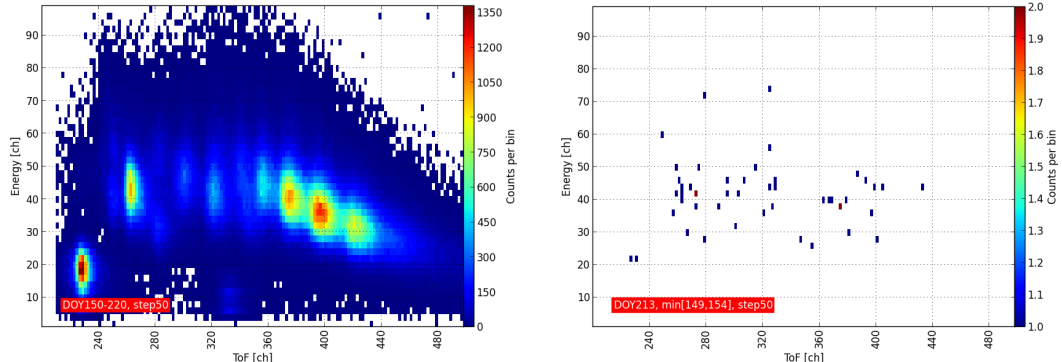


FIGURE 3.4: CTOF ET-Matrices for E/q-step 50 for two measurement periods of extremely different duration. Left: long-time data of DOY 150-220 1996, right: short-time data of minutes 149 - 154 of DOY 213 1996.

the distributions of the most prominent ions, especially  $\text{He}^{2+}$  and  $\text{O}^{6+}$  around TOF-channel 230 and 270, respectively, this is clearly not the case for the short-time data. Thus analyzing CTOF data on minute time resolution needs an accurate in-flight calibration both of the most probable ion positions, as well as of their peak shape in the ET-matrices, which is performed in the next chapter. We finally mention that due to an unknown error in the raw data, showing every second channel enhanced in count rate

compared to its neighbor channels, we had to bin each two channels together, so that the accuracy for the assignment of a single count to a specific ion by a simple box rate counting method (see chapter 5) is naturally limited by 2 channels.

## Chapter 4

# In-Flight-Calibration of the CTOF-Sensor

### 4.1 Time-of-Flight Calibration for Solar Wind Ions

In his master thesis A. Taut [40] already performed an in-flight calibration of the CTOF time-of-flight section which was conceived to investigate pick-up ions with CTOF. By performing fits to several pick-up ion peaks appearing in the CTOF data similar to the ones to be shown in this section he was able to accomplish a calibration for the time-of-flight measurement proofed to be valid for pick-up ions and even a few solar wind ions such as  $\text{Fe}^{10+}$ ,  $\text{Fe}^{11+}$ ,  $\text{O}^{6+}$  and  $\text{He}^{2+}$ . Since the pick-up ion measurement is done simultaneously with the solar wind measurement and the calibration was supposed to cover the whole instrument ToF range from channel 200 to 600 this calibration should be valid for our measurements, too, and we can adopt the obtained calibration constants. These constants were determined to  $a_{\text{tof}} = 0.200723 \text{ ns/ch}$ ,  $b_{\text{tof}} = -1.46909 \text{ ns}$  and allow us to linearly convert the observed ToF channel number to seconds via:

$$\tau[\text{ns}] = a_{\text{ToF}} \cdot \tau[\text{ch}] + b_{\text{ToF}} \quad (4.1)$$

Furthermore, in [40] it is stated that consistent values of  $a_{\text{ToF}}$  and  $b_{\text{ToF}}$  for all fitted ions could only be found by a slight variation of the nominal values for the CTOF carbon foil thickness and post-acceleration. These values were determined simultaneously to  $d_{\text{foil}} = 240 \text{ \AA}$  and  $U_{\text{acc}} = 23.85 \text{ keV}$  for the time period DOY 150-230 1996 which fully contains the measurement period of this work.

But even if the largest part of the work was done by Taut by deriving the given constants which fully determine the ToF measurement, we still have to calculate the energy loss  $\Delta E(Z, v)$  for all relevant solar wind elements and also at the relevant solar wind

speeds which are in general different from the pick-up ion speeds. Furthermore we will double-check the obtained ToF values of the solar wind ions selected by Taut and take into account additional calibration ions such as e.g. Si<sup>7+</sup> and Si<sup>8+</sup>. Finally we still have to find a model for the ToF peak widths which will be the last part of the ToF calibration.

#### 4.1.1 Selection of the Reference Ions

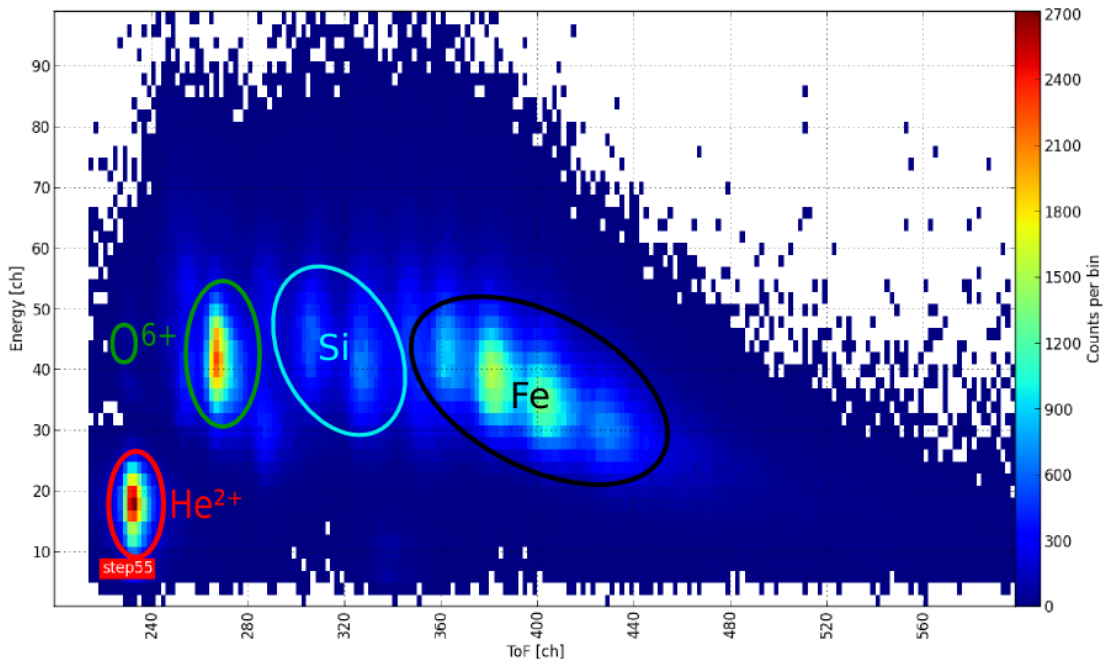


FIGURE 4.1: CTOF ET matrix in E/q-step 55 with the described reference ions.

In the first step of the calibration we determine the position of a few well-distinguishable solar wind heavy ions within the ET-matrix for a number of E/q-steps. These ions will be referred to as *reference ions* and act as calibration points within the ET-matrix. All of these ions can be found by eye in a sufficient number of long-time data matrices similar to the one in figure 4.1 since they show significantly higher count rates than their adjacent ions which have similar mass and m/q ratio. The identification of these reference ions relies on established facts about the solar wind elemental [10], [41] and charge state composition [15], [42] which were briefly discussed in chapter 1. We selected the following reference ions:

- $\text{He}^{2+}$  is by far the most abundant solar wind heavy ion since helium is, after hydrogen, the second most abundant element in the solar corona and its second ionization potential of 54 eV lies far below the average free electron energy within the corona of 129 eV corresponding to an electron temperature of  $\sim 1.5 \text{ MK}$  [30]. Thus practically every solar wind helium atom is double ionized. In figure 4.1 it can be seen that the  $\text{He}^{2+}$  distribution is well-separated in time-of-flight from the  $\text{He}^{1+}$  pick-up ions due to the relatively large difference in  $\Delta(m/q) = 2.0 \text{ amu/e}$  and from the heavier elements it is well separated in residual energy due to its small mass of only 4 amu.
- Oxygen is among the most abundant solar wind elements and both in the fast and slow solar wind the by far most populated oxygen charge state is  $\text{O}^{6+}$ , which is due to the achieved noble gas configuration. This leads to a dominant  $\text{O}^{6+}$  peak in the ET-matrix. Having a mass-per-charge ratio of  $m/q = 2.7 \text{ amu/e}$  and a mass of  $m = 16 \text{ amu}$  it is well-separated from the  $\text{He}^{2+}$  peak both in time-of-flight and energy.
- The most abundant iron charge states are supposed to be centered around  $\text{Fe}^{9+}$  and  $\text{Fe}^{10+}$ . Therefore, the iron sequence is mostly situated at mass-per-charge ratios greater than  $m/q = 5 \text{ amu/e}$ , which guarantees a good separation in time-of-flight from the  $\text{O}^{6+}$  and  $\text{He}^{2+}$  peak.
- Finally the most abundant silicon ions lie at charge states centered around  $\text{Si}^{8+}$ , which leads to  $m/q$ -ratios between 3 and 4 amu/e. This still ensures a sufficient separation in time-of-flight from the  $\text{O}^{6+}$  and the iron distributions.

As can be seen from figure 4.1 with these few reference ions we are able to span a wide range within the ET-matrix both in time-of-flight and residual energy. Later this will allow us to interpolate the exact positions of less abundant ions and thus obtain a complete calibration including all relevant solar wind ions.

#### 4.1.2 Fit of the Reference Ions

In a first approach the fits are performed as simple 2D-Gaussians in time-of-flight and residual energy. The fitfunction for a single ion distribution such as  $\text{He}^{2+}$  is thus given by

$$f_{fit} = f_{g2d}(T, E) = h \cdot \exp\left(-\frac{1}{2} \frac{(T - T_0)^2}{\sigma_T^2}\right) \cdot \exp\left(-\frac{1}{2} \frac{(E - E_0)^2}{\sigma_E^2}\right) \quad (4.2)$$

where the free fit-parameters are the peak-height  $h$ , the mean time-of-flight  $T_0$ , the mean residual Energy  $E_0$  as well as the the ToF- and energy-sigmas  $\sigma_T$  and  $\sigma_E$ . Three

examples for the performed fits of  $\text{He}^{2+}$  at different E/q-steps are shown in figure 4.2.

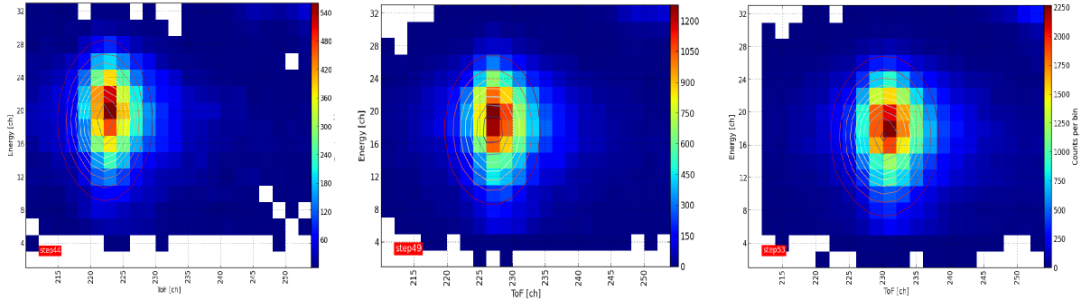


FIGURE 4.2: Applied single Gaussian fits of  $\text{He}^{2+}$  at E/q-step 44, 49 and 53.

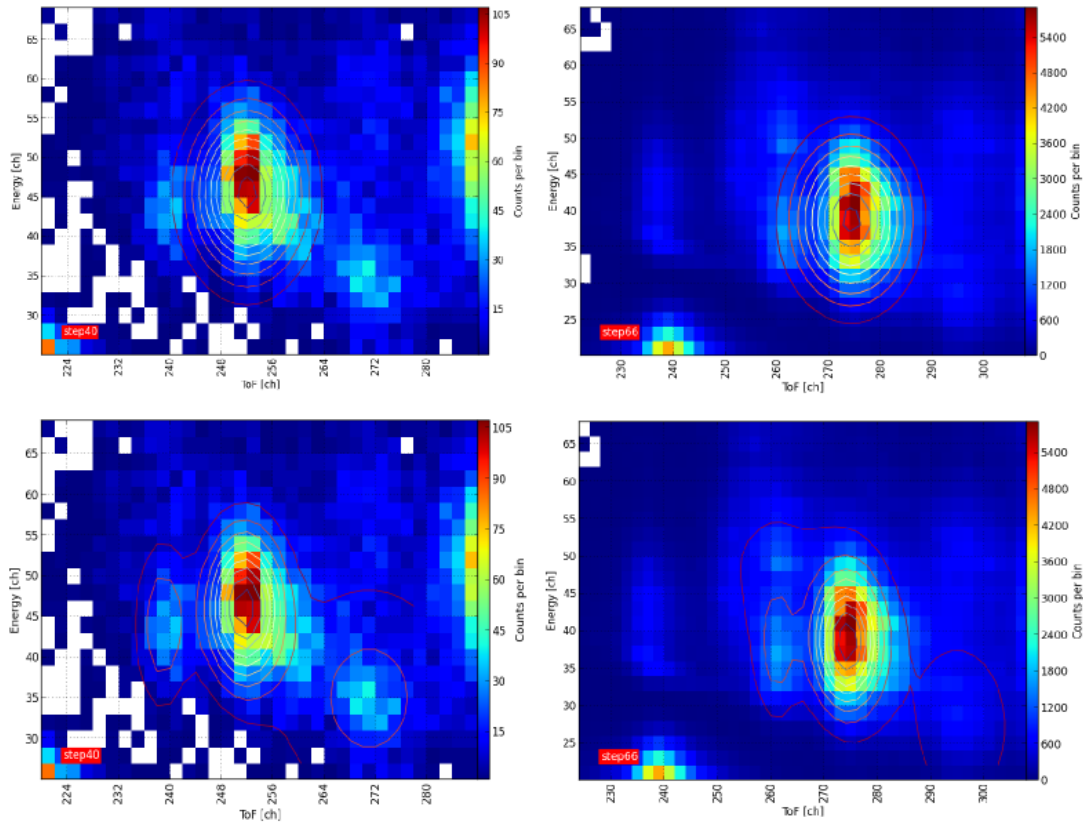


FIGURE 4.3: Applied single-Gaussian and multiple-Gaussian fits of the  $\text{O}^{6+}$  peak and its adjacent peaks:  $\text{C}^{4+}$  (at its high-ToF, low-energy flank)  $\text{C}^{5+}$  (at its low-ToF, low-energy flank) and  $\text{Ne}^{8+}$  (at its low-ToF, high-energy flank) at E/q-steps 40 and 66.

Already for oxygen this simple single-peak model has to be reviewed since, as can be seen in figure 4.3, at several E/q-steps there appear adjacent peaks on the low- and high-ToF flank of the  $\text{O}^{6+}$  peak which can be identified as  $\text{C}^{5+}$ ,  $\text{C}^{4+}$  and  $\text{Ne}^{8+}$ , respectively. In order to estimate the influence of these adjacent distributions on the estimated

parameters of the  $O^{6+}$  peak, we performed fits with both a single-peak model and a multiple-peak model, being just the superposition of several Gaussians:

$$f_{fit} = \sum_i^N f_{g2d,i} \quad (4.3)$$

with  $N$  as the number of fitted peaks which is in the case of  $O^{6+}$  either  $N = 3$ , when we included only the carbon peaks in the fit (as done for E/q-step 34 to 55) or  $N = 4$  when we additionally included the  $Ne^{8+}$  peak (step 51 to 70) as can be seen in figure 4.3 in the lower left and right panel, respectively.

The comparison of the estimated fit parameters obtained from the single-peak fits (upper panels) and the multiple-peak fits (lower panels) in figure 4.4 shows that the inclusion of the carbon and neon distributions which are roughly a factor of 3-5 lower than the  $O^{6+}$  peak and which are both peaking in its 2-sigma environment did not influence the estimated ToF and energy position of the  $O^{6+}$  peak significantly since the difference between positions estimated with the different models is far below 2 ch. However, it significantly influenced the estimated distribution widths changing this value in time-of-flight of about 2 to 6 channels and in energy of about 2 channels. For the energy width it even makes a slight difference, whether we include the  $Ne^{8+}$  peak as well, which is reasonable since it additionally confines the  $O^{6+}$  peak at the high energy flank.

As conclusion we find that the positions obtained from the 2D-Gaussian fit model are rather robust while the obtained widths are influenced by adjacent peaks when included in the fit. Therefore, it is a meaningful approach to calibrate the positions with a simple 2D-Gaussian model while for the estimation of the widths it is worth to improve the calibration by taking into account the surrounding peaks as soon as their position in the ET-matrix can be determined.

For the even heavier silicon and iron ions the situation is even more complex than for oxygen as can be seen in figure 4.5. With the previous considerations it is thus reasonable to include all prominent silicon and iron charge states at a given E/q-step in one fit. For Silicon the performed fit always includes the  $Si^{7+}$  and  $Si^{8+}$  peaks and depending on the concrete step which for a given ion species is equivalent to a selected velocity window also appearing adjacent distributions such as  $C^{4+}$ ,  $Si^{9+}$  and  $Fe^{12+}$ . A similar approach was chosen to fit the iron peaks: We always included  $Fe^{8+}, Fe^{9+}, Fe^{10+}$  in the fit and added adjacent peaks  $Fe^{7+}$ ,  $Fe^{11+}$  and even  $Fe^{12+}$  when possible. Examples of these fits are shown in figure 4.5.

As outcome of all fits we obtain the position of the reference ions in the ET-matrix, as well as their distribution widths both in time and energy. Note that only the inner ion

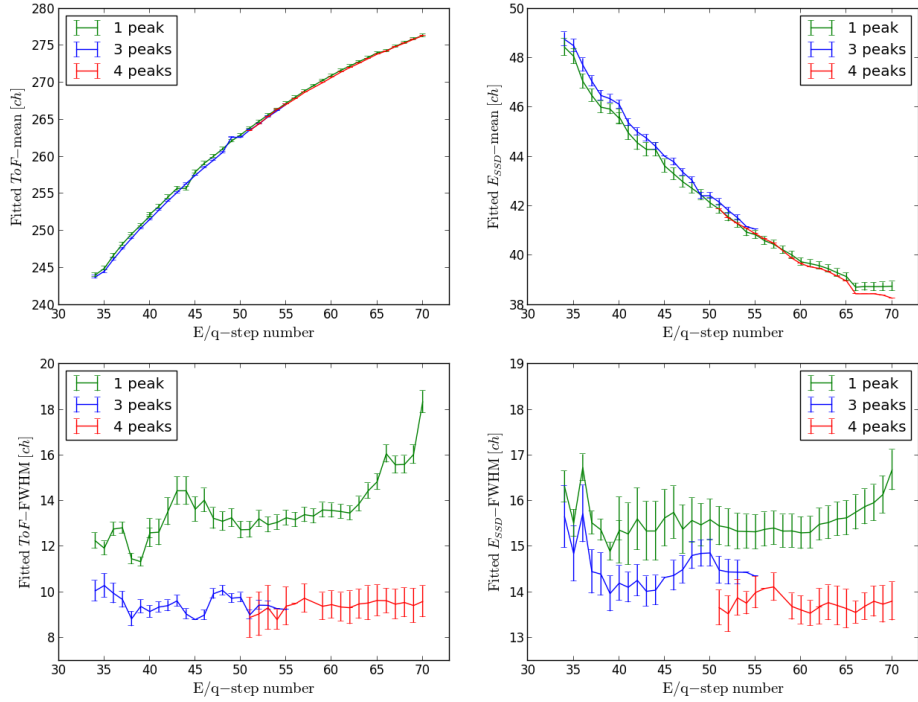


FIGURE 4.4: Fitted peak positions (upper panels) and widths (lower panels) for the  $O^{6+}$  peak. The peak was fitted with a single Gaussian (green) and the sum of 3 (blue) and 4 (red) Gaussians including the adjacent  $C^{4+}$ ,  $C^{5+}$  and also  $Ne^{8+}$  peaks in the fit.

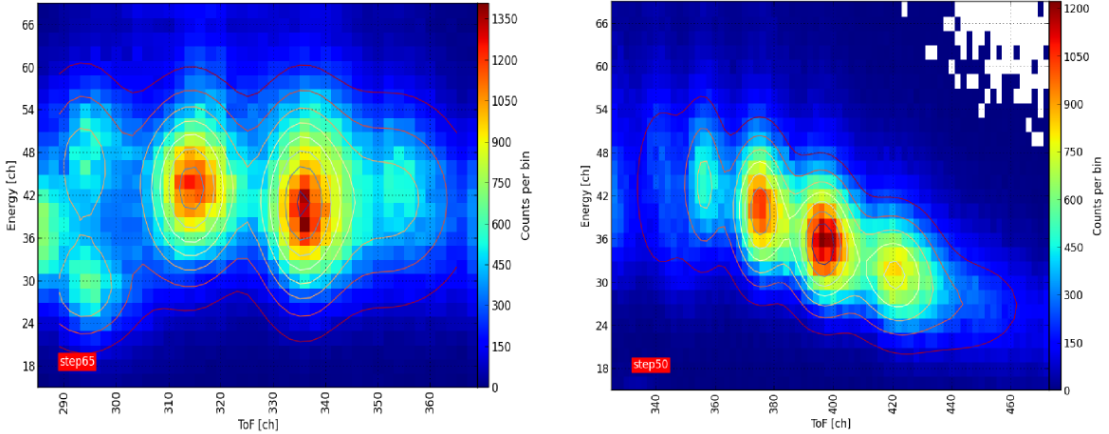


FIGURE 4.5: Examples of the accomplished fits for silicon (left) and iron (right). At the shown  $E/q$ -step 65 we included  $Si^{9+}$ ,  $C^{4+}$ ,  $Si^{8+}$ ,  $Si^{7+}$  and  $Fe^{12+}$  (from left to right) in the applied silicon fit. In the iron fit at step 50 we included  $Fe^{12+}$ ,  $Fe^{11+}$ ,  $Fe^{10+}$ ,  $Fe^{9+}$ ,  $Fe^{8+}$  and  $Fe^{7+}$  from left to right. In the silicon fit especially the  $C^{4+}$  and  $Si^{9+}$  are likely to be influenced by the flank of the adjacent  $O^{6+}$  distribution lying on the fit boundary. As can be seen in the iron fit the  $Fe^{12+}$  peak seems to be shifted to lower energies by the influence of adjacent minor ions not included in the fit such as  $Si^{6+}$  or  $S^{7+}$ .

peaks  $Si^{7+}$ ,  $Si^{8+}$  and  $Fe^{8+}$ ,  $Fe^{9+}$ ,  $Fe^{10+}$  are taken into account for the in-flight calibration while the other ions, lying close to the boundary of the fit region or likely to be

influenced by even minor peaks not included in the fit, will not be considered below. The position of each ion fitted at a number of E/q-steps is shown in the top panel of figure 4.6 together with the corresponding error bars in time-of-flight and energy. In the bottom panel we additionally plotted the fitted widths.

The different elements form their own hyperbolas in the ET matrix as it is implicitly assumed in (3.5) of chapter 3 while the different ionic charge states of each element are lying on the same curve. The very small position uncertainties both in time-of-flight and energy are derived automatically from counting statistics by the fit routine, but are also cross-checked with a Monte-Carlo bootstrap error estimation. Comparing these uncertainties with the ion peak widths it is clear that they will not play a big role for later error estimations of the obtained count rates. Furthermore the absence of significant discontinuities between the estimated positions of different charge states along the iron and silicon hyperbolas makes it rather improbable that there are significant systematic errors in the estimated fit positions caused by non-resolvable underlying ions. In fact these would most likely affect a shift of only one charge state of an element but in most cases not a shift of two or even three charge states in the same way. In addition this shows that all instrumental effects resulting from the original particle charge, such as e.g. focusing effects in the entrance system can be neglected for this calibration.

#### 4.1.3 Calculation of the ToF Peak Positions with TRIM

With the values given at the beginning of this chapter for  $a_{ToF}$ ,  $b_{ToF}$ ,  $U_{acc}$  and  $d_{foil}$ , it is now possible to calculate the most probable ToF positions for the solar wind reference ions using TRIM. The comparison between these calculations and the fitted position thus provides a consistency check and uncertainty estimation of the earlier calibration [40], in particular in the solar wind velocity range. If the model holds we can calculate all ToF positions of even less abundant ions in the ET-matrix.

The TRIM simulation of the time-of-flight section, as explained in chapter 3, is basically the simulation of the ions' carbon foil passage. We therefore define the simulation target as the CTOF carbon foil consisting of pure carbon as it is specified in the standard TRIM target material tables. The target thickness is set to 240 Å as explained above. From equation (3.1) and the determined post-acceleration of  $U_{acc} = 23.85$  kV we can obtain the particles' energy  $E_{acc}$  prior to the time-of-flight section for each ionic species at each E/q-step at which we successfully applied a fit. The obtained energy ranges for the reference ions are shown in table 4.1 for all reference ions and represent the initial energy range for the TRIM simulation: Since TRIM according to theory does not distinguish between different charge states of an element, here the minimum energy

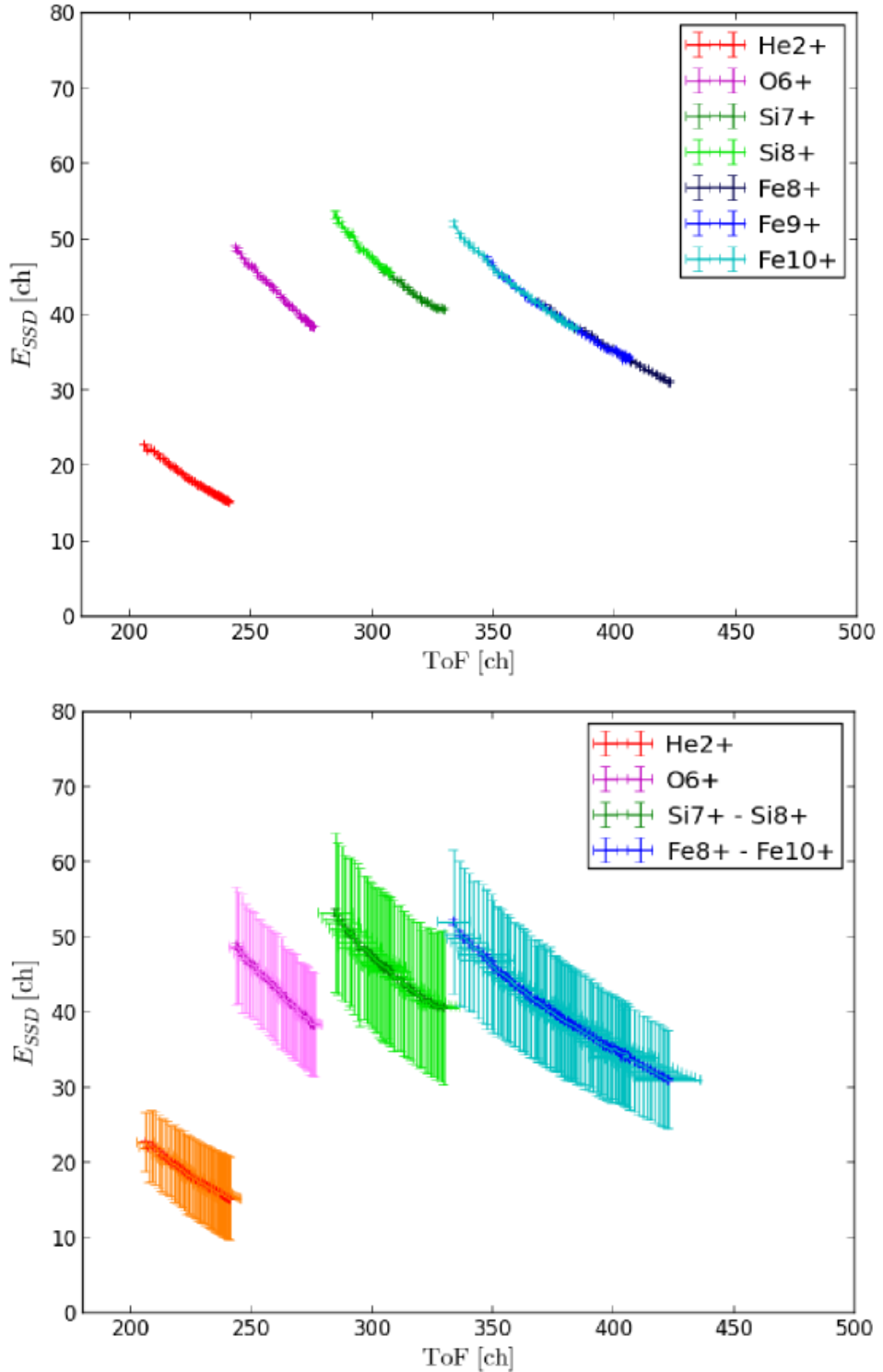


FIGURE 4.6: Fitted ET-matrix positions with uncertainties (upper panel) and fitted widths (lower panel) for all reference ions and all selected  $E/q$ -steps. In the lower panel we plotted all charge states of the same element in the same color, since both in theory and as shown in the upper panel the ionic charge has no effect on the ToF and energy measurement except for the amount of energy that the ions receive from the post-acceleration voltage.

Ion	min. step	max. step	min. $E_{acc}$ [keV]	max. $E_{acc}$ [keV]
He2+	30	73	<b>52</b>	<b>69</b>
O6+	40	70	<b>156</b>	<b>185</b>
Si7+	38	58	<b>191</b>	220
Si8+	38	58	218	<b>251</b>
Fe8+	27	57	<b>219</b>	285
Fe9+	25	60	242	329
Fe10+	27	60	270	<b>356</b>

TABLE 4.1: Reference ion energies  $E_{acc,j} = q \cdot [(E/q)_j + U_{acc}]$  after the post acceleration. The energy ranges are obtained for the steps  $j$ , in which we applied fits to the reference ions. They represent the initial energies for the TRIM simulation of the ToF measurement.

of the lowest charge state and the maximum energy of the highest charge state (bold numbers) define the initial energy range for the simulation for each element.

By simulating the passage of an ion sample at a given initial energy we obtain the energy loss spectrum which is produced by the statistic process of energy straggling in the carbon foil. Four examples of such energy spectra at different initial energies are shown in figure 4.7. Both the oxygen and iron spectra show the general trend that the most probable energy loss in the foil only increases weakly with increasing initial energy, so that the relative energy loss  $\Delta E/E_{in}$  decreases with increasing initial energy. One also recognizes that while the oxygen spectra only show a slight asymmetry but are still in good agreement with a Gaussian shape the iron spectra show pronounced tails towards higher energy losses. These tails result from a fraction of particles that undergo strong straggling in the foil, due to the collision with its carbon nuclei and this effect is more pronounced for ions having low initial velocities and high atomic numbers.

In order to calculate the energy loss for all fitted steps, we run the TRIM simulation within the element ranges given in table 4.1 with 5 keV increment. The resulting relative energy loss, calculated as the ratio between the most probable absolute energy loss and the initial energy, is plotted in figure 4.8 against the initial energy (left panel) and initial velocity (right panel) for each element together with a continuous fit to the simulation data. The obtained curves show that for all elements the relative energy loss decreases with increasing initial energy. When plotting the relative energy loss against the initial velocity the distinct dependencies of velocity and atomic number become visible: At a given initial velocity the relative energy loss shows the trend to decrease with increasing atomic number.

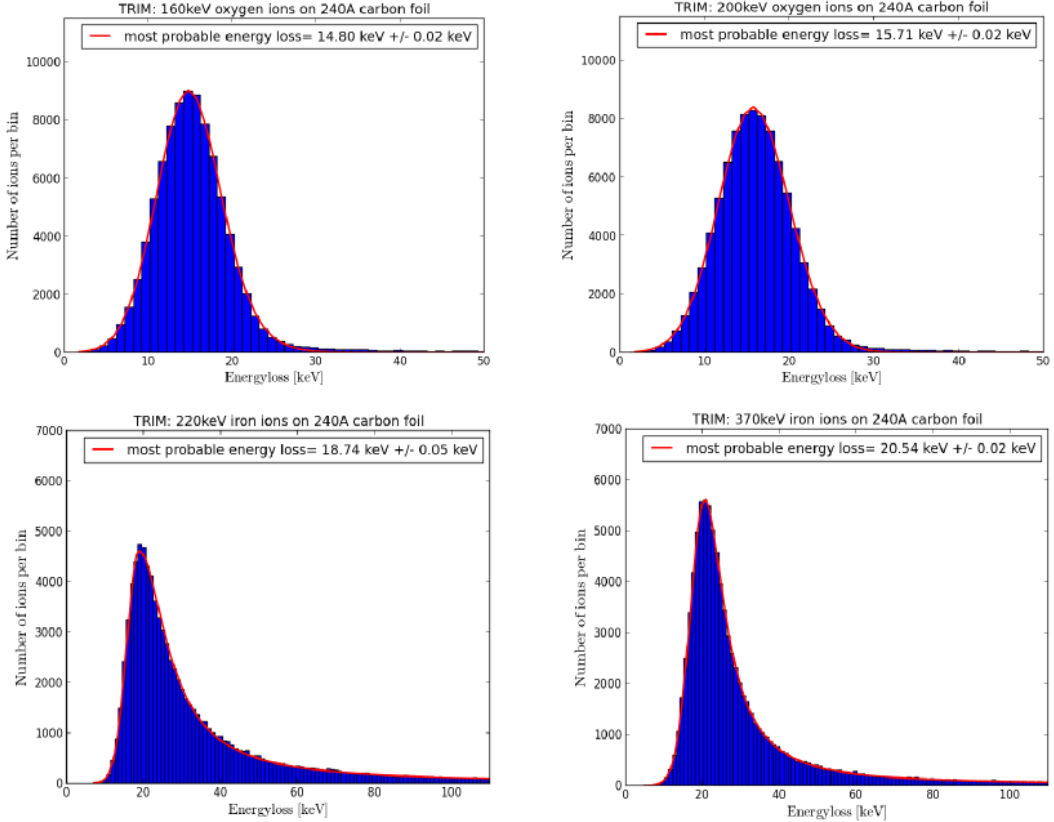


FIGURE 4.7: Energy loss spectra for oxygen (upper panels) at initial particle energies of 160 keV and 200 keV and iron at 220 keV and 370 keV. These energies correspond to initial velocities of 1350 km/s, 1550 km/s and 850 km/s, 1150 km/s, respectively. All spectra are fitted with kappa-functions, allowing to model the pronounced tails in the iron spectra. The kappa-function is explained in section 4.3 as part of a more elaborated peak-shape model.

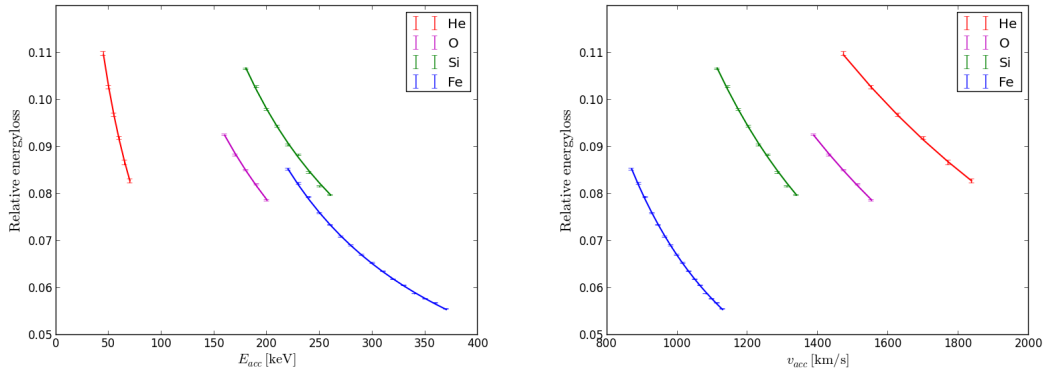


FIGURE 4.8: Relative energy losses of the reference elements in the carbon foil as calculated with TRIM. In the left panel the relative energy loss is plotted against the incident energy while in the right panel it is plotted against the incident velocity of the ions after the post-acceleration.

The accomplished fit to the simulation data follows the dependency:

$$\alpha_{\Delta E}(E_{acc}) = \frac{A_i}{B_i \cdot E_{acc}} + C_i \quad (4.4)$$

with  $A_i$ ,  $B_i$  and  $C_i$  as individual constants for each element.

From the calculated relative energy loss  $\alpha$ , we can now determine the time-of-flight position of each ion at a given step in the ET-matrix:

$$\tau[ch] = a_\tau^{-1} \cdot \left( \sqrt{\frac{m \cdot L^2}{2 \cdot \alpha \cdot E_{acc}}} - b_\tau \right) \quad (4.5)$$

The calculated time-of-flight channels obtained from the simulation are plotted in figure 4.9 for all reference ions together with the fitted positions at each  $E/q$ -step. When

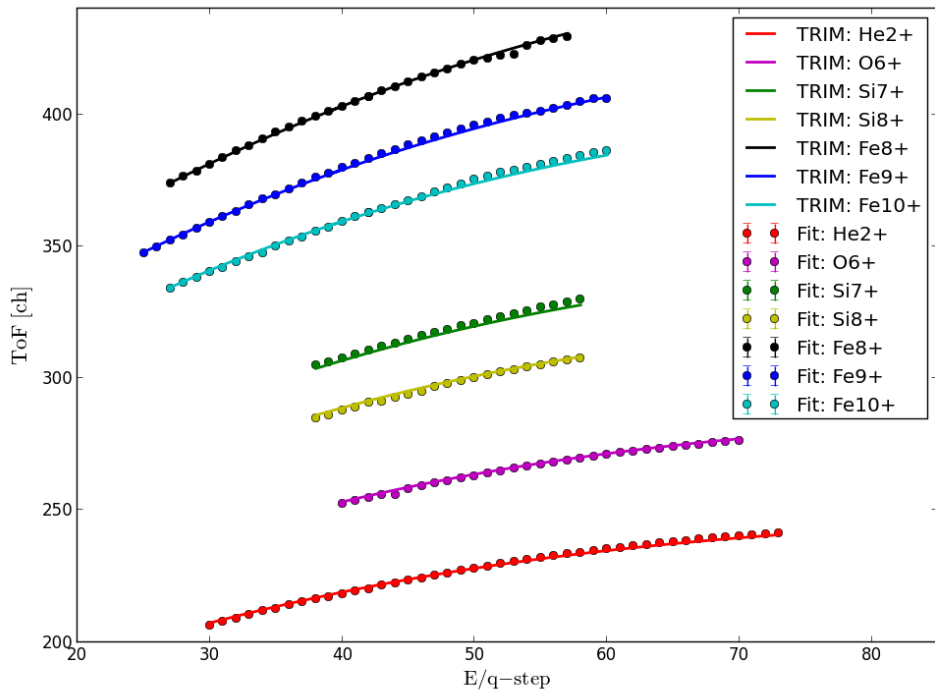


FIGURE 4.9: Comparison between fitted and simulated ToF-positions.

we compare the simulated with the fitted positions we find that they fit very well: Even if there are small systematic deviations in the case of  $Si^{7+}$  and  $Si^{8+}$  where the simulation constantly overestimates (underestimates) the fitted ToF-positions and also ions where the simulation partly under- and partly overestimates the fitted ToF-position such as  $He^{2+}$  and  $Fe^{10+}$  these deviations are in all cases not larger than 2 channels which is the diameter of the circles in the plot. Since 2 channels is the best achievable accuracy of the ToF-measurement in the case of the short-time data we conclude that within this desired accuracy the observed ToF positions are consistent with the time-of-flight calibration accomplished by [40]. Even if this result was expected it is a meaningful check

for the former calibration since with  $\text{Fe}^{8+}$ ,  $\text{Fe}^{9+}$ ,  $\text{Si}^{7+}$ ,  $\text{Si}^{8+}$  we added 4 additional ions which were not included in the original calibration.

#### 4.1.4 Calibration of the ToF Peak Widths

In principle the ToF signal width is influenced by several factors which are the velocity acceptance of the CTOF entrance system / electrostatic analyzer, the straggling in the foil and finally the read-out electronics signal width. While in the CTOF literature we could not find any hint that the read-out electronics could have a significant influence on the measured signal, the entrance system is described in detail in [35]. We therefore first calculate analytically the expected ToF signal width caused by the finite entrance system velocity acceptance and then compare it to the simulated TRIM widths. The convolution of both, theoretically should reproduce the fitted ToF widths. We find for the entrance window ToF-width contribution from the Gaussian error propagation formula

$$\sigma_y(x_i, \sigma_{x_i}) = \sqrt{\sum_i \left( \frac{\partial y}{\partial x_i} \cdot \sigma_{x_i} \right)^2} \quad (4.6)$$

and Eq. (3.5), (4.1):

$$\sigma_{ToF}^{ESA}[ch] = \left[ \Delta E_{rel} \cdot E_{in} \cdot \sqrt{\frac{m \cdot L_\tau^2}{8 \cdot E_{pc}^3}} - b_{ToF} \right] \cdot a_{ToF}^{-1} \quad (4.7)$$

where

$$\sigma_{E_{in}}/E_{in} = \Delta E_{rel} = 2 \cdot \Delta v_{rel} = 2.4\% \quad (4.8)$$

is the relative energy acceptance of the electrostatic analyzer,  $E_{in}$  is the incident energy of the ion *before* the post-acceleration and  $E_{pc}$  is the ion's energy after the carbon foil which can be calculated from Eq. (4.4). As before  $L_\tau$  is the length of the ToF section as explained in chapter 3. The obtained widths  $FWHM_{ToF} \approx 2.35 \cdot \sigma_{ToF}^{ESA}$  are plotted in figure 4.10. When we convolute these obtained widths with the TRIM widths resulting from carbonfoil straggling, which is done exemplary for iron at ESA step 50 in figure 4.11, we see that the entrance system contribution is negligible. For other ions this is also true because even when the obtained TRIM widths are smaller this is also the case for the analyzer contribution. Furthermore we compare the theoretical ToF-signal response (solid black curve) with the fitted peak shapes (green curve). Unfortunately the distribution widths differ by a factor of 2 even if the distribution shapes look similar

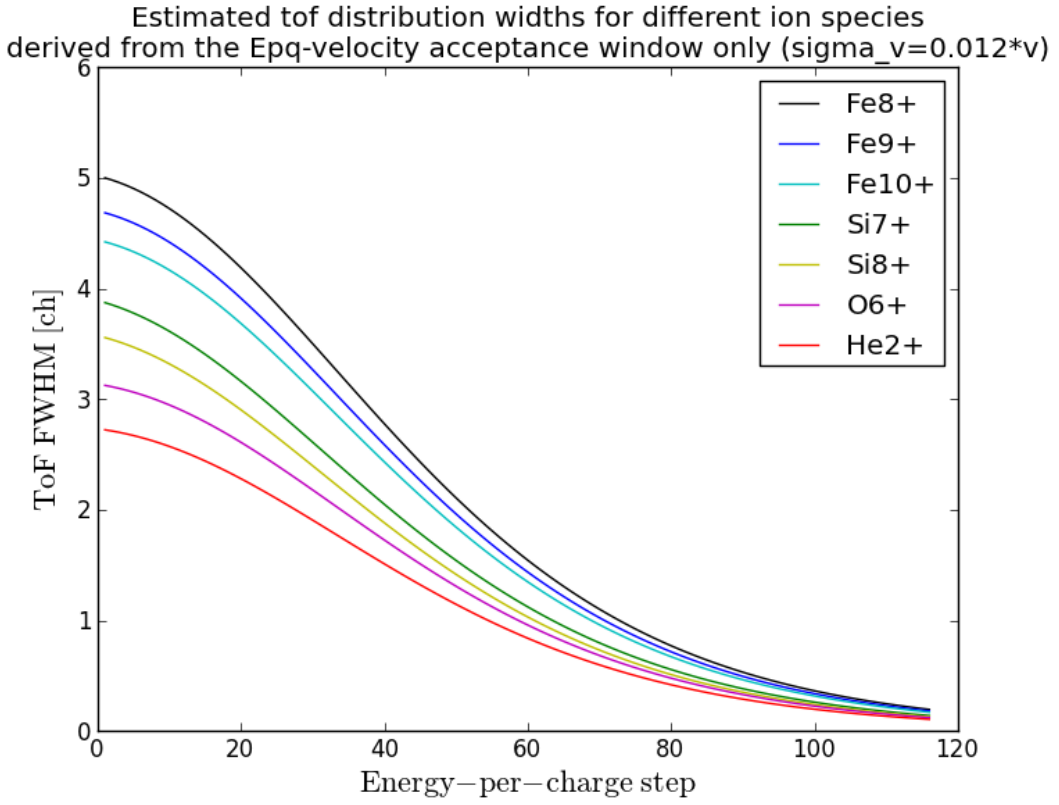


FIGURE 4.10: Calculated contribution of the entrance window to the measured ToF signal widths.

as shown in figure 4.11.

Therefore, we cannot use the TRIM predictions for the estimation of the ToF signal

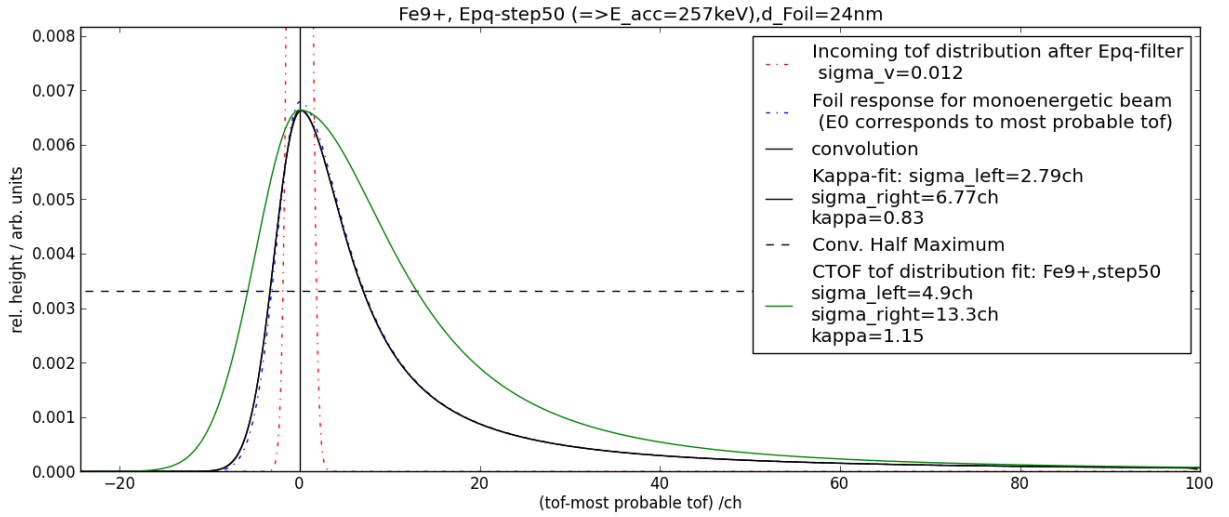


FIGURE 4.11: Comparison between fitted and simulated ToF-widths.

widths but instead we will follow an empirical approach which was already applied in

the in-flight calibration of similar instruments such as ACE/SWICS (Berger, pc: 2014) and which is to plot the fitted widths against the fitted most probable ToF values or equivalently against the incident velocity of the ions. As shown in figure (4.12) the ion velocity after the post-acceleration (and before the foil)  $v_{acc}$  is indeed the dominant parameter for the velocity loss in the foil since all ions almost perfectly line up to the linear fit and we get the linear relation:

$$\sigma_{ToF}[ch] = -0.0040 \cdot v_{acc} [km/s] + 10.28 \text{ ch} \quad (4.9)$$

The widths increase with decreasing ion velocity since the particles straggle more at low velocities due to the increase of the nuclear stopping power contribution.

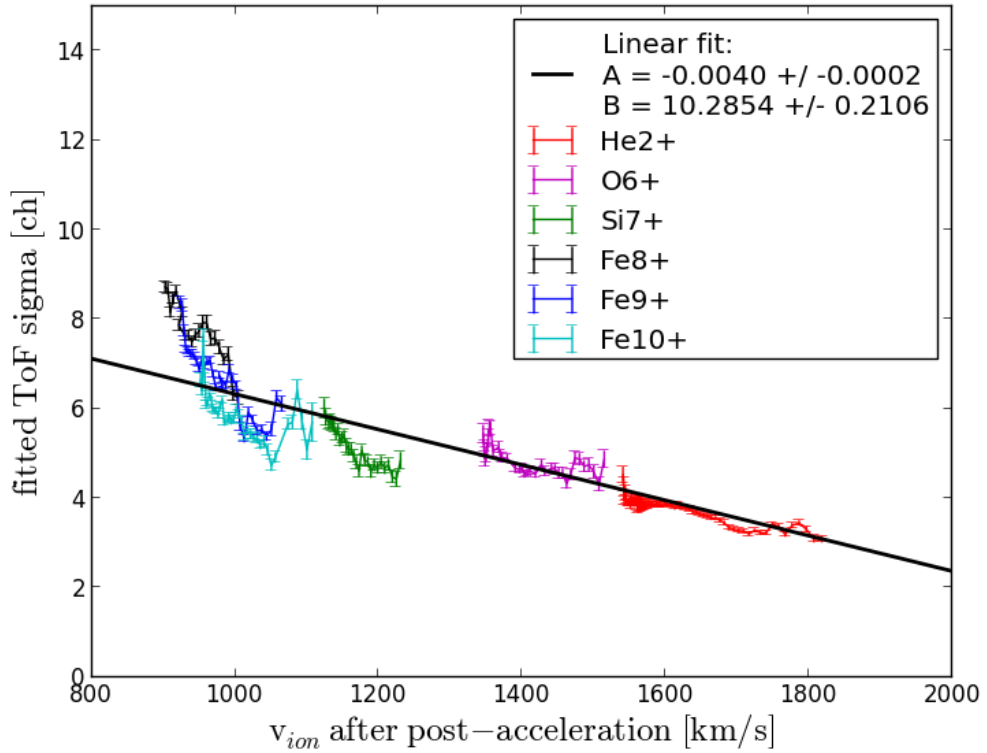


FIGURE 4.12: Time-of-flight signal sigmas.

## 4.2 Solid State Detector Calibration for Solar Wind Ions

### 4.2.1 SSD Calibration Model

We now come to the calibration of the residual energy measurement which is visualized on the y-axis of the ET-matrix. In chapter (1) we introduced the pulse height defect (PHD) which is responsible for the fact that the measured energy signal is not simply linearly related to the particle's energy prior to the foil which can be deduced from the already calibrated time-of-flight measurement by:

$$E_\tau = \frac{m \cdot L_\tau^2}{2} \cdot \tau^{-2} \quad (4.10)$$

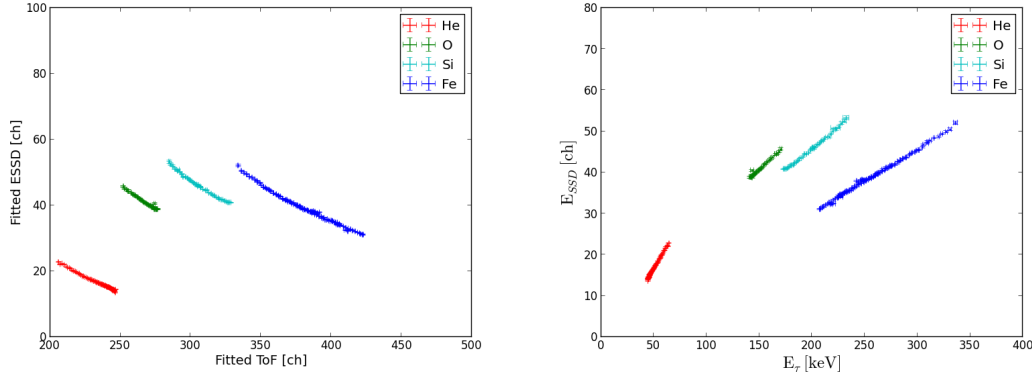


FIGURE 4.13: From the fitted ToF positions of the reference ions (left panel) the kinetic energy of the ions prior to the SSD  $E_\tau$  is calculated and plotted against the measured  $E_{SSD}$  channel (right panel). Obviously there is no universal linear calibration relation between the two quantities valid for all elements, which is the result of the discussed pulse height defect.

In fact the situation is more complicated as figure 4.13 illustrates the enormous effect of the PHD on the measured signal: Still assuming a linear conversion from energy channels to a physical unit

$$ESSD[\text{ch}] = A \cdot E_{\text{meas}}[\text{keV}] + B \quad (4.11)$$

and recalling the pulse height fraction  $\eta$  from chapter 3 as the complement of the PHD , we come up with the following calibration model for the measured energy signal

$$E_{SSD}[\text{ch}] = A \cdot \eta(Z, v) \cdot E_\tau[\text{keV}] + B \quad (4.12)$$

with universal constants A and B which have to be valid for all ions. In the following we abbreviate the term

$$\eta(Z, v) \cdot E_\tau =: E_{SSD}^{keV} \quad (4.13)$$

## 4.2.2 Simulation of the Energy Peak Positions with TRIM

### 4.2.2.1 Total Ionization Loss of Ions in the Silicon Layer

In order to precisely characterize the SSD response to incident ions, with the TRIM simulation we aim to calculate the most probable electronic energy loss within the sensitive SSD area. This quantity can deviate significantly from the mean value of the electronic ionization loss in the target, directly provided by TRIM, due to possible asymmetric electronic loss distributions in the SSD as documented in [36], [37]. Therefore, we have to calculate the complete electronic energy loss distributions for samples of the different incoming elements in analogy to the energy loss distributions of the carbon foil simulation. Unfortunately the TRIM program does not directly provide these distributions but it allows to track single ions through the target and, as shown below, one can make use of this feature to finally obtain the wanted electronic energy distributions for a sample size of 10000 particles within reasonable calculation time of a few minutes per distribution.

The TRIM simulation creates the optional output file *EXYZ* shown in figure A.1 in the appendix. In this file each ion is tracked through the target with a given energy increment as step size: For each step  $i$  the ion's remaining energy, and its position in the target in terms of the x-, y-, z-coordinate is given. In addition the average electronic stopping power over the last performed step  $(dE_{el}/dr)_i$  is specified and the ion's energy loss in the last recoil collision  $(\Delta E_{rec})_i$ . Choosing the increment to be small compared to its initial energy such as  $E_{inc} = 0.1$  keV we can follow all major changes in the particle energy since the electronic energy loss is modeled continuously and every recoil collision with an energy transfer of more than  $E_{inc}$  will be listed<sup>1</sup>. With these considerations the total energy losses both to target electrons and recoils can be obtained for each simulated ion by summing over the stepwise losses:

$$(\Delta E)_{rec} = \sum_{i=1}^N (\Delta E_{rec})_i \quad (4.14)$$

---

<sup>1</sup>Note that the energy step size is usually not exactly  $E_{inc}$ , because the energy losses occur in general in uneven steps, therefore the nearest occurring energy to each increment is used. For further details the reader is referred to the SRIM/TRIM Manual, chapter 9, page 14 [39].

and

$$(\Delta E)_{el} = \sum_{i=1}^N \left( \frac{dE_{el}}{dr} \right)_i \cdot \Delta r_i \quad (4.15)$$

with the ion path increments within the target

$$\Delta r_i = \sqrt{(x_i - x_{i-1})^2 + (y_i - y_{i-1})^2 + (z_i - z_{i-1})^2} \quad (4.16)$$

and  $N$  as the total number of incremental steps. In figure 4.14 the accumulated total energy losses  $(\Delta E)_{rec}$  and  $(\Delta E)_{el}$  are plotted against the projected ion path for a randomly selected helium ion with initial energy  $E_{in} = 60$  keV and similarly for an iron ion with initial energy  $E_{in} = 230$  keV. Calculating these quantities for a sample of ions

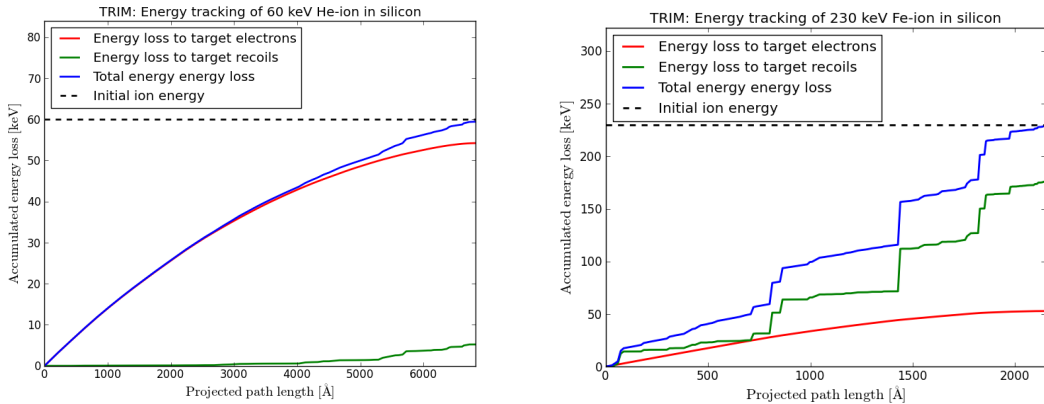


FIGURE 4.14: Exemplary energy loss of a fully stopped helium and iron ion in a silicon target.

and histogramming the individual energy losses we obtain distributions for the energy loss to the target electrons and recoils. These are shown in figure 4.15 for helium and iron for the same initial energies for which the single ion tracking was illustrated.

Unfortunately the calculated energy loss to the target electrons is not the full electronic energy loss of the ion, because as explained in chapter (1) the created target nuclei can start to travel by themselves after the collision with the incident ion if the energy transfer is larger than the target-specific *displacement energy*. These recoil nuclei in general also interact with the silicon target and ionize it. Thus the amount of energy lost by recoils to the target electrons has to be added to the ion electronic loss to get the *total electronic loss (TIL)* for each ion which we can express as

$$\Delta E_{TIL} = \Delta E_{el}^{ion} + \Delta E_{el}^{rec} = \sum_i^N \left( \frac{dE_{el}}{dr} \right)_i^{ion} \cdot \Delta r_i + \sum_i^N (\Delta E_{el}^{rec})_i . \quad (4.17)$$

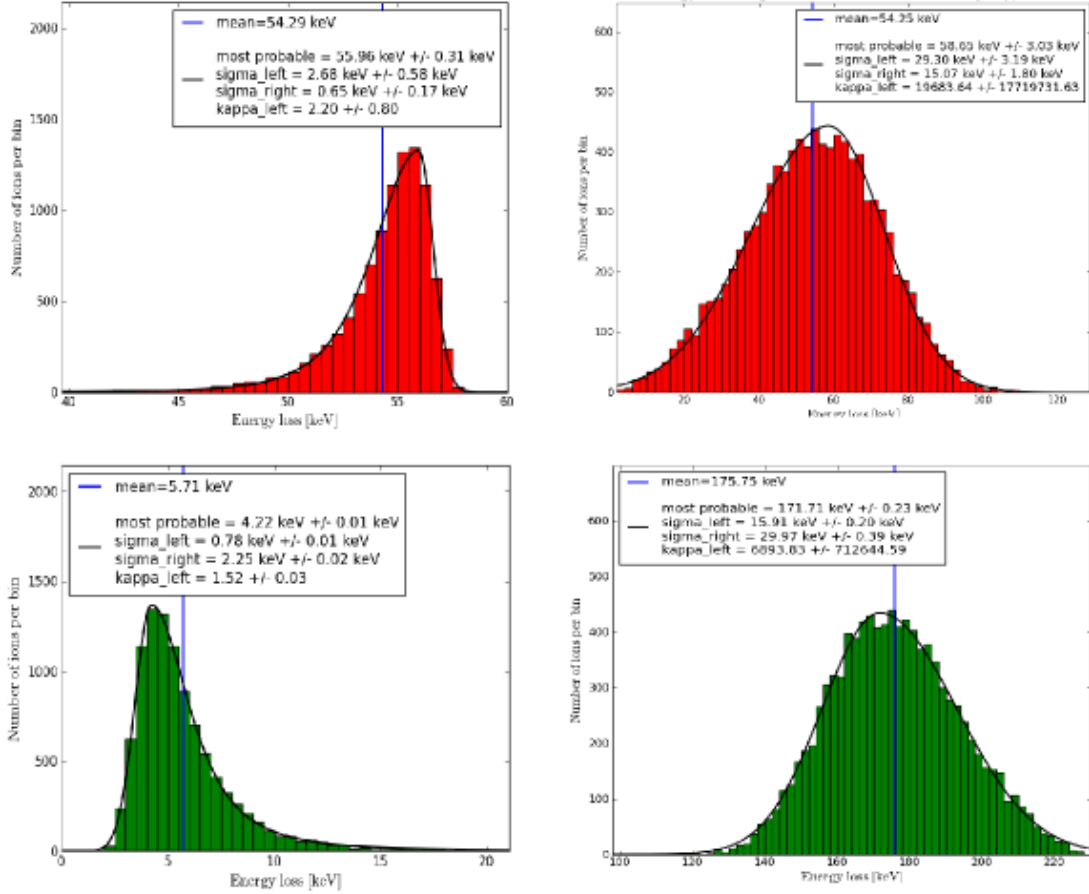


FIGURE 4.15: Energy loss of fully stopped helium (left panels) and iron (right panels) ions to the silicon target. Red histograms: energy loss to the target electrons. Green histograms: energy loss to the target nuclei eventually traveling through the target as recoils. While the ion's energy loss to recoils is small for helium, it even exceeds the electronic loss for iron at the selected initial energy.

which is just the numerical expression of Eq. (1.7) in chapter (1). Note that  $\Delta E_{el}^{rec}$  is the electronic loss of *all* target recoil ions created by a single incident ion. Even if we cannot calculate this quantity exactly without examining the full recoil cascades<sup>2</sup>, we can approximate this quantity by calculating the mean electronic loss  $\langle \Delta E_{el}^{rec} \rangle_i$  for each target recoil which is directly created by the incident ion, and which we therefore call 1<sup>st</sup>-order recoil, and finally summing over these energies:

$$\Delta E_{el}^{rec} \approx \sum_i^N \langle \Delta E_{el}^{rec} \rangle_i \quad (4.18)$$

The mean electronic loss of each 1<sup>st</sup>-order recoil can be derived when having in mind that all recoils are in fact silicon nuclei, traveling through the sensitive silicon layer of the solid state detector. In addition the recoil ion charge state, as explained in the

<sup>2</sup> which is rather not practicable for several thousand incident ions.

previous sections, does not play a role for the calculation of its energy loss and the initial recoil kinetic energy is just the difference between the transferred energy from the ion to the recoil and the displacement energy, which is for semiconductors of the order of 15 eV according to [39]. We thus get a relation between the energy transferred to a 1<sup>st</sup>-order recoil at simulation step  $i$  and the initial recoil energy  $E_{rec,i}$ :

$$E_{rec,i} = \Delta E_{rec,i} - E_{disp} \quad (4.19)$$

Consequently we can simulate the (energy-dependent) mean electronic loss of these silicon recoils by simply simulating the electronic energy loss of silicon ions in a silicon target with TRIM where the upper limit for the recoil energy is given by the incident ion's energy. In figure 4.16 the TRIM result for the electronic recoil energy loss is plotted in terms of the mean relative electronic loss  $\eta_{rec}^{el}$  of silicon ions in an infinite silicon target in dependence of the initial recoil energy  $E_{rec,i}$ :

$$\eta_{rec}^{el}(E_{rec,i}) = \frac{\langle \Delta E_{rec,i}^{el}(E_{rec,i}) \rangle}{E_{rec,i}}. \quad (4.20)$$

We observe a monotonic increase of the electronic energy loss fraction with increasing initial recoil energy which is expected since the ratio between electronic and nuclear stopping power increases for a given element with increasing particle velocity.

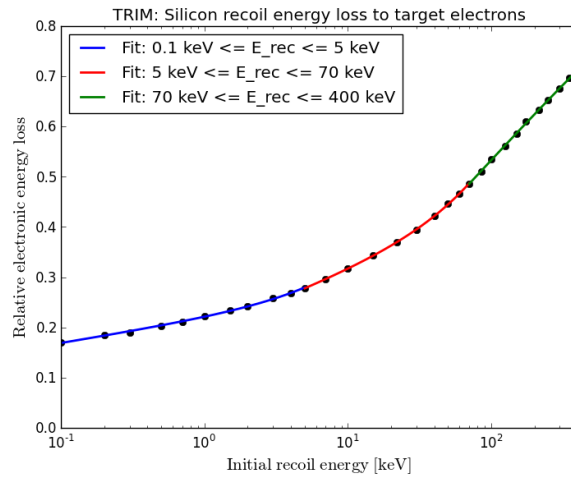


FIGURE 4.16: Relative electronic energy loss of silicon ions in silicon, acting as artificial recoils. The different colors mark the region of different fit-functions applied which nevertheless had to form a continuous curve.

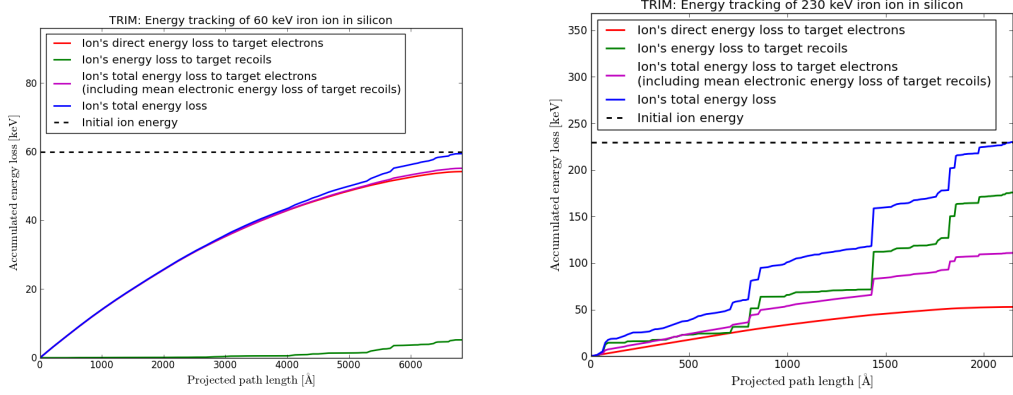


FIGURE 4.17: Exemplary energy loss of a fully stopped helium and iron ion in a silicon target. The magenta line is the calculated total ionization loss of the ion.

Given  $\eta_{rec}^{el}$  we can now approximate electronic energy loss of all silicon recoils created by a single incident ion by:

$$\Delta E_{rec}^{el} \approx \sum_i^N E_{rec,i} \cdot \eta_{rec}^{el} (E_{rec,i}) \quad (4.21)$$

By adding this to the direct electronic loss of the incident ion, calculated in Eq. (4.17), we get for the total ionization loss of each ion

$$\Delta E_{TIL} = \Delta E_{ion}^{el} + \Delta E_{rec}^{el} \approx \sum_i^N \left[ \left( \frac{dE_{el}}{dr} \right)_i \cdot \Delta r_i + E_{rec,i} \cdot \eta_{rec}^{el} (E_{rec,i}) \right] \quad (4.22)$$

The obtained total ionization loss is plotted in figure 4.17 in the lower panel for the for-

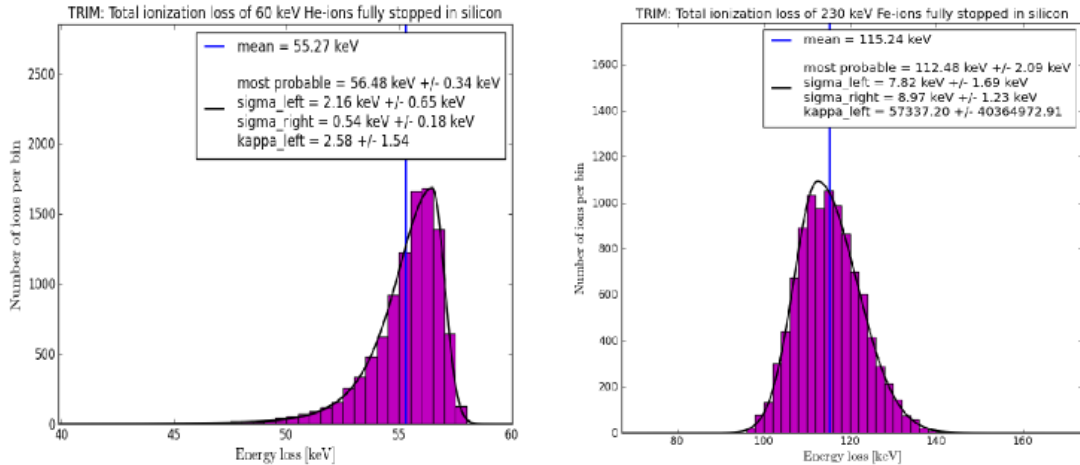


FIGURE 4.18: Total ionization loss spectra for 60 keV helium ions and 230 keV iron ions, which fully stop in silicon.

mer selected helium and iron ions. In figure 4.18 the respective total electronic energy

loss spectra are plotted. Comparing these to the spectra in figure 4.15 the electronic energy loss of the silicon recoils provides only an insignificant small correction of less than 1 % to the most probable total ionization loss of helium at an incident energy of 60 keV while it provides a correction of 107 %(!) to the total ionization loss of iron at an incident energy of 230 keV, showing that the effect of ionizing recoils cannot be neglected to determine the SSD-response for the heavier ions. We also checked the whole simulation method by calculating the mean of the derived total ionization loss spectra and comparing it to the mean ionization loss directly derived by TRIM. Both values matched within 3% of the obtained total ionization loss for all investigated elements in the relevant energy range below 400 keV.

#### 4.2.2.2 Simulation of the SSD Dead-Layer

So far we have not included the front contact dead-layer of the solid state detector in the simulation. Following [37] the dead-layer material is silicon-dioxide ( $\text{SiO}_2$ ) and has a nominal thickness of 500 Å. In the TRIM window it is possible to select  $\text{SiO}_2$  among the target materials. The  $\text{SiO}_2$  layer is stacked in front of the silicon layer so that we simulate now a 2-layer target representing the complete CTOF SSD.

The electronic energy loss for each incident ion is calculated as in the previous section except for the fact that we only summarize over the stepwise energy losses in the sensitive silicon layer, by setting the condition that for all relevant steps the ion's current penetration depth  $x_i$  has to be larger than the layer thickness:

$$\Delta E_{TIL} = \sum_{x_i > d_{\text{SiO}_2}}^N \left[ \left( \frac{dE_{el}}{dr} \right)_i \cdot \Delta r_i + E_{rec,i} \cdot \eta_{rec}^{el}(E_{rec,i}) \right] \quad (4.23)$$

In figure 4.19 the resulting total ionization loss spectra are plotted for helium and oxygen at two different initial energies, respectively. As expected the total ionization loss which is equivalent to the measured pulse height fraction decreases for helium and iron compared to the situation without dead-layer in figure 4.18. While the shape of the energy loss distribution stays close to a Gaussian for the helium ions at both energies, the distribution develops asymmetric tails towards lower electronic losses for the heavier iron ions which can be explained by a fraction of incident ions losing a large part of their energy already in the dead-layer. This is exactly the same phenomenon as observed in the carbon foil but it develops even stronger since the dead-layer is about twice as thick of the carbon foil while having comparable values in density and atomic number of its constituent atoms.

In a CELIAS/CTOF pre-flight study [43] it is stated that the measured PIPS detec-

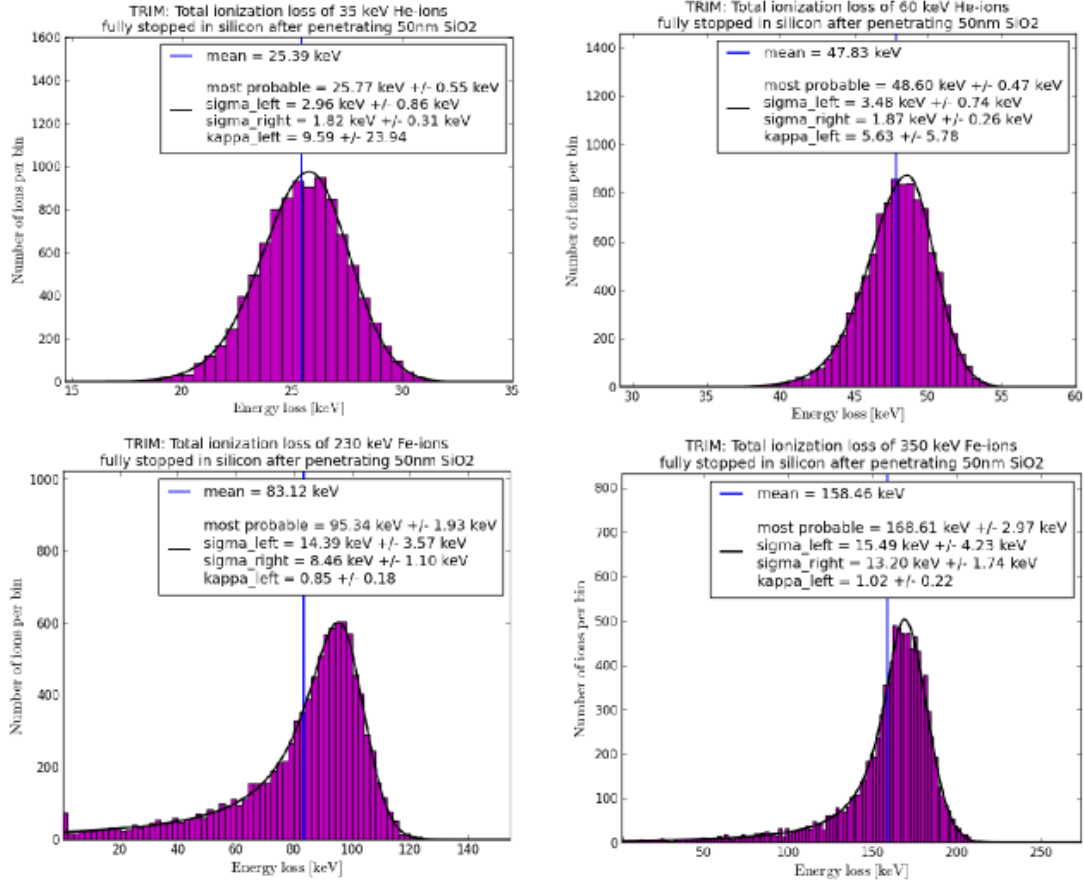


FIGURE 4.19: Total ionization loss of helium (upper panels) and iron (lower panels) in the sensitive silicon layer at different incident energies after penetrating a 50 nm SiO<sub>2</sub> dead-layer.

tor signal could be better reproduced with TRIM when assuming an SiO<sub>2</sub>-dead-layer thickness of 75 nm instead of the nominal thickness of 50 nm. Therefore, we will perform simulations with different dead-layer thicknesses to search for the best agreement with the fitted long-time data. In figure 4.20 the influence of the dead-layer thickness is illustrated by plotting the total electronic energy loss for helium and iron for two different thicknesses of  $d_1 = 25$  nm and  $d_2 = 75$  nm both deviating by 50% from the nominal thickness. For 230 keV iron we observe a change in the most probable value of the total ionization loss from 95 keV to 86 keV (104 keV) when changing the SiO<sub>2</sub>-layer thickness to 75 nm (25 nm), which changes the PHF about  $\pm 0.04$  from 0.41 to 0.37 (0.45). For helium at 60 keV initial energy the PHF even changes about  $-0.07$  ( $+0.05$ ) from 0.81 to 0.74 (0.86) when increasing (decreasing) the dead-layer thickness by 25 nm. Furthermore an increase of the dead-layer thickness comes with larger signal widths and more pronounced tails, so that very large thicknesses above 100 nm lead to a dramatic drop in resolution making such a choice highly improbable.

Finally we consider that TRIM does not simulate any channeling effects, so that in the given detector geometry the variation of the incident angle  $\alpha_{in}$  in the simulation has the

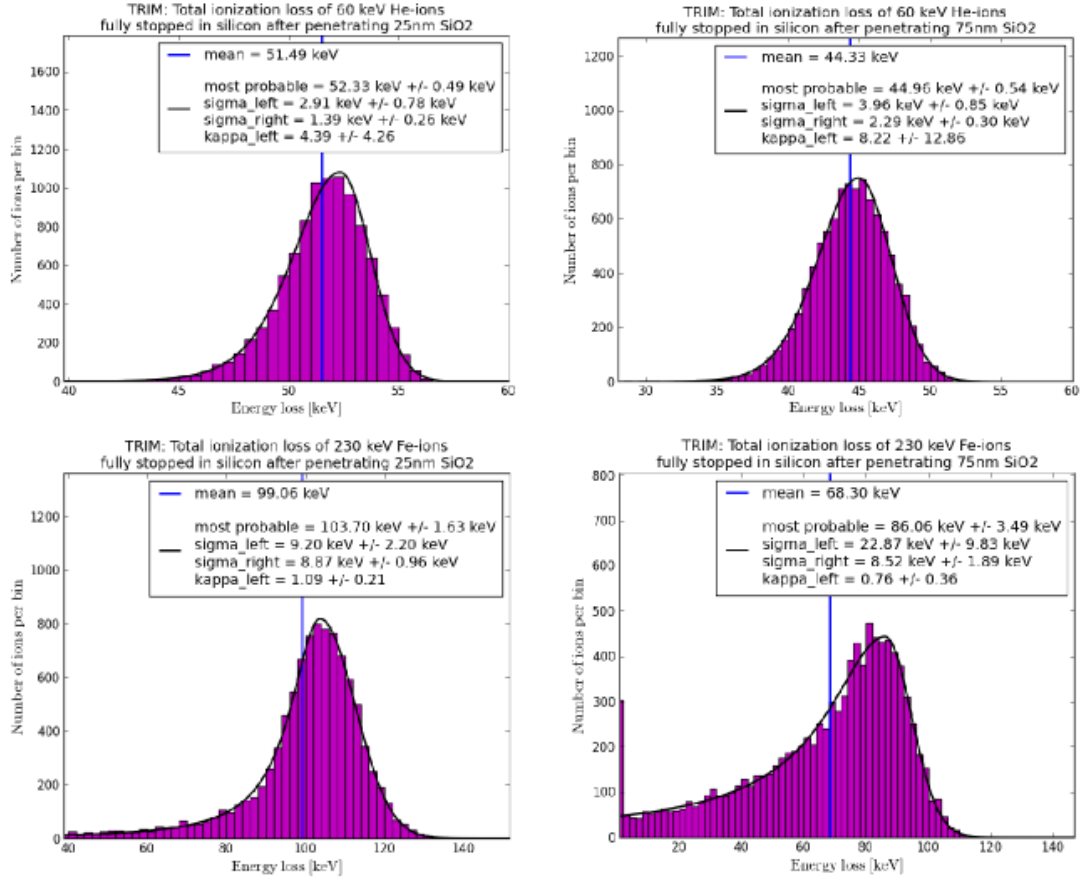


FIGURE 4.20: Total ionization loss spectra for 60 keV helium ions (upper panels) and 230 keV iron ions after penetrating a 25 nm (left panels) and a 75 nm (right panels) SiO<sub>2</sub> dead-layer.

only effect of increasing the effective dead-layer thickness because the mean effective path  $\langle r_{ion}^{SiO_2} \rangle$  of the incident ions in the dead-layer (and in the carbon foil, respectively) increases as function of  $\alpha_{in}$ :

$$\langle r_{ion}^{SiO_2}(\alpha_{in}) \rangle = \frac{\langle r_{ion}^{SiO_2}(0) \rangle}{\cos(\alpha_{in})} , \quad -\pi/2 < \alpha_{in} < \pi/2 . \quad (4.24)$$

We immediately see that this effect can be neglected since even a very large declination of the incoming ions of  $\alpha_{in} = 10^\circ$  from the SSD axis only yields a relative path length increase of 1.5% in the SiO<sub>2</sub>-layer, which is much less than the uncertainty in dead-layer thickness as discussed above.

When comparing the simulated peak shapes in energy with the observed CTOF peak shapes we find that surprisingly in the data there is no evidence for asymmetries in the energy direction even if we observe such tails in the ToF direction. We still cannot give an explanation for that phenomenon but the same qualitative difference between simulation and measurement was observed by [37] and [36], as well.

### 4.2.2.3 Influence of Carbon Foil and Entrance System on the SSD Signal

After setting up the simulation of the complete solid state detector in the previous section, in this final step we aim to simulate the particles' passage through the carbon foil and the SSD in one integrated simulation set-up. This makes it possible to take into account that the particles entering the SSD do not represent a mono-energetic beam as assumed in the previous sections but instead were already scattered in the carbon foil and thus arrive as non-trivial distributions in energy with widths up to 15 keV (compare also figure 4.7) at the SSD. In the simulation the carbon foil is stacked in front of the SSD with the same nominal thickness of 24 nm as in section (4.2.2.2). The resulting spectra are shown in figure 4.21 on the left. The incoming helium and iron energies

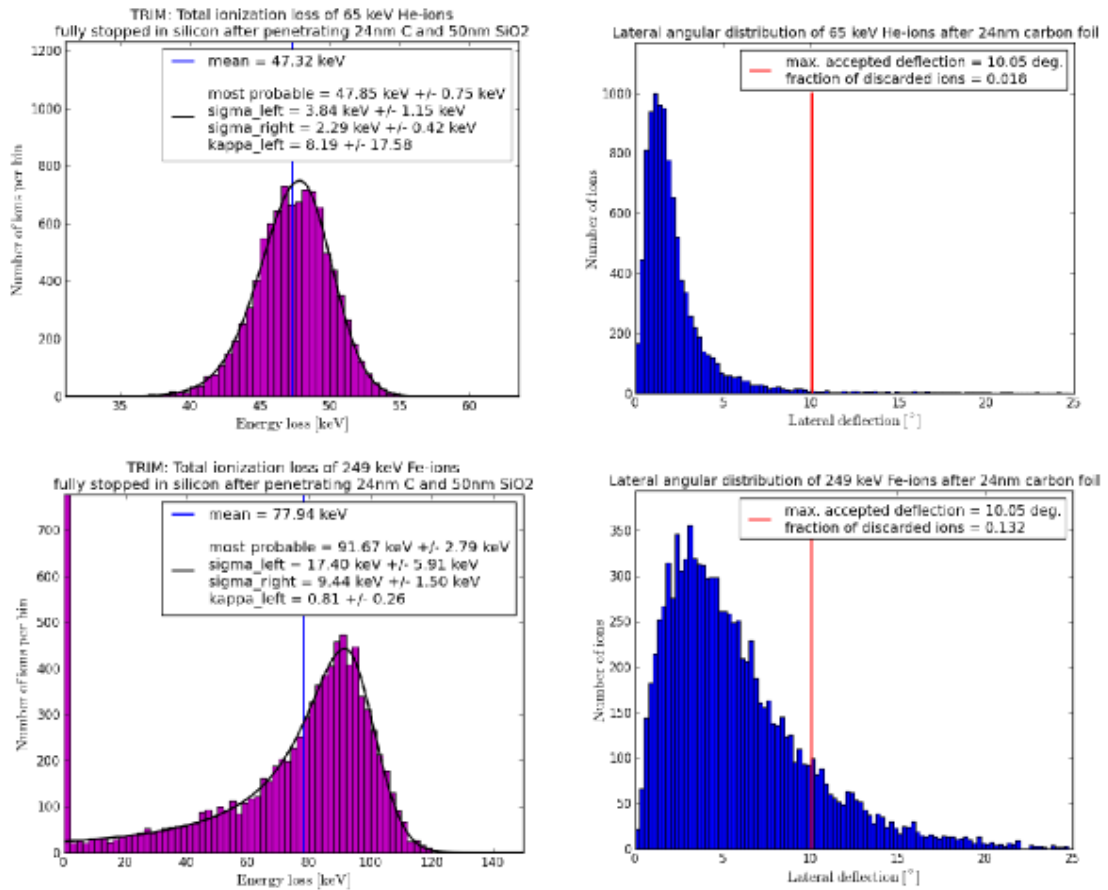


FIGURE 4.21: Left: Total ionization loss spectra for 65 keV helium ions (upper panel) and 249 keV iron ions (lower panel) after penetrating both a 24 nm carbon foil and a 50 nm SiO<sub>2</sub> dead-layer. Right: Lateral angular distribution after the ions' passage through the carbon foil. The ions with an angular deflection larger than 10.05° are excluded from further tracking in the simulation and end up in the zero-energy bin of the obtained spectra on the left.

prior to the carbon foil of 65 keV and 249 keV correspond to most probable residual energy values of 60 keV and 230 keV after the foil ,respectively, so that the obtained

electronic energy loss spectra should be compared directly to the spectra of figure 4.19. We observe only slight shifts in the most probable electronic energy loss for helium of about 1 keV and for iron of about 4 keV and as expected also the distribution sigmas increase when including the carbon foil in the simulation.

Note that when integrating the carbon foil in the simulation we paid attention to discard particles that are deflected in the foil more than the critical angle to reach the circular surface of the SSD. This critical angle can be calculated as

$$\theta_{max} = \arctan \left( \frac{r_{SSD}}{L_{ToF}} \right) = 10.1^\circ \quad (4.25)$$

with  $r_{SSD} = 1.25$  cm (after H. Grünwaldt, pc: 2014) as the SSD surface radius and  $L_{ToF} = 7.05$  cm as the length of the ToF-section. For each simulated ion its lateral deflection from the incoming x-direction is calculated from its last two positions within the carbon foil:

$$\theta = \arctan \left( \frac{\sqrt{(y_i - y_{i-1})^2 + (z_i - z_{i-1})^2}}{x_i - x_{i-1}} \right) \quad (4.26)$$

If  $\theta > \theta_{max}$  the particle's energy loss in the SSD layers was set to zero. On the right of figure 4.21 the lateral angular distribution is plotted from which we can see that while for the weakly scattering helium ions the fraction of discarded particles is less than 2% this fraction is about 13% for the iron ions. These strongly scattered particles consequently fill the zero-energy bin in the energy loss spectra on the left.

As shown in the ToF width calibration the influence of the entrance system on the ion's energy spectrum after the carbon foil could be neglected. Therefore, we do not consider it here anymore when even the scattering in the carbon foil has very small effects. Having considered the two layers of the solid state detector, the carbon foil and the velocity acceptance of the entrance system we have developed a comprehensive model of the complete CTOF sensor within the possibilities of the TRIM simulation framework which, nevertheless, has its limitations in terms of target modeling compared to other software packages such as GEANT 4. However, it is rather questionable whether a more complex simulation of the detector is helpful in our situation since with the not accurately known dead-layer thickness we already have an additional degree of freedom in the simulation and adding further parts of the detector when only having limited documentation of its components and of the pre-flight calibration seems rather speculative.

### 4.2.3 SSD Simulation Results

We now present the pulse height fractions (PHFs) which we obtain from the simulations by dividing the most probable electronic energy loss  $E_{SSD}$  by the most probable incoming ion energy  $E_\tau$ , obtained from the ToF measurement. In figure 4.22 we plotted the simulated PHFs for the nominal dead-layer thickness of 50 nm against the initial energy-per-nucleon of the reference elements before they enter the SSD which is equal to the ion's velocity squared. As expected the simulation yields an increasing PHF for

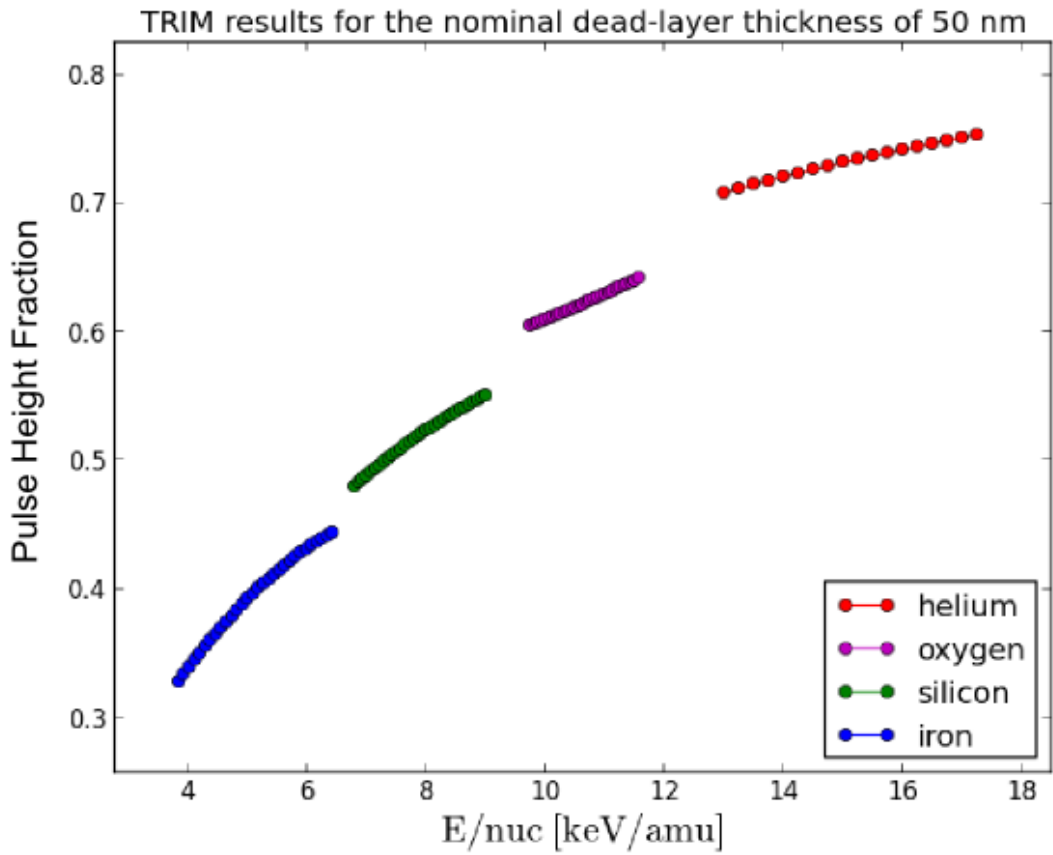


FIGURE 4.22: Simulated pulse height fractions for the reference elements with an assumed SiO<sub>2</sub> dead-layer thickness of 50 nm.

all elements with increasing energy-per-nucleon and higher PHFs for the lighter elements at a given energy-per-nucleon. In figure 4.23 we plotted the obtained PHFs for different SiO<sub>2</sub>-dead-layer thicknesses of 1 nm, 25 nm, 50 nm, 75 nm and 100 nm. In accordance with the examples in figure 4.20 of the previous section, for all ions the PHFs decrease with increasing dead-layer thickness. However, we note that the decrease is stronger for the lighter ions than for the heavier ions. This leads to the effect that for

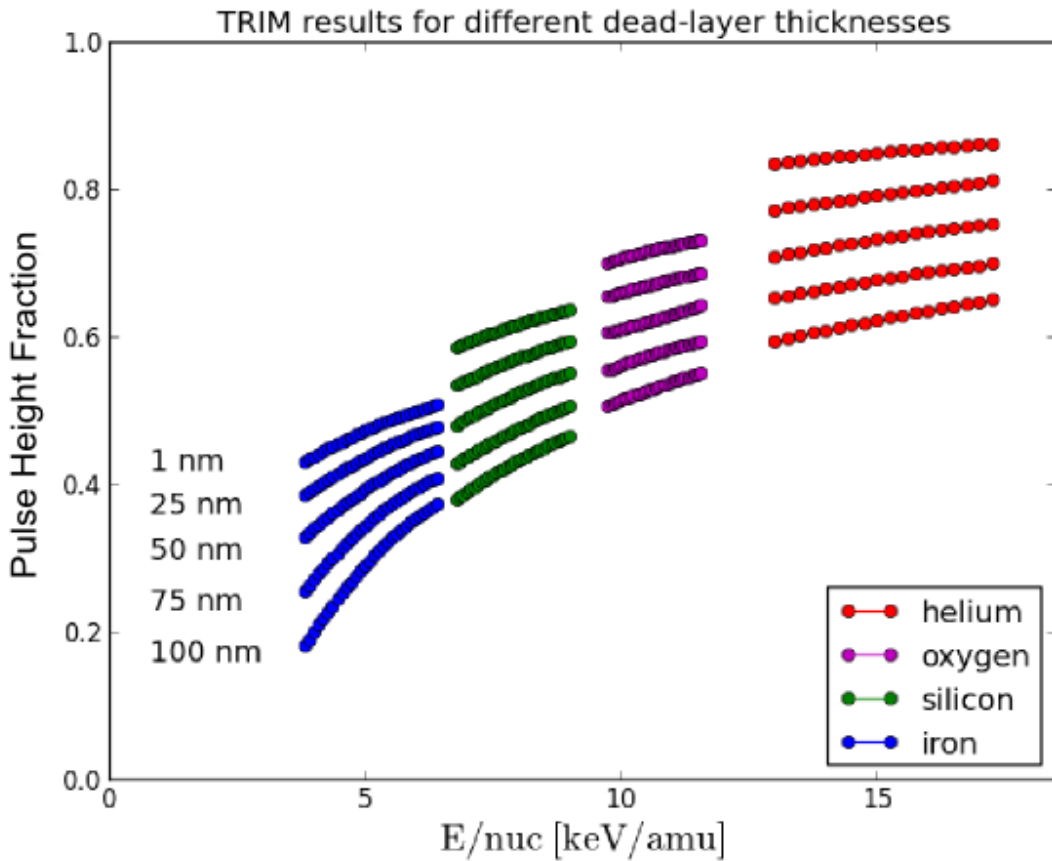


FIGURE 4.23: Simulated pulse height fractions for the reference elements for several SiO<sub>2</sub>-dead-layer thicknesses of  $1 \text{ nm} \leq d_{\text{SiO}_2} \leq 100 \text{ nm}$ .

small dead-layer thicknesses of 25 nm and less the PHF also shows a significant dependence on the atomic number of the element, while for higher dead-layer thicknesses of 75 nm and more this dependence almost vanishes.

With the calculated PHFs we can use Eq. (4.13) to calculate the theoretical energy response of the SSD and plot it against the actually measured energy signal to finally obtain the conversion from energy channel to keV after (4.12). This is done in figure 4.24 for the nominal dead-layer thickness of 50 nm and in figure 4.25 for all five simulated dead-layer thicknesses. As can be seen the data can not be fitted to a single straight calibration line even if the points lie much closer together than in figure 4.13. This means that the simulation qualitatively corrects the initial energy for the PHF in the right sense but is quantitatively not fully consistent with the measured signals, so that it is impossible to find universal calibration constants  $A$  and  $B$  for a linear conversion from the theoretically expected signal (in keV) to the measured signal (in channel) for all reference ions. As figure 4.25 shows, this does not change when varying the dead-layer thickness from a value of 1 nm up to 100 nm.

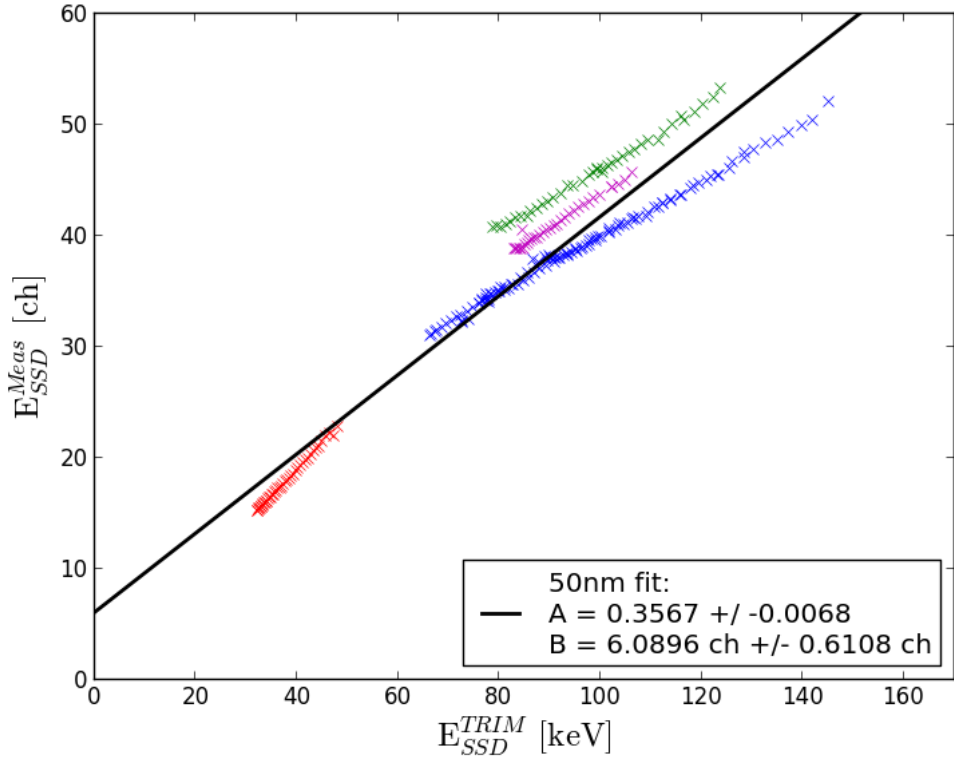


FIGURE 4.24: Actually deposited total ionization energy in the SSD (in channels) obtained from fits plotted against the simulated total ionization energy (in keV) deposited in the SSD for a dead-layer thickness of 50 nm. The black line represents the best linear fit to the data.

Having considered several effects such as the ionization loss of the silicon recoils, the influence of the carbon foil and a varying dead-layer thickness we conclude that the TRIM model at least in the assumed still simplified detector set-up cannot deliver accurate consistent results for all elements. However, before discussing this point in the following section, we recall the fact that we just need to have an accurate PHD estimation for one element to obtain the missing calibration constants  $A$  and  $B$ , so we have to evaluate the most reliable candidate of the calculated elements. Looking at the single PHD curves for the different elements in figure 4.25 one can estimate that the individual offset parameters of oxygen and silicon are around  $B \approx 15$  ch already for a dead-layer thickness of 1 nm. Regarding the fact that helium is measured also at channels at and slightly below 15 keV, this would lead to zero or even negative incident energies of some helium ions if the model for oxygen and silicon were correct. Thus we have to stick to helium or iron in order to find a meaningful calibration constant. Helium, as the only noble gas among our reference elements, is by far the easiest accessible element for laboratory experiments and should be also the easiest to model. The fact that we are

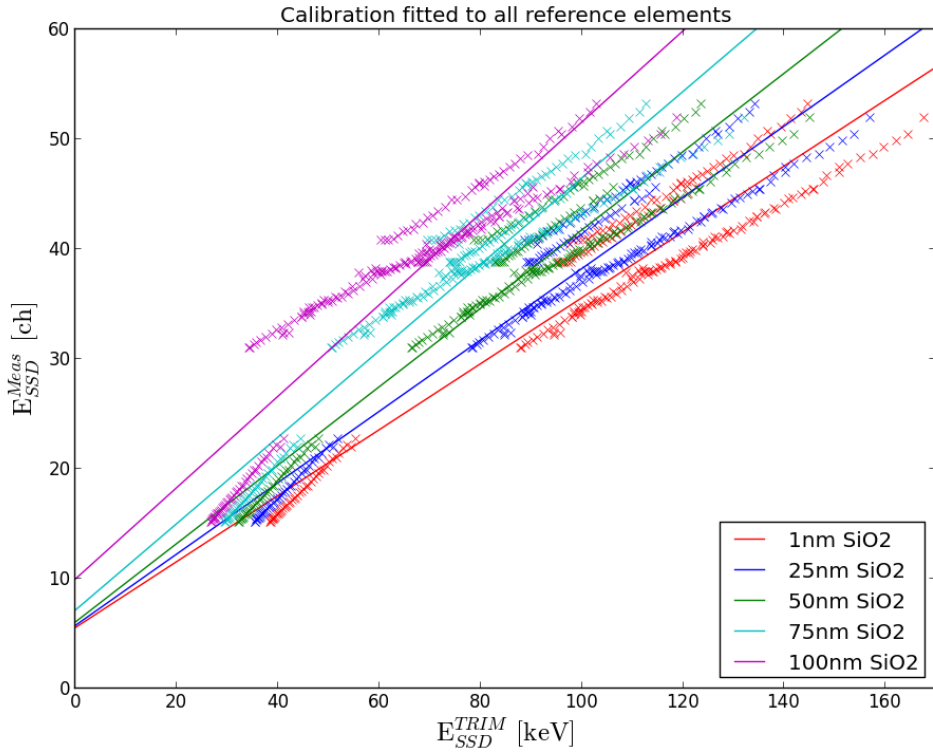


FIGURE 4.25: Actually deposited total ionization energy in the SSD (in channels) obtained from fits plotted against the simulated total ionization energy (in keV) deposited in the SSD for several dead-layer thicknesses of  $1 \text{ nm} \leq d_{\text{SiO}_2} \leq 100 \text{ nm}$ . The solid lines represent the best linear fits to the respective data.

operating at the low energy-per-nucleon range of validity and helium due to its small mass is measured at the highest energy-per-nucleon values among all measured ions additionally supports this point. From figure A.2 - A.6 in the appendix we can see the large difference in quantity of measurements between the different ions to which the TRIM model was compared: In the energy range below 20 keV/nuc we have about 20 independent data sets (among them 2 measured with a silicon target) for helium where we have only 2 for iron in that energy range, but neither of these is actually measured with a silicon target.

Therefore, we choose the following approach: We fit the SSD calibration constants  $A$  and  $B$  only to the helium data but then use the other elements as indicator for the most probable dead-layer thickness by taking them into account in the reduced  $\chi^2$  calculation.

This is done in figure 4.26 where we find a most probable dead-layer thickness of 75 nm which is 50% thicker than the nominal thickness. The derived calibration constants are then  $A := A_{He} = 0.5098 \pm 0.0035 \text{ ch/keV}$  and  $B := B_{He} = 0.02 \pm 0.12 \text{ ch}$ . Since the obtained offset value is very small compared to a critical accuracy of 2 channels and its

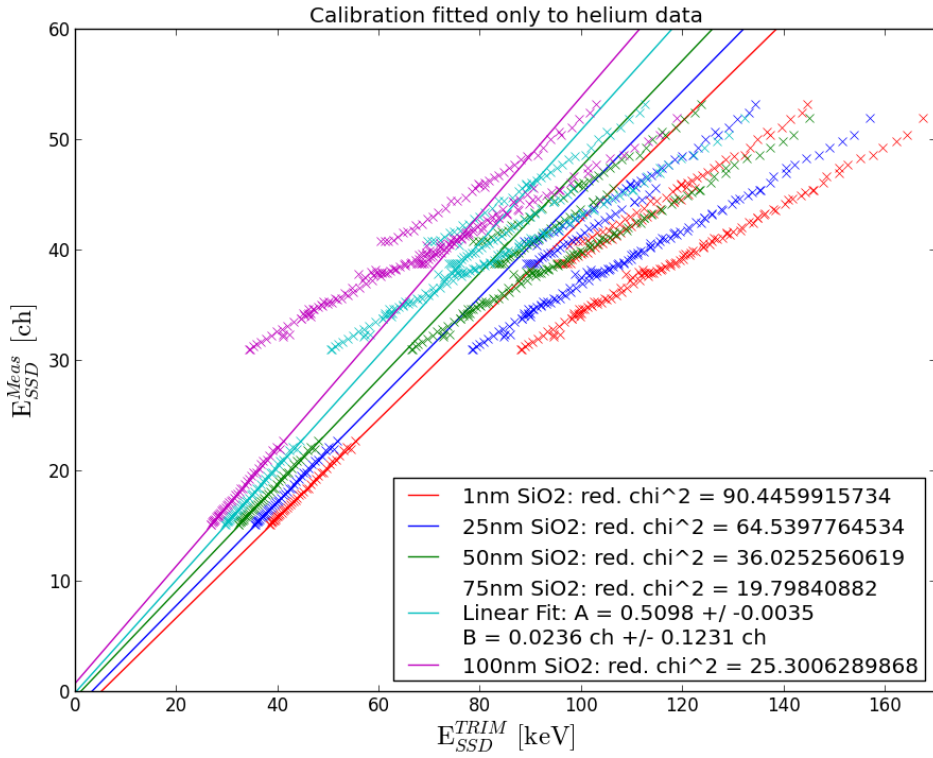


FIGURE 4.26: Actually deposited total ionization energy in the SSD (in channels) obtained from fits plotted against the simulated total ionization energy deposited in the SSD (in keV) for several dead-layer thickness of  $1 \text{ nm} \leq d_{SiO2} \leq 100 \text{ nm}$ . The solid lines represent the best linear fits to the helium data only. Nevertheless, the calculated reduced  $\chi^2$  in which all reference elements are included indicates how good the other ions fit to the helium fit for the respective dead-layer thickness.  $\chi^2$  is minimized for a dead-layer thickness of 75 nm for which the obtained calibration constants  $A$  and  $B$  are given.

uncertainty is about one order of magnitude larger than itself we can set this value to zero, so that  $B := 0 \text{ ch}$ .

#### 4.2.3.1 Comparison with Pre-flight Calibration Data

With the obtained calibration constants we can now also calculate the measured pulse height fractions for oxygen, silicon and iron as graphically shown in figure 4.28. These are plotted together with their individual simulated PHF curve in figure 4.27 on the left. By definition the helium curve is identical for measurement and simulation while for the other elements we find maximum deviations of less than 5% for oxygen, of about 5% for silicon and up to 10% for iron. An apparent difference between the simulation and the measured data of the heavier elements is the fact that the simulation predicts a strong continuous decrease of the PHF with decreasing velocity while the measured signal in this energy-per-nucleon range shows no dependency on the velocity at all.

This leads to relatively large deviations in particular for iron at energy-per-nucleon values around 6 keV/nuc, where the simulations overestimates the PHF, while the deviations vanish at values around 4 keV/nuc. In order to cross-check and discuss these

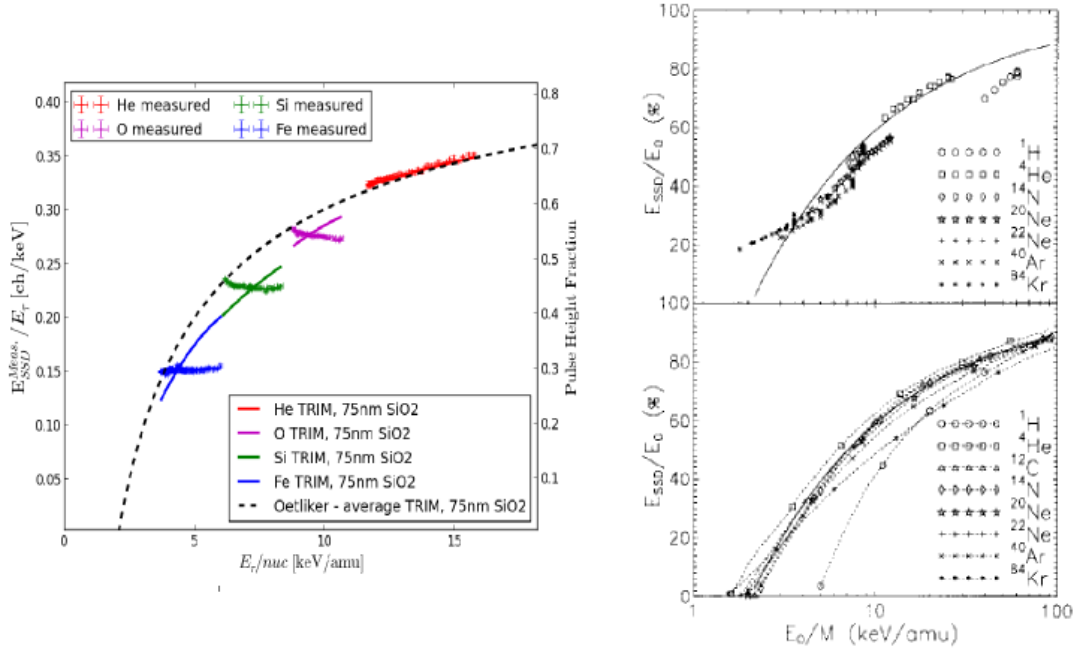


FIGURE 4.27: Comparison of the obtained pulse height fractions in this work (left panel) and in a CTOF pre-flight study by M. Oetliker (1993) [43] (right panels).

deviations between measurements and simulation we can compare our results with the results of a paper by M. Oetliker [43] who actually measured a prototype of the SSD later implemented in CTOF and also simulated it with TRIM. The SSD was also a Passivated Implanted Planar Silicon (PIPS) detector with SiO<sub>2</sub> dead-layer of nominal thickness of 50 nm, however, it was found that the SSD response could be better modeled with the assumption of a dead-layer thickness of 75 nm which is in agreement with our findings. In figure 4.27 in the right upper panel which is taken from the cited paper we see the measured signals for several ions produced by a laboratory ion source while the plotted solid curve is an average of the simulated signals with TRIM for all occurring elements. Note that this curve is explicitly given in [43] and therefore could be plotted as the dotted black curve in the left panel of figure 4.27. In the lower right panel all simulation curves for the different elements of [43] are plotted.

The most important point is that both the helium measurements by Oetliker and our simulation and measurement results for helium match very well the average black solid curve and both helium data sets lie at the same energies, when paying attention to the logarithmic scaling of the x-axis in the right plot. Therefore, we can conclude that our obtained pulse height fraction for helium is in very good agreement with the actually

measured pulse height defect in the pre-flight calibration with the CTOF-prototype SSD. This can be seen as direct proof for the correctness of the calibration if one supposes a very similar response between the CTOF SSD and its prototype, which is a reasonable assumption.

Secondly, despite the fact that the Oetliker average curve cannot be directly compared to our individual curves, which were even obtained for different ions, we see that both show qualitatively the same behavior compared to the measurements of the heavier ions such as iron, argon and krypton in the point that TRIM predicts a much stronger dependency on the ion velocity than it is measured. However, for neon which has an atomic number in between those of oxygen and silicon the slope of the measurements by Oetliker agrees well with the simulations which is not the case for the solar wind ions we modeled, but note that the performed measurements for neon were done over a wider energy range than our oxygen and silicon measurements.

#### 4.2.4 SSD Calibration Results

In the previous section the performed calibration could be corroborated by pre-flight measurements, but the critical proof for the quality of the in-flight calibration still has to be given by the successful prediction of the energy position of ions other than the reference ions, which is the objective of this section.

We now perform the final step in the energy signal calibration, which is the interpolation of all elemental PHFs from the reference element PHFs. As shown in figure 4.28, with the given SSD constants  $A$  and  $B$  we can convert the measured energy signals (in channels) for oxygen, silicon and iron to physical pulse height fractions. We thus obtain PHFs of 0.542, 0.448 and 0.296 for oxygen, silicon and iron, respectively. Note that these PHFs are not velocity dependent in the ambient energy range in contrast to the helium PHF which varies between 0.63 and 0.70 in dependence of the helium incident velocity. By additional calibration fits of the carbon  $C^{5+}$  peak we can show that even this second lightest ion of interest shows no dependency of the PHF on the ion velocity. As a consequence we can neglect this dependency for all heavy ions except for helium and interpolate the elemental PHFs simply as a function of the atomic number for  $Z > 2$  as illustrated in figure 4.28 in the right panel.

We selected all elements as relevant for our first studies which have elemental coronal abundances not smaller than two orders of magnitude less than oxygen, as well as calcium which is below but close to that limit and its atomic number lies nicely in between those of sulfur and iron. The coronal abundances are taken from [30]. The

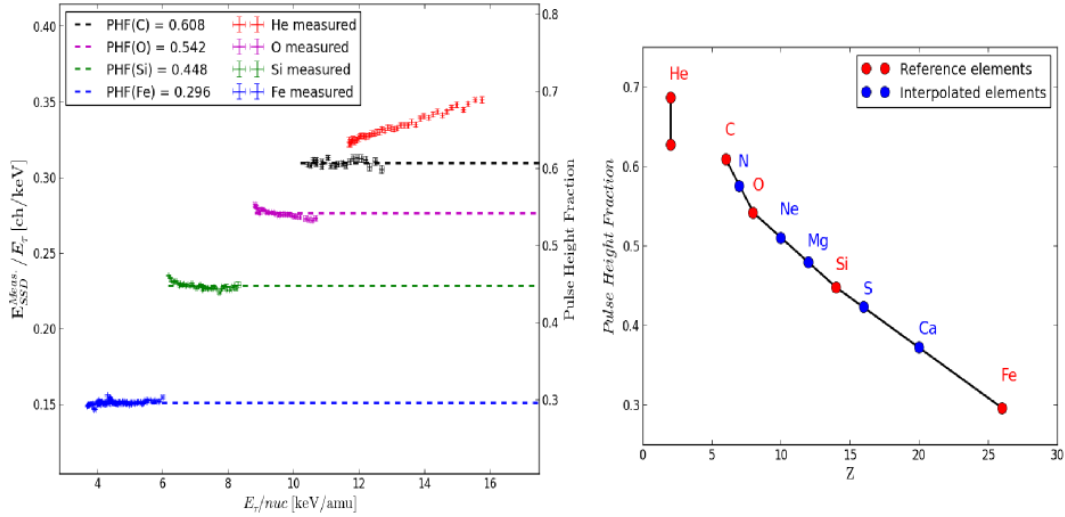


FIGURE 4.28: Left: Calculated PHFs for the reference elements and carbon after obtaining the calibration constants A and B from the helium fits for a dead-layer thickness of 75 nm. Right: Interpolation of the PHFs of further relevant solar wind elements: nitrogen, neon, magnesium, sulfur and calcium.

PHF can be converted via Eq. (4.12) back to the expected SSD energy channel which allows us to plot the calibrated ion positions into the ET-matrix. As discussed above, the ionic charge states of each element lie on the obtained elemental hyperbola as shown in figure 4.29, and 4.30 for energy-per-charge steps 56 and 78, respectively. From these figures we can see that with the purely interpolated PHFs of neon and magnesium we can precisely predict the energy position of their most prominent charge states  $\text{Ne}^{8+}$  and  $\text{Mg}^{10+}$ . Unfortunately it is hard to find evidence for the correct calibration of nitrogen and sulfur since their most prominent charge states lie in between the most prominent charge states of such more abundant elements as oxygen and carbon, and silicon and iron, respectively. Nevertheless the reproducibility of the  $\text{Ne}^{8+}$  and  $\text{Mg}^{10+}$  ToF and energy position is a good proof of the predictive power of the performed calibration.

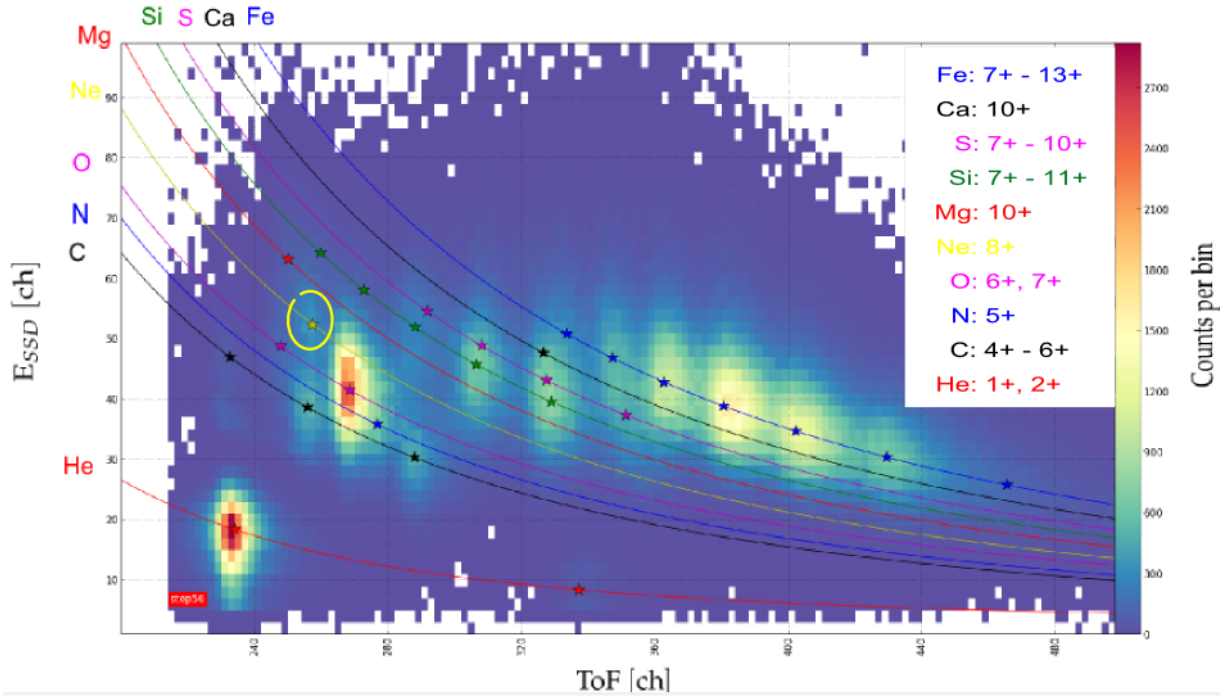


FIGURE 4.29: Calibrated ET-matrix at  $E/q^-$  (ESA) step 56. The yellow circle marks the interpolated position of  $\text{Ne}^{8+}$  which fits well to the actually observed peak.

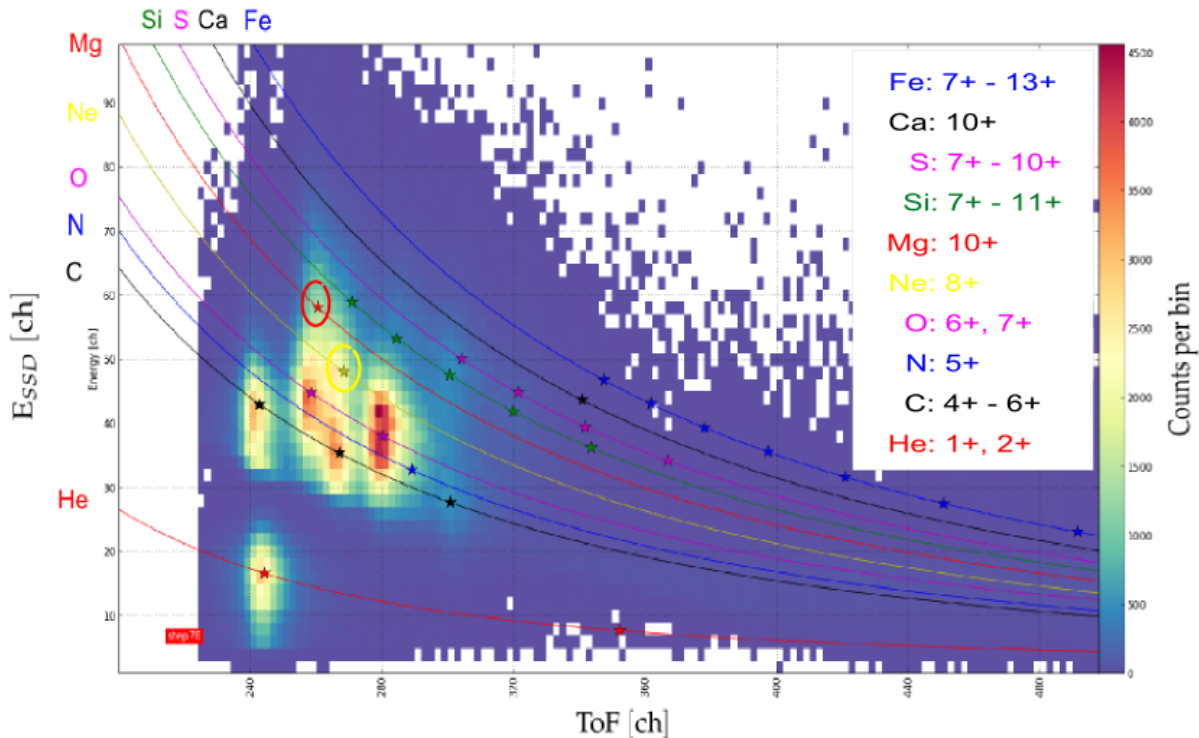


FIGURE 4.30: Calibrated ET-matrix at  $E/q^-$  (ESA) step 78. The yellow and red circles mark the interpolated position of  $\text{Ne}^{8+}$  and  $\text{Mg}^{10+}$ , respectively, which fit well to the actually observed peaks.

#### 4.2.5 Calibration of the Energy Peak Widths

As in the case of the ToF widths the TRIM results for the energy widths could not reproduce adequately the observed peak widths. However, when plotting the fitted signal width (or equivalently the standard deviation  $\sigma_{ESSD} = 1/[2.35 \cdot FWHM_{ESSD}]$ ) against the fitted most probable energy channel as done in figure 4.31, to a good accuracy one finds a simple linear relation between these quantities, which is

$$\sigma_E [ch] = 0.1024 \cdot E_{SSD} [ch] + 2.368 \text{ ch} \quad (4.27)$$

We mention that this approach was also already applied for the in-flight calibration of similar instruments such as ACE/SWICS (Berger, pc: 2014) and at least the positive sign of the slope can be understood since ions with higher initial energy undergo on average more collisions both with the target nuclei and electrons before they fully stop and therefore, their energy deposit distribution broadens absolutely similar to a random walk scenario.

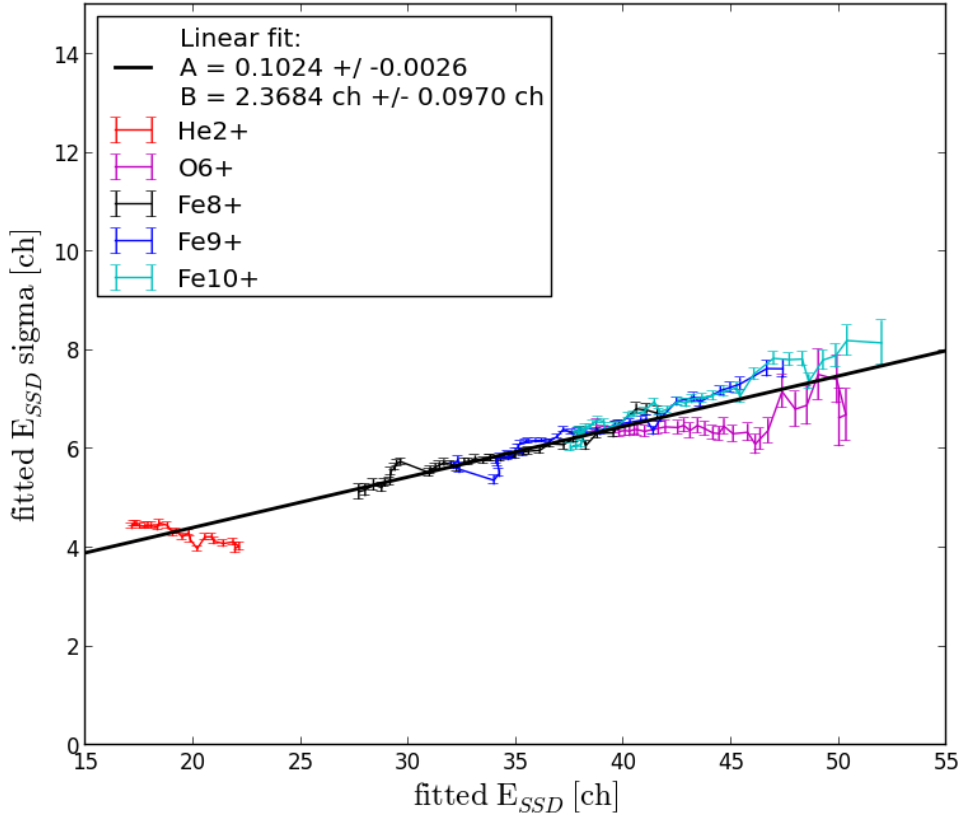


FIGURE 4.31:  $E_{SSD}$  signal sigmas.

### 4.3 An Improved Peak Shape Model for Iron Ions

While the 2D-Gaussian peak shape is a useful first approximation for the individual ion peak shapes, as can be seen from figure 4.32 (left panel) for the heavy iron ions there are significant deviations from this shape. This is especially important because the several iron charge states are comparable in abundance and therefore inaccurate peak shapes can easily lead to false assignment of the measured counts. While for a

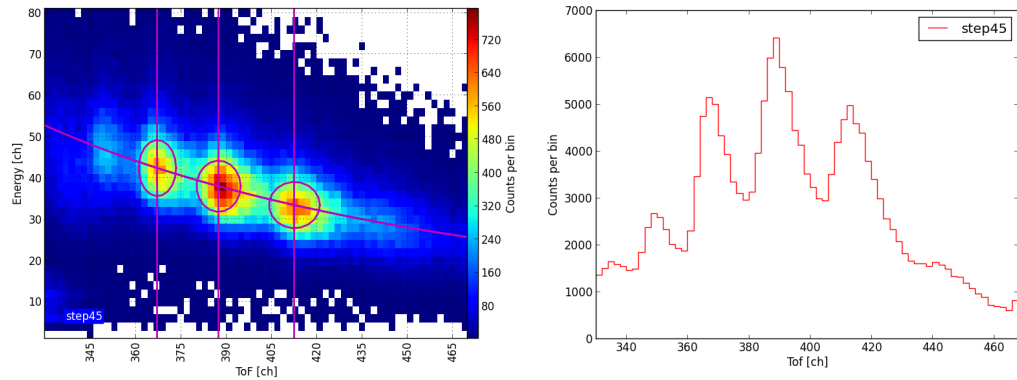


FIGURE 4.32: Left: Calibration for the iron ions  $\text{Fe}^{8+}$ ,  $\text{Fe}^{9+}$ ,  $\text{Fe}^{10+}$  (from right to left at ESA step 45) obtained from the 2D-Gaussian peak shape model. Right: ToF histogram of the same iron ions at the same ESA step.

fixed ToF-channel the energy signal of the shown charge states  $\text{Fe}^{8+}$ ,  $\text{Fe}^{9+}$  and  $\text{Fe}^{10+}$  is quite symmetrically centered around the most probable energy channel we observe a significant asymmetry in the ToF signal, which can be seen even better in the 1d ToF histogram in the right panel of figure 4.32 which is just the projection of the 2d-ET matrix on the ToF axis.

The observed tails at the high-ToF flank of the peaks are caused by the straggling in the carbon foil as mentioned before. The straggling itself is a very complicated process which again can be divided into electronic straggling describing the variation of energy loss to the target electrons and nuclear straggling describing the variation of energy loss to the target nuclei [39]. In thin layers like the CTOF carbon foil the electronic straggling can be calculated from Landau straggling theory [44] while the nuclear straggling is a rare process which has to be modeled with Poissonian statistics following

$$P_\lambda(k) = \frac{\lambda^k}{k!} e^{-\lambda} \quad (4.28)$$

where  $P_\lambda(k)$  is the probability that the particle undergoes  $k$  collisions and  $\lambda$  is the expected number of ion-target nuclei collisions and supposed to be very small. Both processes lead to skewed energy loss distributions with high-energy tails as we see them in

the energy loss spectra calculated by TRIM in figure (4.7). These high energy tails in the energy loss spectra are converted into low-energy tails in the residual energy spectra of the ion ensemble assuming a mono-energetic incident beam on the foil. The residual energy distributions naturally represent the variation in kinetic energy of the particles after the foil so that we can convert them into ToF spectra as exemplary shown in figure 4.33 (upper left) which then have the observed high-ToF tails.

The resulting ToF distributions can be fitted with a function which is a mix of a Gaus-

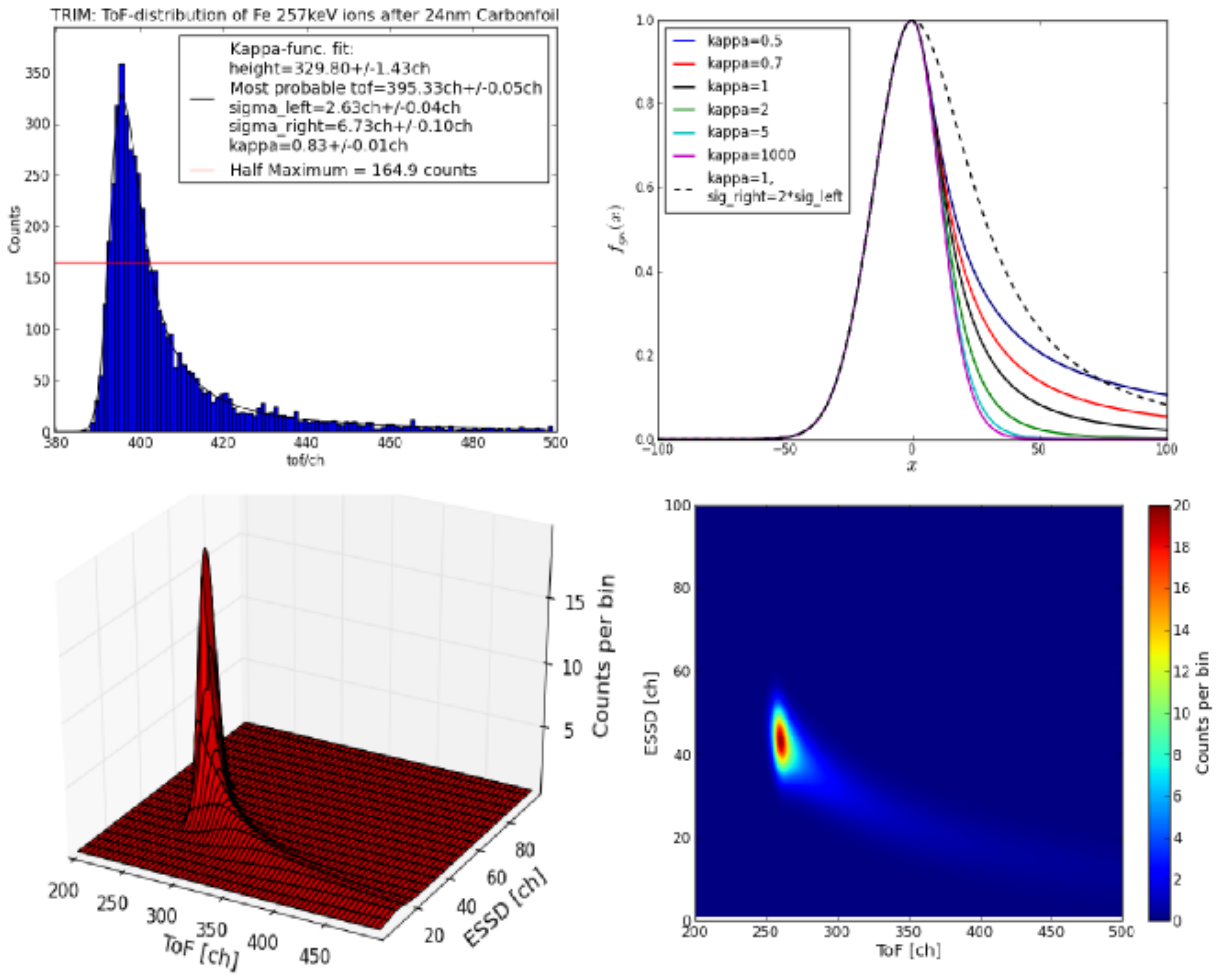


FIGURE 4.33: Gauss-Kappa functions (upper panels) and improved peak shape model  $f_{ips}$  (lower panels). The tail parameter in the lower panels is exaggerated to better illustrate the peak shape.

sian (at the low ToF flank) and a kappa-function (at the high ToF flank) and so we call it *Gauss-kappa function* and write  $f_{g\kappa}$ . This function, beside the height  $h$ , has four

parameters and is defined as:

$$f_{g\kappa}(T[T_0, \sigma_l, \sigma_r, \kappa]) = \begin{cases} h \cdot \exp\left(-\frac{(T - T_0)^2}{2\sigma_l^2}\right) & \text{if } T \leq T_0 \\ h \cdot \left(1 + \frac{(T - T_0)^2}{2\sigma_r^2 \cdot \kappa}\right)^{-\kappa} & \text{if } T \geq T_0 \end{cases} \quad (4.29)$$

with  $T_0$  as the most probable value of the ToF distribution,  $\sigma_l$  and  $\sigma_r$  as parameters for the different widths below and above  $T_0$  and  $\kappa$  as a parametrization of the tail. A Gauss-kappa function is already applied as fit in figure 4.33 in the upper left panel and sketched in the upper right panel of figure 4.33: We plotted the function for different values of  $\kappa$  but always with the same value of  $\sigma_l = \sigma_r = 15$  ch except for the black dotted curve where we set  $2 \cdot \sigma_l = \sigma_r$  which is closer to the real situation of the CTOF ToF measurements.

In order to fit the 2-dimensional distributions in the ET matrix we construct a 2-dimensional fit function by multiplying the Gauss-kappa function with a Gaussian of unity height:

$$f_{ug}(E, [E_0, \sigma_E]) = \exp\left(-\frac{(E - E_0)^2}{2\sigma_E^2}\right) \quad (4.30)$$

This is motivated by the fact that we did not observe a substantial asymmetry in the CTOF energy signals. The obtained function is then

$$f(T, E) = h \cdot f_{ug\kappa}(T) \cdot f_{ug}(E) \quad (4.31)$$

where we denoted the Gauss-kappa function of unity height as  $f_{ug\kappa}$ . Finally we consider the effect that the observed tails in figure 4.33 are not extending parallel to the ToF axis but instead follow the plotted hyperbola, representing the energy calibration for a certain element as given by Eq. (3.5). This can be explained by the fact that within an extended peak the ions at the low-ToF flank of the peak have more kinetic energy than the ions at the high-ToF flank and therefore on average the first deposit more energy in the SSD than the latter (and neither of them deposits the average energy  $E_0(T_0)$ ). We can include this in the peak shape model by writing the mean energy of the Gaussian as function of the free time-of-flight parameter  $T$ , rather than of its fixed most probable value  $T_0$ :

$$E_0(T) = A_0 \cdot \eta(T, Z) \cdot \frac{mL_\tau^2}{2} \cdot \left(\frac{T - b_{ToF}}{a_{ToF}}\right)^{-2} \quad (4.32)$$

where we used the relation between ToF channel and energy channel obtained in the position calibration (see Eq. (4.1) and (4.12)). Graphically this modification forces the peak (and especially its tail) to form a curve in the ET-plane following the elemental

hyperbola in figure 4.29. Putting all parts together and listing explicitly all fit parameters that define the actual peak shape and position in square brackets we find for the improved peak shape model the following form:

$$f_{ips}(T, E, [T_0, \sigma_l, \sigma_r, \kappa, \sigma_E]) = h \cdot f_{ug\kappa}(T, [T_0, \sigma_l, \sigma_r, \kappa]) \cdot f_{ug}(E, [E_0(T), \sigma_E]) \quad (4.33)$$

where  $T$  and  $E$  are free ToF and residual energy variables (given in channels) and  $h$  is the dependent variable which has to be fitted to the measured count rates. Visualizations of such a peak are shown in figure 4.33 in the lower panels as 3d-surface plot (left) and color plot (right).

#### 4.3.0.1 Parametrization of the Peak Width Parameters for Iron Ions

Like with the simple 2D-Gaussian model one also has to apply the improved fit model to the long-time data in order to fix all remaining free parameters except for the peak heights. Since the peak position is already fixed we only fit the width parameters  $\sigma_l, \sigma_r, \sigma_E$  to the long-time data. Since this is basically the same procedure as described in the first part of this chapter we do not explain the procedure in detail here. Instead we only mention that the  $\kappa$ -parameter turned out to be very sensitive even to small count rate fluctuations in the data. So we had to derive this value from a parameter study prior to the fits of the other parameters, in which we fixed the  $\kappa$ -value at several different values close to the value derived from TRIM and let all other width parameters free. Then we selected the  $\kappa$  value for which the deviations between data and model were lowest at a number of different steps. It turned out that at nearly all relevant ESA steps the value  $\kappa = 1.2$  matched best, for all investigated iron ions which indicates only a weak dependence of  $\kappa$  on the iron ion velocity in the given energy range. Having fixed that value we could parametrize the remaining ToF sigmas in dependence on the mean energy of the ions after the post-acceleration (or prior to the carbon foil)  $E_{acc}$ :

$$\sigma_l(E_{acc}) = -0.019 \text{ ch/keV} \cdot E_{acc}[\text{keV}] + 10.0 \text{ ch} \quad (4.34)$$

$$\sigma_r(E_{acc}) = -0.046 \text{ ch/keV} \cdot E_{acc}[\text{keV}] + 27.1 \text{ ch} \quad (4.35)$$

while  $\sigma_E$  was taken to be the same as in Eq. (4.27).

With all peak shape parameters fixed except for the height we could perform the following fits to the  $\text{Fe}^{7+}$  -  $\text{Fe}^{11+}$  peaks in the long-time data, shown in figure 4.34. We see that although we are fitting the five iron peaks at the same time with relatively sophisticated peak shapes these peaks do not expand on the cost of each other because

all parameters except for the heights are principally bound to the most probable ToF position via  $E_{acc}$ . This can be also motivated physically since the iron ions all have the same atomic number and lose their charge state information as soon as they reach the carbon foil. Therefore the only control parameter which influences both the energy loss and straggling in the carbon foil and SSD and therefore determines peak position and shape is the ion's velocity after the post-acceleration, which is bijectively related to its kinetic energy.

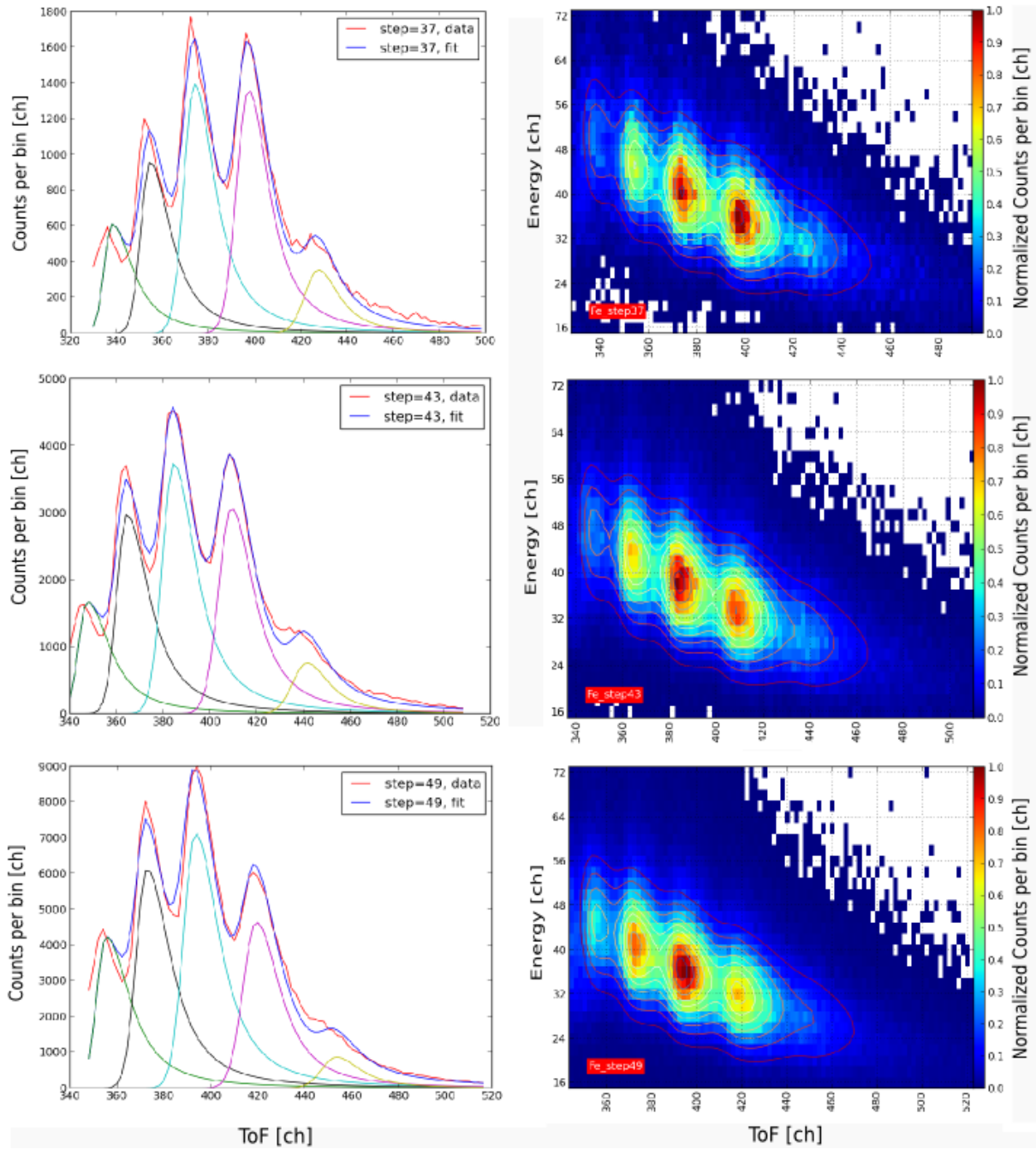


FIGURE 4.34: Improved peak shape model for the iron ions  $\text{Fe}^{7+}$  to  $\text{Fe}^{11+}$  (from right to left) fitted to long-time data at  $E/q$ -step 37, 43, 49.

# Chapter 5

## Data Analysis

### 5.1 Count Rate Analysis with Box Rates

In this chapter we describe the procedure of obtaining velocity spectra for a given ion species from the ET-matrix data. In principle this procedure is straight forward: We scan through all energy-per-charge steps of a given CTOF measurement cycle and simply sum over those counts in the ET-matrix which could be assigned to the selected ion distribution based on the performed in-flight calibration. In the easiest case the assignment is done by considering only the counts in the 1-sigma environment of the calculated most probable position as shown in figure 5.1 and 5.2 for the ion Fe<sup>9+</sup> for long- and short-time data, respectively.

The obtained energy-per-charge spectra can then be converted to velocity spectra since we know the mass and charge of the assigned ions so that we can convert each energy-per-charge step into a velocity by

$$v = \sqrt{\frac{2q}{m} \cdot \left(\frac{E}{q}\right)_j} \quad (5.1)$$

where  $\left(\frac{E}{q}\right)_j$  is the adjusted energy-per-charge value at a given ESA step  $j$  obtained from Eq. (3.1). An example of a measured energy-per-charge spectrum and the corresponding velocity spectrum is shown in figure 5.3.

Finally we have to consider that the velocity acceptance of the electrostatic analyzer, given in Eq. (3.6) is proportional to the ion velocity and therefore the instrument covers

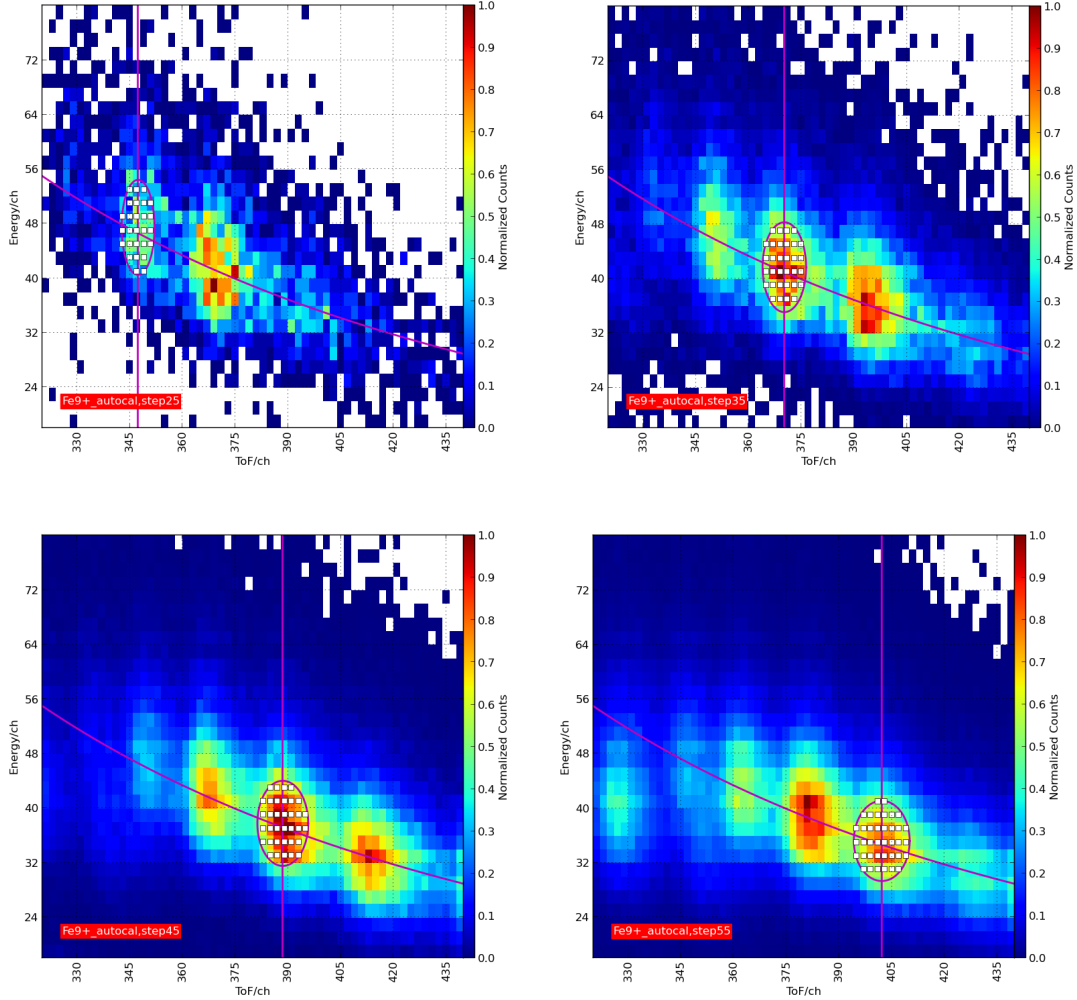


FIGURE 5.1: Applied box rate method to  $\text{Fe}^{9+}$  long-time data at ESA step 25, 35 (upper panels) and 45, 55 (lower panels).

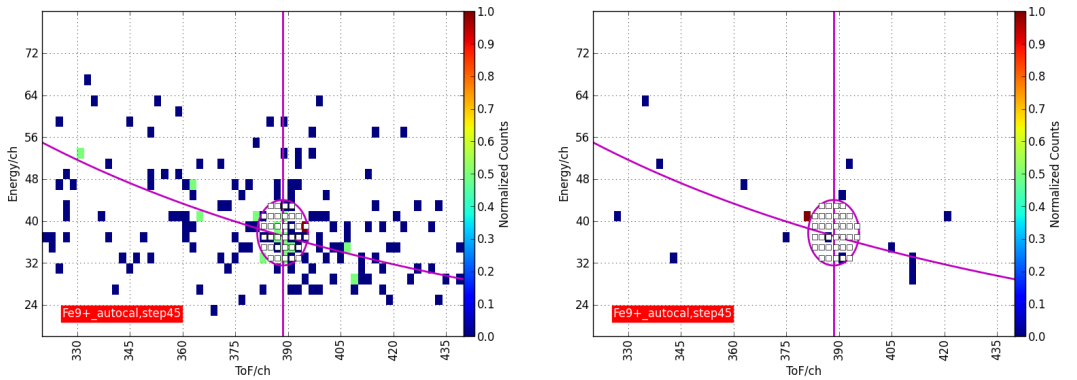


FIGURE 5.2: Applied box rate method to  $\text{Fe}^{9+}$  short-time data at ESA step 45 for 15-min (left) and 5-min (right) cadenced data.

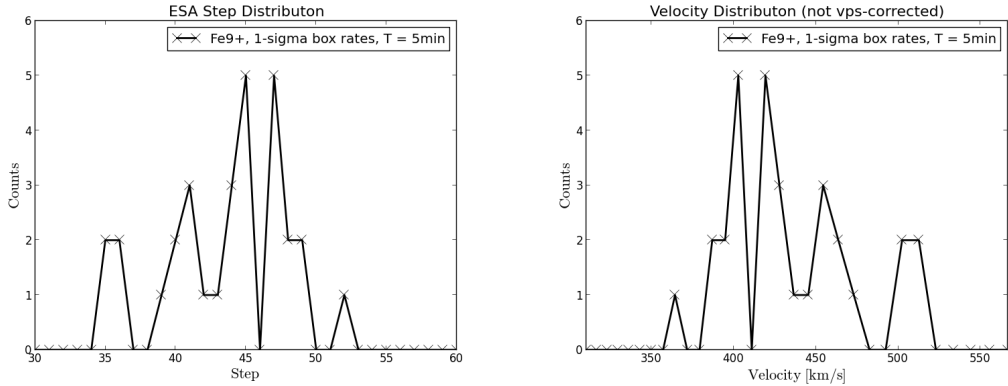


FIGURE 5.3: Examples of derived ESA-step (left) and velocity (right) spectra for  $\text{Fe}^{9+}$  5-min cadenced data.

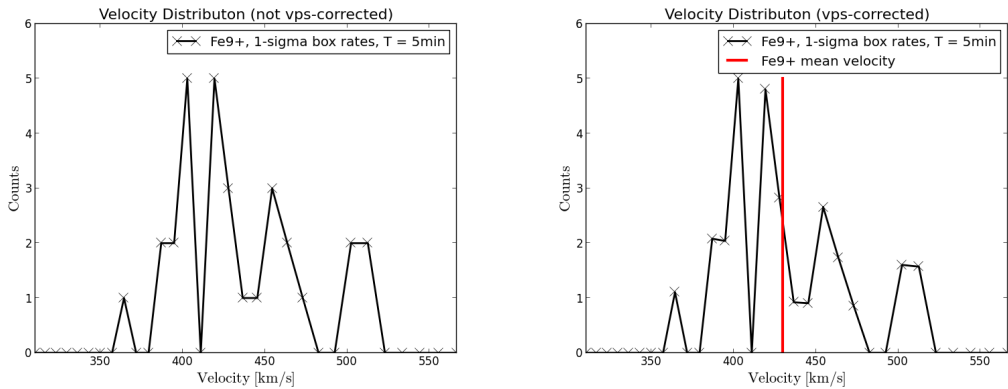


FIGURE 5.4: Examples of velocity phase-space corrected (right) and not corrected velocity spectra (left) for  $\text{Fe}^{9+}$  5-min cadenced data.

a larger fraction in the 1-dimensional velocity phase space for ions with higher incident velocities which are therefore over-represented in the velocity spectra. We can correct for this effect if we weight the obtained counts at each velocity  $v$  with a factor proportional to  $v^{-1}$ . We choose the concrete factor so that the maximum of the distribution is weighted with a factor of 1:

$$N(v)_{cor} = \frac{v_{max}}{v} \cdot N(v) \quad (5.2)$$

so that for velocities lower than  $v_{max}$  the count rate  $N(v)$  is raised, for those higher than  $v_{max}$  the count rate is lowered.

Note that this correction has only a small effect of about 10 km/s on the measured mean speed, derived as the first moment of the velocity spectrum, because the width of the spectrum is relatively narrow with an FWHM of about 10-15 steps. An example of a corrected and uncorrected spectrum is given in figure 5.4. However, it does play a role for the differential streaming which is on the order of 10% of the mean ion velocity. We mention that if we assume a Maxwellian velocity distribution the second moment of

the distribution  $\langle v^2 \rangle$  is related to the kinetic ion temperature via

$$T = \frac{2\langle E_{kin} \rangle}{3k_B} = \frac{m\langle v^2 \rangle}{3k_B} \quad (5.3)$$

where  $k_B$  is the Boltzmann constant. Therefore, we can also derive ion temperatures with CTOF if the statistics are sufficient.

In figure 5.5 we show typical examples for the spectra of  $\text{Fe}^{9+}$  accumulated over measurement periods of about 1 hour ( $\sim 12$  CTOF cycles), 15 minutes ( $\sim 3$  CTOF cycles) and 5 minutes ( $\sim 1$  CTOF cycle). We can see that even for the highest cadence of 5 minutes the statistics are in general good enough to obtain a reasonable mean ion velocity and even an estimation for the second moment could be done. Higher moments that are of interest in proofing the general assumptions of Maxwellian velocity distributions might be problematic to derive with 5 minute cadence, while this should not be a problem with 1 hour cadence which to our knowledge has not been done for iron ions yet. Taking into account the velocity spectra of the solar wind protons (red line in the lower panels of figure 5.5) measured at the same time with the CELIAS Proton Monitor (see upper left panel of figure 5.5), we can compare the mean proton velocity with the mean ion velocity and finally calculate the difference velocity

$$v_{diff} = v_{ion} - v_{proton} \quad (5.4)$$

which we define as the measured differential streaming within the investigated short-time period.

## 5.2 Count Rate Analysis with Poisson-Fits

The box rate analysis method has the disadvantage that it does not take into account the influence of adjacent ion peaks. As illustrated in figure 5.6 for the case of iron the 1-sigma environment of e. g.  $\text{Fe}^{9+}$  overlaps with the 3-sigma environment of  $\text{Fe}^{10+}$  so that even close to the calibrated  $\text{Fe}^{9+}$  position we have a non vanishing probability for measuring  $\text{Fe}^{10+}$  instead of  $\text{Fe}^{9+}$ . This plays especially a role in the case of asymmetric peak shapes with extended tails where the Gaussian relation between the sigma-value and the expected count rate fraction does not hold anymore. The errors also increase if one measures adjacent ions which differ significantly in average abundance and finally the static sigma-environments do not react to the count rate fluctuations in time: e. g. if within a certain CTOF cycle  $\text{Fe}^{10+}$  is strongly enriched compared to  $\text{Fe}^{9+}$ , which can

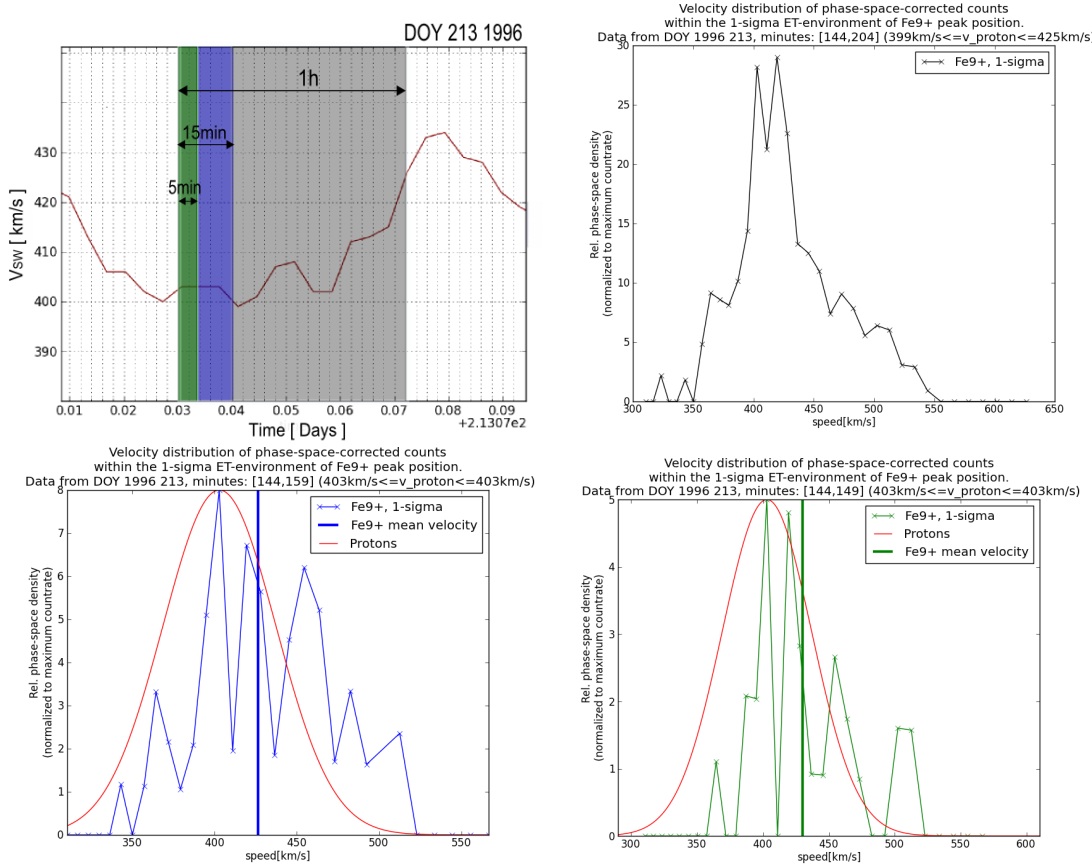


FIGURE 5.5: Upper left: Measured mean solar wind proton velocity from the CELIAS proton monitor (PM). Upper right and lower panels: Derived velocity spectra for 1-h (black), 15-min (blue) and 5-min (green) cadenced data. The red line in the lower panels represents the proton velocity distribution as given by the measured proton mean and thermal velocity measured by the PM..

be the case at stream interfaces. Finally even in the simple 2D-Gaussian model one can increase the statistics when the analysis method is not restricted to the 1-sigma environment of each ion. Therefore, we apply an improved analysis method by fitting the short-time data with the appropriate fit-functions derived from the calibration long-time data fits. The improved fit function  $f_{ips}$  derived in the previous section in (4.33) fully determines the peak shape of the iron ions so that all peak parameters are fixed except for the peak heights. Thus for each fitted peak the obtained height  $h_i$  is proportional to the volume  $V_i$  below the peak which is equal to the ion count rate  $N_i$ . Thus we can derive the count rates of the iron ions  $Fe^{7+}$  -  $Fe^{11+}$  directly from applying the following fit function directly to the short-time data:

$$f_{fit} = \sum_i^5 f_{ips,i}(T, E, h_i) \quad (5.5)$$

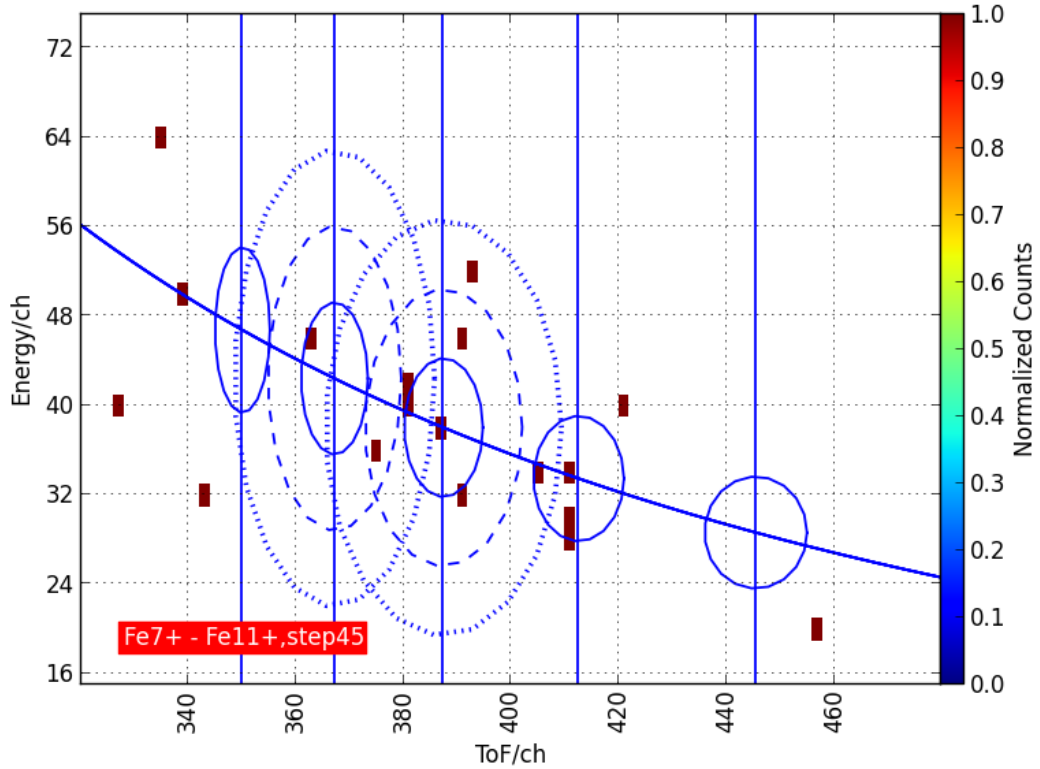


FIGURE 5.6: Calibrated positions of the iron ions  $\text{Fe}^{7+}$  -  $\text{Fe}^{11+}$  (from right to left) at ESA step 45 and 1-sigma (solid lines), 2-sigma (dashed lines) and 3-sigma (dotted lines) environments of  $\text{Fe}^{9+}$  and  $\text{Fe}^{10+}$  derived from the simple 2D-Gaussian fit model.

In order to have the counts of several sigma-environments of the included iron peaks in the fit but not the adjacent silicon peaks we limited the fit-area in ToF by

$$T_{min} = T_0(\text{Fe}^{11+}, s) - 1 \cdot \sigma_l(s) \quad (5.6)$$

and

$$T_{max} = T_0(\text{Fe}^{7+}, s) + 2 \cdot \sigma_l(s) \quad (5.7)$$

where  $T_0(\text{Fe}^{11+}, s)$  and  $T_0(\text{Fe}^{7+}, s)$  are the calibrated positions of the outer iron peaks at given ESA step  $s$  and  $\sigma_{l,r}(s)$  are the calibrated ToF-sigma values of the improved peak shape model. Similarly the area is limited in residual energy by

$$E_{min} = E_0(\text{Fe}^{7+}, s) - 2 \cdot \sigma_E(s) \quad (5.8)$$

and

$$E_{max} = E_0(\text{Fe}^{11+}, s) + 2 \cdot \sigma_E(s) \quad (5.9)$$

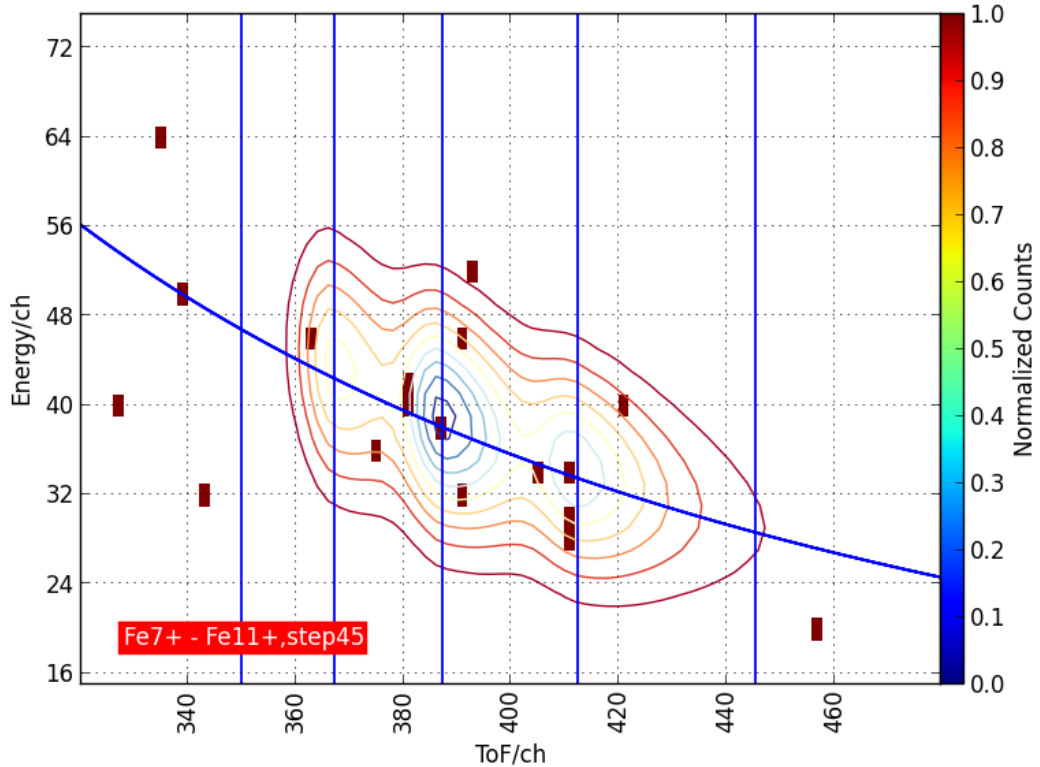


FIGURE 5.7: Example of a Poisson-fit applied to the iron ions  $\text{Fe}^{7+}$  -  $\text{Fe}^{11+}$  5-minute cadenced data at ESA step 45. The contour lines follow the superposition of the single ion peak shapes given by the improved peak shape model  $f_{ips}$ . Note that the peaks of  $\text{Fe}^{7+}$  and  $\text{Fe}^{11+}$  are not visible in this contour plot, because their fitted count rates lie below the threshold of the lowest contour line.

An example of such a fit applied to 5-minute cadenced data is shown in figure 5.7. In a second step the 5 obtained peak heights  $h_i$  are separately put into their respective single peak shape function  $f_{ips,i}$  to calculate the count rate as the volume below the curve which is in the case of the discrete ET-matrix a simple sum:

$$N_i = V_i = \sum_{T_j, E_k} f_{ips,i}(T_j, E_k, h_i) \quad (5.10)$$

where  $T_j, E_k$  are ET-matrix bins.

As a last point we address a decisive difference between long-time data fits that we applied in the previous chapter and the short-time data fits which we apply in this section. For the long-time data we could use a Gaussian minimization function given as

$$\chi_G^2 = \sum_i^N \frac{(f(x_i) - n_i)^2}{\sigma_i^2} \quad (5.11)$$

where  $f(x_i)$  represents the fit model,  $n_i$  are the measurements (in our case the number of counts per bin) and  $\sigma_i$  are the standard errors of the individual measurements which in the limit of high count rates can be considered as symmetrically distributed around  $n$  with  $\sigma_i \approx \sqrt{n_i}$ .

However, as can be seen in figure 5.7 we now deal with single counts per bin for which the errors are instead distributed after the Poisson distribution defined in Eq. (4.28). Therefore, we have to apply a minimization function  $\chi_P^2$  which is derived from Poisson statistics just as the following very fast converging function derived in a paper by [45] and which is defined as:

$$\chi_P^2 = \sum_i^N \left[ 2(f(x_i) - n_i) + (2n_i + 1) \cdot \log \left( \frac{2n_i + 1}{2f(x_i) + 1} \right) \right] \quad (5.12)$$

where the characteristic feature arising from Poisson statistics is the additional logarithmic term and, as the Poisson distribution itself,  $\chi_P^2$  is completely parametrized by the measured count rate value  $n_i$  rather than by a tuple  $(n_i, \sigma_i)$ . Furthermore we see that in the case of high count rates  $n_i, f_i \rightarrow \infty$ ,  $\chi_P^2$  behaves asymptotically like  $\chi_G^2$  because the second term in Eq. (5.12) approaches  $\log(1) = 0$  and the denominator  $\sigma^2 \approx n_i$  in Eq. (5.11) cancels with  $(f(x_i) - n_i)$  in the numerator. Finally the authors could show by comparison with Monte-Carlo simulations that the given  $\chi_P^2$  is performing very well in the special case of asymmetric distributions with significant tails such as the Moyal function which is often used as approximation for the Landau distribution and therefore is exactly what we need and what we consequently implemented in the fit algorithm for the short-time data.

# Chapter 6

## Results

### 6.1 Differential Streaming of Heavy Ions Derived from Box Rates

Here we present the results for the differential streaming of  $O^{6+}$ ,  $Si^{7+}$ ,  $Fe^{9+}$  and  $Fe^{10+}$  obtained from 1-sigma box rates as described in section (5.1). These ions were selected because the first three of them were also investigated in the earlier CTOF study by [32] so that we can compare our results. Furthermore we want to compare the behavior of the most abundant ion charge states  $Fe^{9+}$  and  $Fe^{10+}$ . The investigated time period is DOY 150-220 1996 representing the second (and last) extended CTOF measurement period as described in section (3.2). In figure 6.1 we plotted the obtained mean ion velocity together with the mean proton velocity taken from the CELIAS Proton Monitor. The total number of measurements in this 70-days time period is larger than  $2 \cdot 10^4$  since the time difference between two measurements is the inherent CTOF ESA cycle time of about 5 minutes. However, note that the actual time interval over which the obtained mean ion velocities are averaged is about 1 minute only, because due to the finite ion temperatures the non-zero count rates are distributed just over  $\sim 20$  of the 117 measurement cycle steps as exemplary shown in figure 5.3.

The time series show that in general we observe ion velocities greater than the corresponding proton velocities in the fast solar wind above proton velocities of  $\sim 400$  km/s. For  $O^{6+}$  and  $Si^{7+}$  this effect is stronger than for the iron ions. We also see that the fluctuations of the mean ion velocity are larger in the fast solar wind, which cannot be explained only by the lower density of the fast wind. Instead this partly results from telemetry budget variations lowering the obtained CTOF count rate in the fast wind (M. Hilchenbach, pc: 2014) and partly from the ambient B-field directional change, which

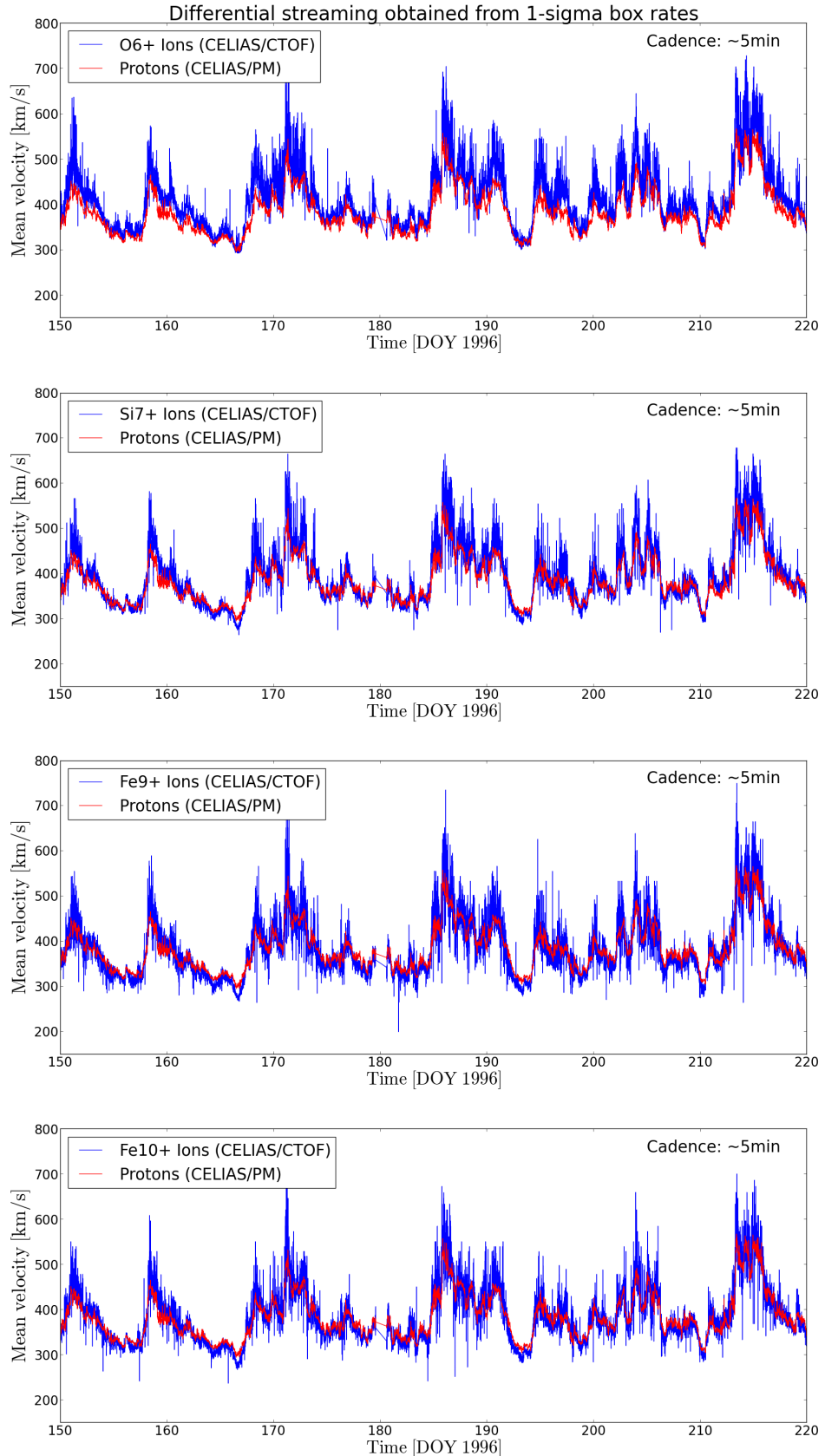


FIGURE 6.1: Time series of the measured mean ion velocities (blue) and the mean proton velocity (red) over the full investigation period of this study DOY 150-220 1996 for O<sub>6+</sub>, Si<sub>7+</sub>, Fe<sub>9+</sub> and Fe<sub>10+</sub> (from top to bottom). The mean ion velocities were obtained from the 1-sigma box rates method described in chapter 5 .

is seen stronger in the fast wind where a significant differential streaming is produced. To derive quantitative statements for the differential streaming of heavy ions we created 2d-histograms with proton and ion velocity representing the x- and y-axes. These

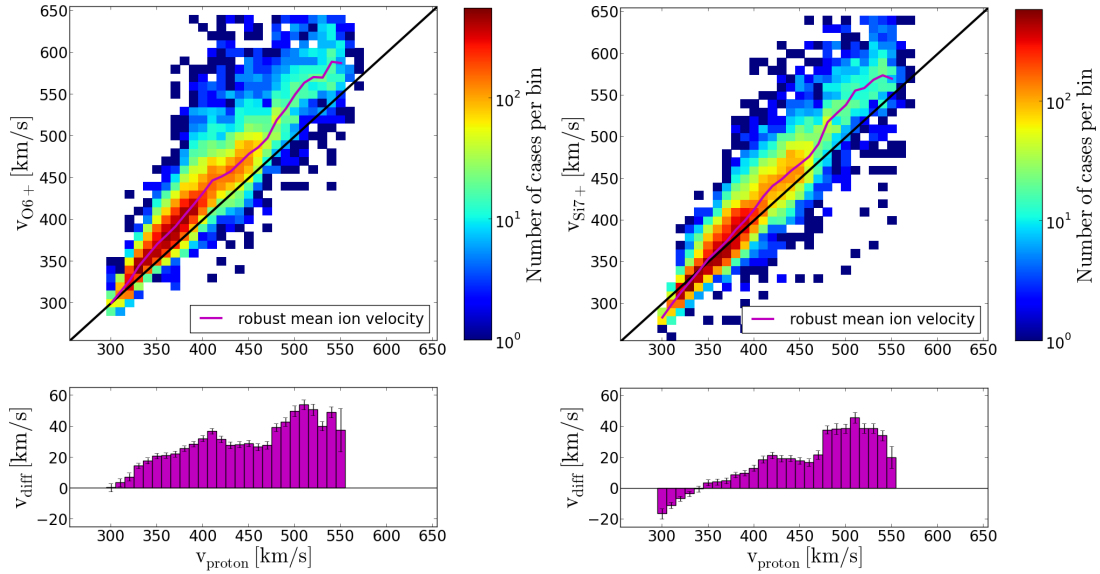


FIGURE 6.2: Upper panels: 2D-histograms of the obtained mean ion and proton velocities for  $O^{6+}$  and  $Si^{7+}$  measured during the same CTOF cycle and obtained from the 1-sigma box rates method. The magenta curve signifies the robust mean ion velocity at a given proton velocity. The difference between the mean ion velocity and the identity (black) is the resulting differential streaming, plotted in the bottom panel.

are shown in figure 6.2 and 6.3. The robust mean ion velocity at each fixed proton velocity is calculated only from those bins in which we have at least 10 counts to avoid effects of statistical outliers. For all investigated ions the differential streaming

$$v_{diff} = \bar{v}_{ion} - v_{proton} \quad (6.1)$$

shows a clear dependency on the proton velocity with the general trend to increase with higher proton velocities. For  $O^{6+}$  we obtain velocity differences of  $\sim 50$  km/s for the fastest proton velocities above 500 km/s while the difference vanishes completely for the very slow solar wind at 300 km/s. For  $Si^{7+}$  we obtain a maximum differential streaming of  $\sim 40$  km/s in the fast solar wind while interestingly we find negative differential streaming for very slow solar wind below 340 km/s. Both for  $Fe^{9+}$  and  $Fe^{10+}$  the obtained maximum differential streaming is only  $\sim 20$  km/s while for these ions we observe negative speed differences for the whole slow solar wind regime below 400 km/s. The minimum differential streaming of  $-20$  km/s, obtained at the lowest proton velocity of 300 km/s, is the same as for  $Si^{7+}$ . For all ions one can recognize

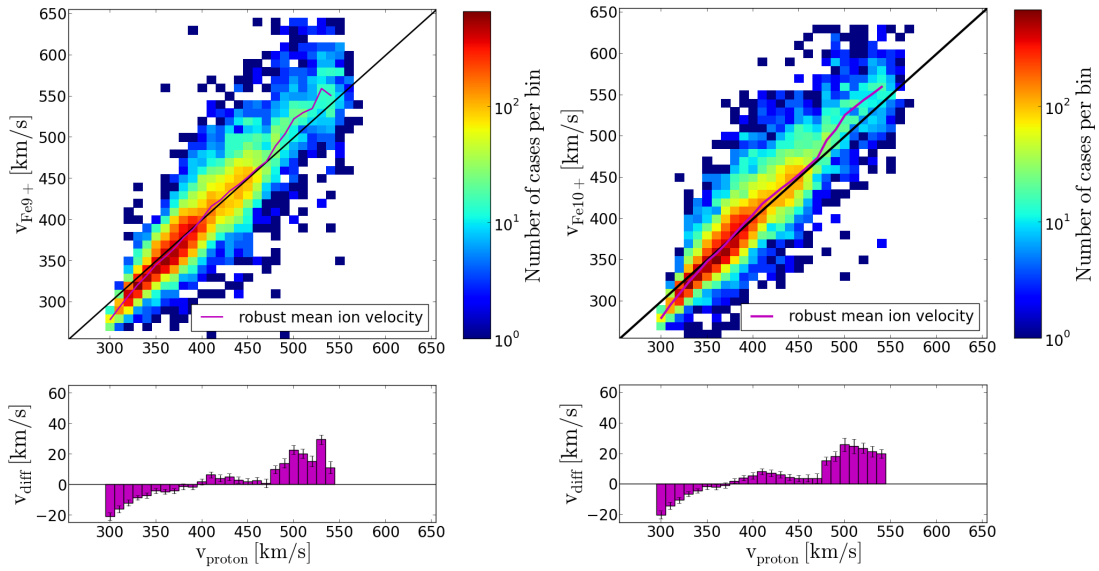


FIGURE 6.3: Upper panels: 2D-histograms of the obtained mean ion and proton velocities for  $Fe^{9+}$  and  $Fe^{10+}$  measured during the same CTOF cycle and obtained from the 1-sigma box rates method. The magenta curve signifies the robust mean ion velocity at a given proton velocity. The difference between the mean ion velocity and the identity (black) is the resulting differential streaming, plotted in the bottom panel.

a small dip of  $\Delta v_{diff} \approx -10$  km/s against the general trend of increasing differential velocities around proton velocities of  $\sim 450$  km. Note that the obtained uncertainties for the differential streaming which are visualized as error bars in the speed difference plots simply represent the standard error of the mean ion velocity calculated from all  $N$  ion velocities which were taken into account for the calculation of the robust mean at each proton velocity:

$$\Delta \bar{v}_{ion} = \sqrt{\frac{\sum_{i=1}^N (v_i - \bar{v}_{ion})^2}{N(N-1)}} \quad (6.2)$$

Therefore, these uncertainties consider only the statistical effect of the width of the measured ion velocity distributions both due to the non-zero temperature of the ion velocity spectra in the solar wind and the fluctuation of the B-field relative to our measurement direction (see figure 1.7). This implicates that we assume the proton monitor to measure with negligible uncertainty, which is reasonable, since such measurements can be done with high precision due to the much higher statistics of solar wind protons compared to heavy ions. More important, systematic errors e.g. due to systematic shifts of positions and inaccurate peak shapes in the ET-matrix calibration or false ion assignment due to the static box rate counting method in the data analysis are not yet included in this uncertainty estimation.

To summarize, besides the theoretically expected significant differential streaming in the fast solar wind we make two observations that are difficult to explain: First the

small dip around  $v_{proton}=450$  km/s and second negative differential streaming in the very slow solar wind.

## 6.2 Differential Streaming of Iron Ions Derived from Poisson-Fits

In this section we present the results for the differential streaming of the iron ions  $\text{Fe}^{8+}$ ,  $\text{Fe}^{9+}$  and  $\text{Fe}^{10+}$  obtained from the Poisson-fitting method described in section 5.2, in which also the improved peak shape model for iron ions, derived in section 4.3, is integrated. The ions on the low- and high-ToF flanks of the fitted sequence  $\text{Fe}^{7+}$  and  $\text{Fe}^{11+}$  are not discussed here since  $\text{Fe}^{11+}$  itself lies in the tail of  $\text{Fe}^{12+}$  while it turned out that  $\text{Fe}^{7+}$  already lies largely in the ToF pile-up tail of  $\text{He}^{2+}$  ranging up to energy channel 30 at low energy-per-charge steps. The obtained time series of  $\text{Fe}^{8+}$ ,  $\text{Fe}^{9+}$  and  $\text{Fe}^{10+}$  are shown in figure 6.4. Compared to the iron time series in figure 6.1 the fluctuations of the mean ion velocities derived from the fits are strongly suppressed by the improved analysis method. Furthermore we now find clear evidence for significant differential streaming in the fast solar wind regime similar to the one found for  $\text{O}^{6+}$  and  $\text{Si}^{7+}$  in the previous section. This can be quantified again from the histograms in figure 6.5: For all three investigated iron ions we find positive differential streaming for proton velocities above 350 km/s which is rising up to more than 40 km/s for  $\text{Fe}^{9+}$  and  $\text{Fe}^{10+}$  and to just about 40 km/s for  $\text{Fe}^{8+}$  at the highest proton velocities around 500 km/s. Comparing these values to the results obtained for  $\text{Fe}^{9+}$  and  $\text{Fe}^{10+}$  with the 1-sigma box rate analysis method in figure 6.3 we find an average difference of  $\sim 10$  km/s for the measured differential streaming at proton velocities between 350 and 450 km/s and a difference of  $\sim 20$  km/s at proton velocities above 450 km/s. At very low proton speeds, however, we roughly still find the same negative differential streaming of about  $-20$  km/s. These results show that the improvements in the applied analysis method change the obtained results for the differential streaming of  $\text{Fe}^{9+}$  and  $\text{Fe}^{10+}$  by a factor of 100% for proton speeds above 400 km/s. This is possible because the measured velocity differences are in general on the order of only 10% of the solar wind ion velocities and therefore represent a small effect. In particular the step-width of the energy-per-charge analyzer corresponds to  $\sim 7$  km/s at an ion velocity of 350 km/s and to  $\sim 12$  km/s at an ion velocity of 600 km/s, so that the observed changes when switching the analysis method correspond to a shift of less than 2 steps in the maximum of the measured counts-per-step spectra. The significant change in the observed speed difference can be understood with the scheme in figure 6.6: We assume the two iron ions  $\text{Fe}^{9+}$  (marked blue) and  $\text{Fe}^{10+}$  (marked cyan) to have the same solar wind speed of  $\sim 400$  km/s. Therefore,  $\text{Fe}^{9+}$ , which might be slightly less in abundance compared to  $\text{Fe}^{10+}$  peaks at ESA step 47 while  $\text{Fe}^{10+}$  peaks at step 50. Furthermore both peaks show high Tof

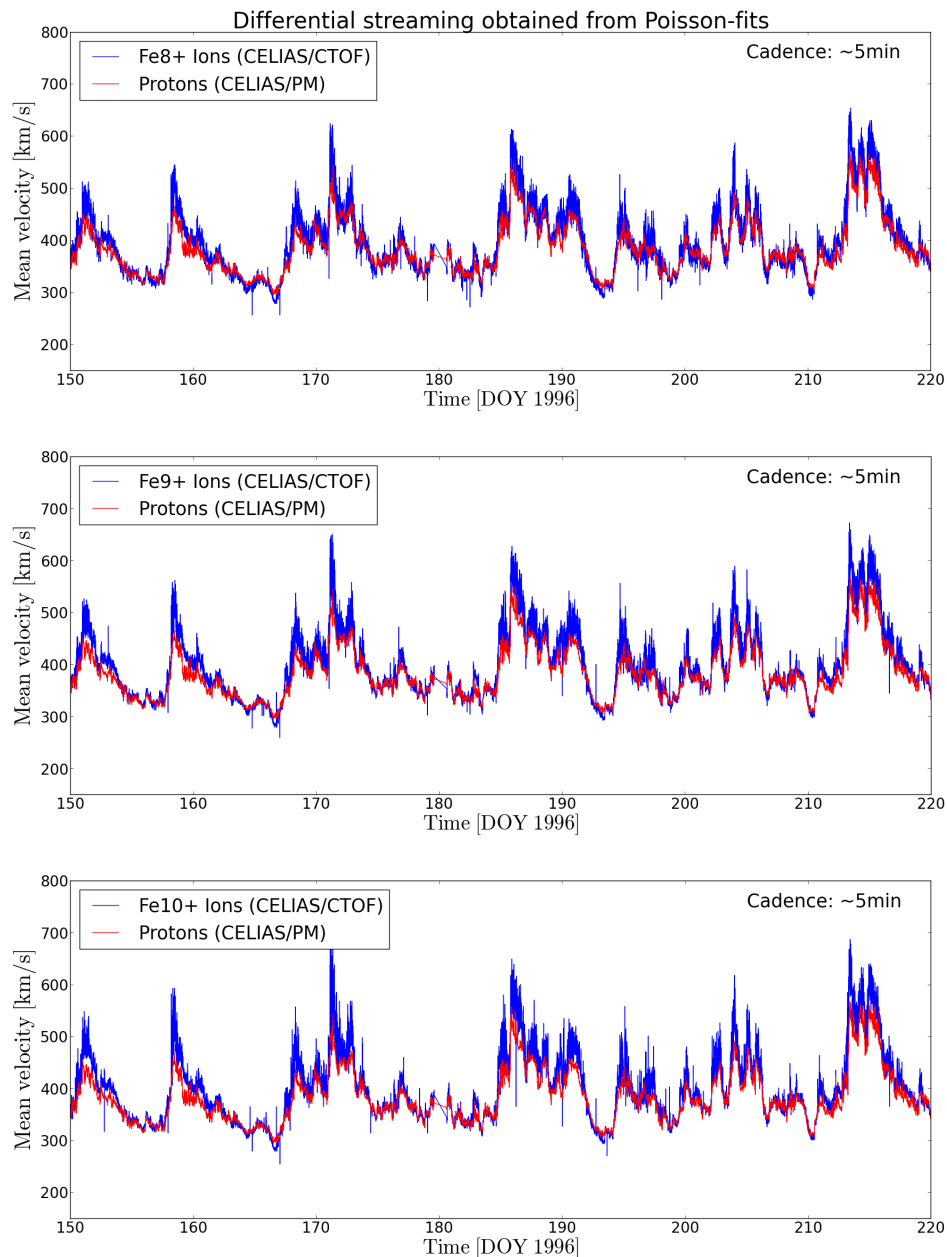


FIGURE 6.4: Time series of the measured mean ion velocities (blue) and the mean proton velocity (red) over the full investigation period of this study DOY 150-220 1996 for  $\text{Fe}^{8+}$ ,  $\text{Fe}^{9+}$  and  $\text{Fe}^{10+}$  (from top to bottom). The mean ion velocities were obtained from the Poisson-fit method described in chapter 5 .

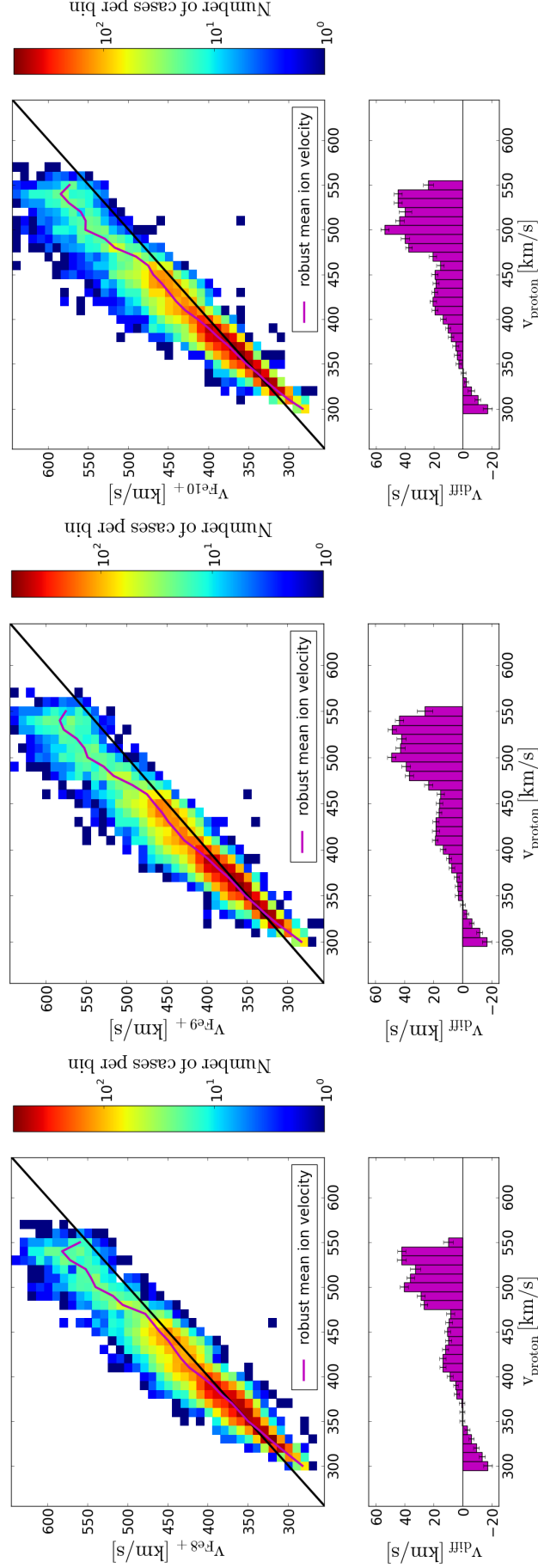


FIGURE 6.5: Upper panels: 2D-histograms of the obtained mean ion and proton velocities for  $Fe^{8+}$ ,  $Fe^{9+}$  and  $Fe^{10+}$  measured during the same CTOF cycle and obtained from the Poisson-fit method. The magenta curve signifies the robust mean ion velocity at a given proton velocity. The difference between the mean ion velocity and the identity (black) is the resulting differential streaming, plotted in the bottom panel.

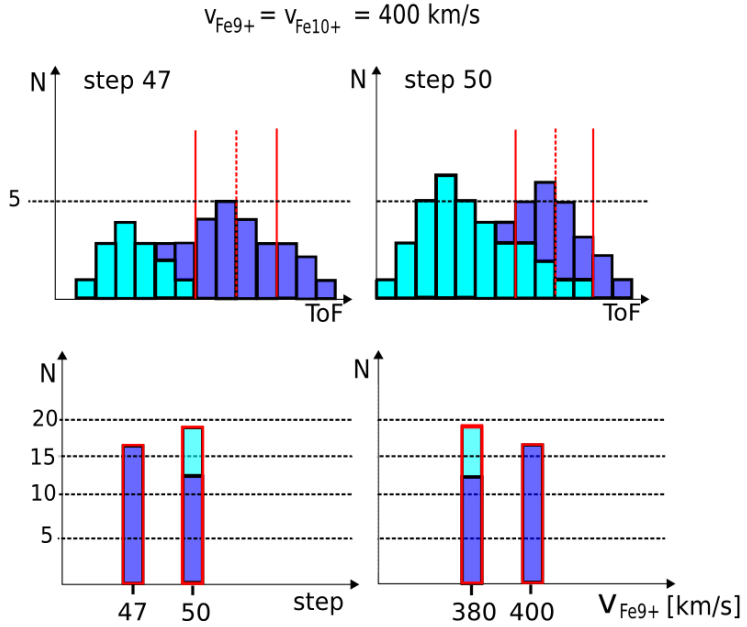


FIGURE 6.6: Schematic illustration of the difference between the box rate method and the Poisson-fit method. For details, see the corresponding passage in the text.

tails with the  $\text{Fe}^{10+}$  tail extending into the  $\text{Fe}^{9+}$  peak. When we now simply count the measured counts within the red surrounding of  $\text{Fe}^{9+}$  in order to obtain a velocity spectrum shown below, we falsely obtain a higher count rate of  $\text{Fe}^{9+}$  at 380 km/s instead of 400 km/s. Thus the mean of the velocity distribution can be shifted by a small amount, which however is large in terms of the differential streaming. Even if the scheme might be slightly exaggerated and the situation is likely to apply only for peaks at the flank of even more abundant peaks, the situation accounts qualitatively at least for  $\text{Fe}^{8+}$  and  $\text{Fe}^{9+}$  since the mean iron charge state in the investigated measurement period in by far most cases lies in between  $\text{Fe}^{10+}$  and  $\text{Fe}^{9+}$  and closest to  $\text{Fe}^{10+}$ .

This point shows that an accurate calibration is necessary to get reliable results for the differential streaming. Therefore, for a conclusive result one also has to include the uncertainty of the calibration into the total uncertainty of the differential streaming. However, this is not done yet because the propagation of the estimated uncertainties in peak position and peak width (given in chapter 4) to the count rate spectra is not straight forward, in particular not for asymmetric peak shapes and Poissonian count statistics. In principle such an uncertainty estimation can be conducted numerically by a Monte-Carlo bootstrap method in which the obtained calibration parameters are fluctuated artificially within their estimated uncertainties while the resulting variation in count rate at each energy-per-charge step is recorded. Such a procedure is planned for the future, also in order to see whether the obtained negative differential streaming

at very low proton velocities is a real effect. We finally point out that there are additional critical error sources in the performed measurements, in particular the unknown uncertainties in the entrance system high-voltage power supply which determines the energy-per-charge value of the incident ions after Eq. (3.1). However, for comparing the obtained results with those of Hefti et al. [32] in the next chapter we do not need to take this into account since we used the exact values that Hefti gave in [34].

## Chapter 7

# Discussion and Conclusions

We finally want to compare our results to the results obtained by S. Hefti in [32] since these were also measured with the CELIAS/CTOF sensor aboard SOHO during Carrington rotations 1908-1912 starting on DOY 99 1996 and ending with the failure of the sensor on DOY 230 1996. The measurement period of this work is DOY 150 - 220 1996 and is therefore completely covered by the former study. Figure 7.1 shows the differential streaming obtained in this work together with the differential streaming obtained by Hefti represented by the gray straight line in the histogram, which is taken from the linear fits in the original paper plot already shown in figure (1.8) of chapter (1). We compare the data of  $O^{6+}$ ,  $Si^{7+}$  and  $Fe^{9+}$ . For the differential streaming of  $O^{6+}$  we see a difference of about 20 km/s between the different measurements at all proton velocities. Therefore, we find a differential streaming of 50 km/s for the fast wind around 500 km/s proton velocity which is almost twice as high as found by Hefti and that we do not find negative differential streaming for  $O^{6+}$ , not even in the very slow solar wind at a proton velocity of 300 km/s. For  $Si^{7+}$  we obtain a slightly larger negative differential streaming in the slowest wind at 300 km/s, however then the difference between the measurements is strongly increasing with increasing proton velocities so that in the fast wind we obtain a differential streaming of  $\sim 40$  km/s while Hefti measured negative values up to proton velocities around 500 km/s and ended up at no differential streaming at 550 km/s proton velocity. For  $Fe^{9+}$  the picture is almost the same as for  $Si^{7+}$  except for the fact that Hefti measured a slight negative differential streaming even for the very fast wind, which leads to a maximum difference between the two measurements of more than 40 km/s at proton velocities around 500 km/s. To conclude we find significant differences between the results found by Hefti and the results of this work. Due to the small size of the physical effect this is not unlikely if the

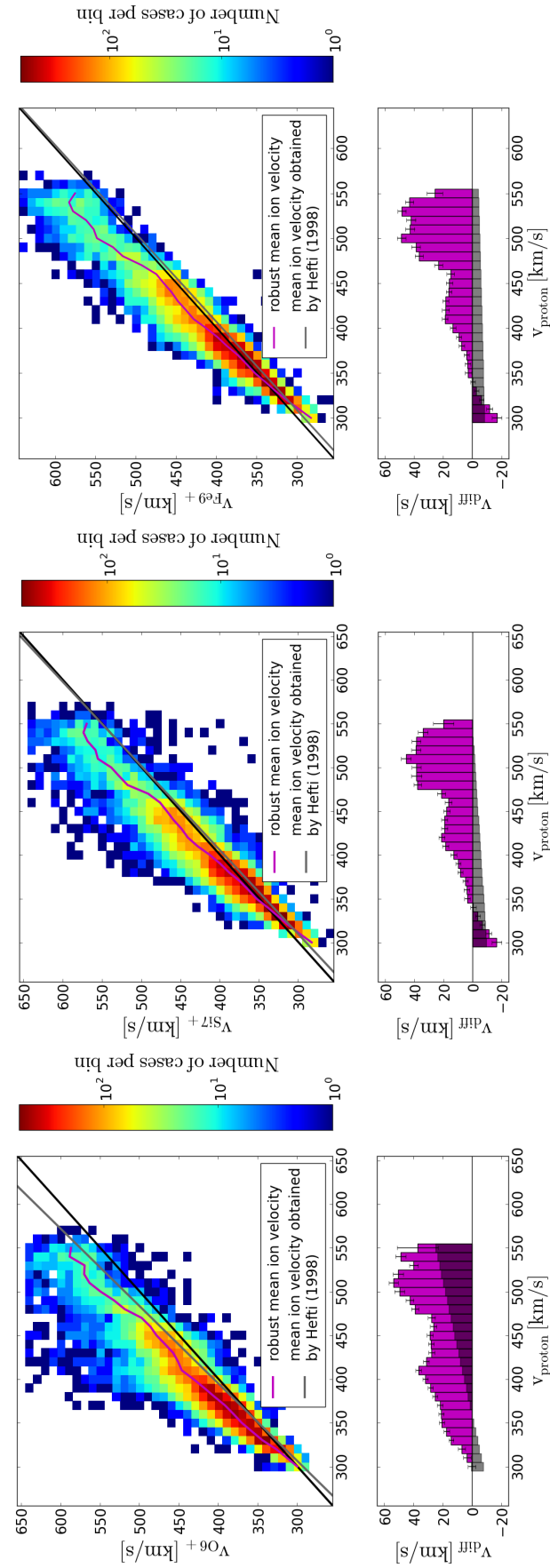


FIGURE 7.1: Comparison between the differential streaming obtained in this work (magenta) and the differential streaming measured by S. Hefti (1998) (gray) for  $O^{6+}$ ,  $Si^{7+}$  and  $Fe^{9+}$ .

calibrations and the data analysis methods differ in accuracy. As shown in the previous chapter for the iron ions, even if the position calibration is fixed, only the change of the peak shape together with a change from box rate counting to Poisson-fits increased the measured differential streaming of about 20 km/s which is already 50% of the obtained difference between the earlier findings of Hefti, directly derived from on-board processed data, and ours derived from raw PHA words.

In general there are few studies for the differential streaming of solar wind heavy ions conducted in the past. Beside the discussed one conducted by Hefti et al. we would like to compare our results with the studies of Berger et al. (2011) [31] and Ipavich et al. (1986) [46] who both measured the differential streaming of heavy ions at solar minimum conditions in the vicinity of L1 with ACE/SWICS and ISEE-3/ULECA, respectively. Berger et al. measured 44 charge states of the most abundant solar wind elements from helium up to iron at proton velocities between 400 km/s and 750 km/s for two high-speed streams over the time periods DOY 6-12 2008 and DOY 14-20 2008. The measurement cadence was  $\sim 12$  minutes and the measured projected velocity difference is corrected for the orientation of the ambient interplanetary B-field direction. In figure 7.2 the resulting velocity difference  $|v_{ip}|$  is compared to the local Alfvén speed, denoted as  $C_A$ , where we can see that all investigated ions show a differential streaming between 20% and 80% of the Alfvén speed. Ipavich et al. measured the speed of

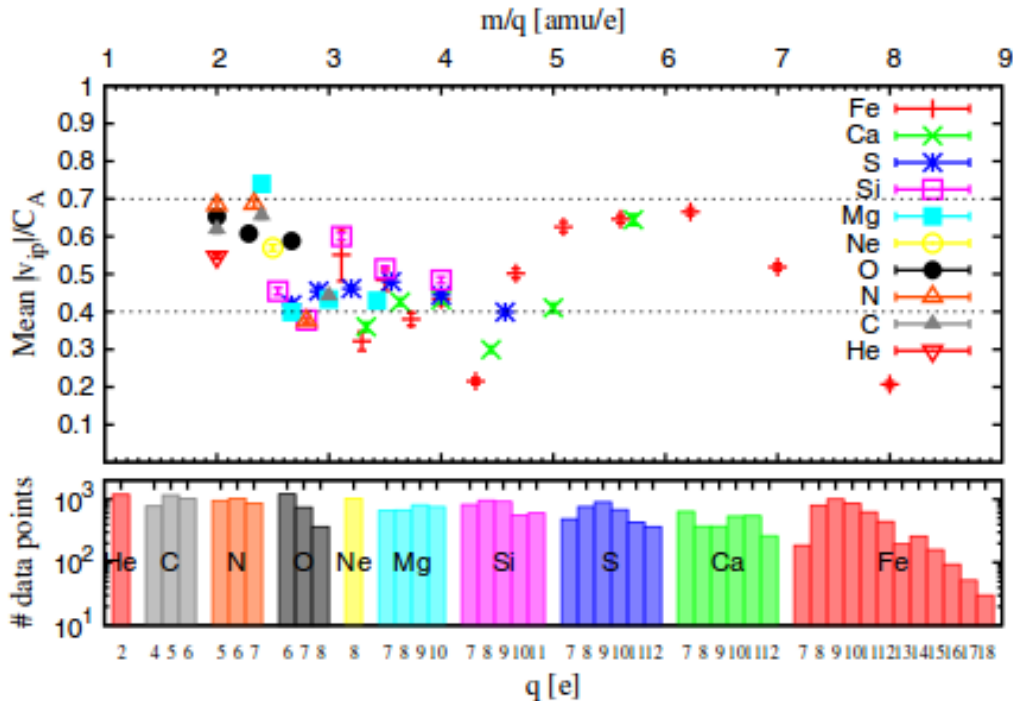


FIGURE 7.2: Differential streaming measured with ACE/SWICS in the fast solar wind at L1 in early 2008. The figure is taken from [31].

iron ions centered around the obtained mean charge state  $\text{Fe}^{10+}$  in the fast coronal-hole associated wind (see column 4 and 5 of the table in figure [46]). These measurements were obtained from two short time intervals of about 4 to 5 hours and represent the mean iron velocities for the whole time intervals which are then compared to the average proton speeds of 624 and 669 km/s, respectively. The obtained velocity differences (row 4 of the table) were then also corrected for the mean interplanetary B-field orientation. The resulting speed differences (row 5 of the table) can be compared to the mean Alfvén speed (row 6 of the table) during the measurement periods. They obtain values for the differential streaming relative to the Alfvén speed of  $v_{\text{diff}}/v_A \approx 1.3$  and  $v_{\text{diff}}/v_A \approx 1.2$  which are both slightly larger than 1. Unfortunately we cannot compare

TABLE 1. Solar Wind Characteristics for Selected Time Periods

	Sept. 29, 1978 0828–0920	Sept. 29, 1978 1105–1400	Sept. 28, 1978 1500–2020	Dec. 18, 1978 0805–1200
Solar wind flow type	driver plasma	driver plasma	coronal hole	coronal hole
$v_H$ , km/s	865	799	624	669
$v_{Fe}$ , km/s	865	800	700	850
$ v_{Fe}  -  v_H $ , km/s	0	1	76	181
$ v_{Fe} - v_H $ , km/s	$0 \pm 40$	$5 \pm 40$	$80 \pm 10$	$230 \pm 20$
$v_A$ , km/s	210	210	60	190
$T_{K_{in}}(H)$ , $10^4$ K	7	8	20	60
$n_H$ , cm $^{-3}$	5.5	2.8	3.1	4.2
$n_{Fe}$ , $10^{-6}$ cm $^{-3}$	740	280	100	140
$n_{Fe}/n_H$ , $\times 10^6$	135	100	32	33
$T_c(\text{Fe})$ , $10^6$ K*	3.0	4.0	1.5	1.4
$T_c(\text{Fe})$ , $10^6$ K†	3.8	5.0	1.4	1.3

\*Using *Jordan* [1969, 1970].

†Using *Shull and Van Steenberg* [1982].

FIGURE 7.3: Differential streaming measured with ISEE-3/ULECA in two fast solar wind streams at L1 in September and December 1978. The table is taken from [46]

directly our results to these former studies since we cannot correct our measurements for the varying direction of the magnetic field nor can we relate the absolute velocity differences to the ambient Alfvén speed because there are no in-situ B-field measurements provided by SOHO due to the lack of a magnetometer aboard<sup>1</sup>. Nevertheless assuming an average local Alfvén speed around 50 km/s as discussed in chapter 1 and taking into account that we also only measure a projection of the velocity difference, for which the absolute value is always smaller than the absolute value of the actual differential streaming, we can make the statement that the observed differential streaming in the fast solar wind around  $v_{\text{proton}} \approx 500$  km/s for all investigated ions in this work

<sup>1</sup>An extrapolation of the B-field from the WIND spacecraft could help out here but this is rather experimental since the extrapolation quality is expected to drop significantly with the distance of the two spacecraft and WIND did not reach its final orbit around L1 before November 1996 when CTOF was already out of nominal operation for more than 2 months.

is on the order of a substantial fraction of the Alfvén speed which could be also even larger than 1. Therefore, we can roughly confirm the measurements of [31] and [46] but cannot give more precise values for the differential streaming nor favor one of the measurements, even if our study has the best time resolution of the three compared studies.

## Appendix A

### *SRIM/TRIM Tables and Plots*

```
=====
SRIM-2013.00 =====
=====
= Ion Energy vs Position File =
=====
= AXIS DEFINITIONS: X=Depth. Y,Z= Lateral plane of target surface.=
= (If beam enters target at an angle, this tilt is in Y direction)=
= Shown are: Ion Number, Energy (keV), X, Y, Z Position =
=====
= CALCULATION DATA =
Ion Data: Name, Mass, Energy . Energy Interval
He    004.00  60keV   10000ev
=====

```

Ion Number	Energy (keV)	Depth (x) (Angstrom)	Y (Angstrom)	Z (Angstrom)	Electronic Stop.(ev/A)	Energy Lost to Recoil(ev)
0000001	6.0000E+01	0.0000E+00	0.0000E+00	0.0000E+00	1.5414E+01	0.0000E+00
0000001	4.6383E+01	6.5526E+02	-1.1827E+01	8.7548E-01	1.3175E+01	1.0323E+01
0000001	3.9107E+01	1.2132E+03	-5.2514E+01	2.4140E+01	1.1844E+01	9.0716E+00
0000001	2.9346E+01	1.8583E+03	-1.4600E+02	1.0807E+02	9.8753E+00	1.0168E+01
0000001	1.9473E+01	2.9754E+03	-3.3209E+02	5.0100E+02	7.6337E+00	5.9579E+00
0000001	9.9862E+00	4.1146E+03	-7.7275E+02	1.0990E+03	5.3589E+00	2.7382E+01
0000001	0.0000E+00	5.5775E+03	-4.5133E+02	1.2940E+03	0.0000E+00	5.2107E-01
0000002	6.0000E+01	0.0000E+00	0.0000E+00	0.0000E+00	1.5414E+01	0.0000E+00
0000002	4.7386E+01	9.3202E+02	-2.0321E+01	-1.5184E+01	1.3350E+01	6.1074E+00
0000002	3.9510E+01	1.4863E+03	-3.5725E+01	-5.2915E+01	1.1921E+01	8.8914E+00
0000002	2.8433E+01	2.2949E+03	-1.0400E+02	-1.8177E+02	9.6787E+00	2.2936E+03
0000002	1.8914E+01	3.1714E+03	-5.1773E+02	2.4449E+02	7.5009E+00	1.2377E+01
0000002	9.2224E+00	4.6976E+03	-9.5288E+02	5.8591E+02	5.1517E+00	1.1479E+01
0000002	0.0000E+00	6.0669E+03	-4.8368E+02	6.2763E+02	0.0000E+00	4.1908E-01
0000003	6.0000E+01	0.0000E+00	0.0000E+00	0.0000E+00	1.5414E+01	0.0000E+00
0000003	4.9382E+01	8.6780E+02	-2.5612E+01	2.1211E+01	1.3694E+01	1.4650E+01
0000003	3.7279E+01	1.6101E+03	-3.3428E+01	1.2764E+02	1.1493E+01	4.2681E+02
0000003	2.8905E+01	3.0850E+03	-1.5173E+02	6.6572E+02	9.7807E+00	5.0784E+00
0000003	1.9234E+01	4.0931E+03	-8.4126E+01	9.5358E+02	7.5771E+00	1.0954E+01

FIGURE A.1: Exemplary EXYZ-TRIM output file for helium ions with initial energy of 60 keV. Here the selected energy increment is  $E_{inc} = 10$  keV and thus relatively large to show the tracking of different ions.

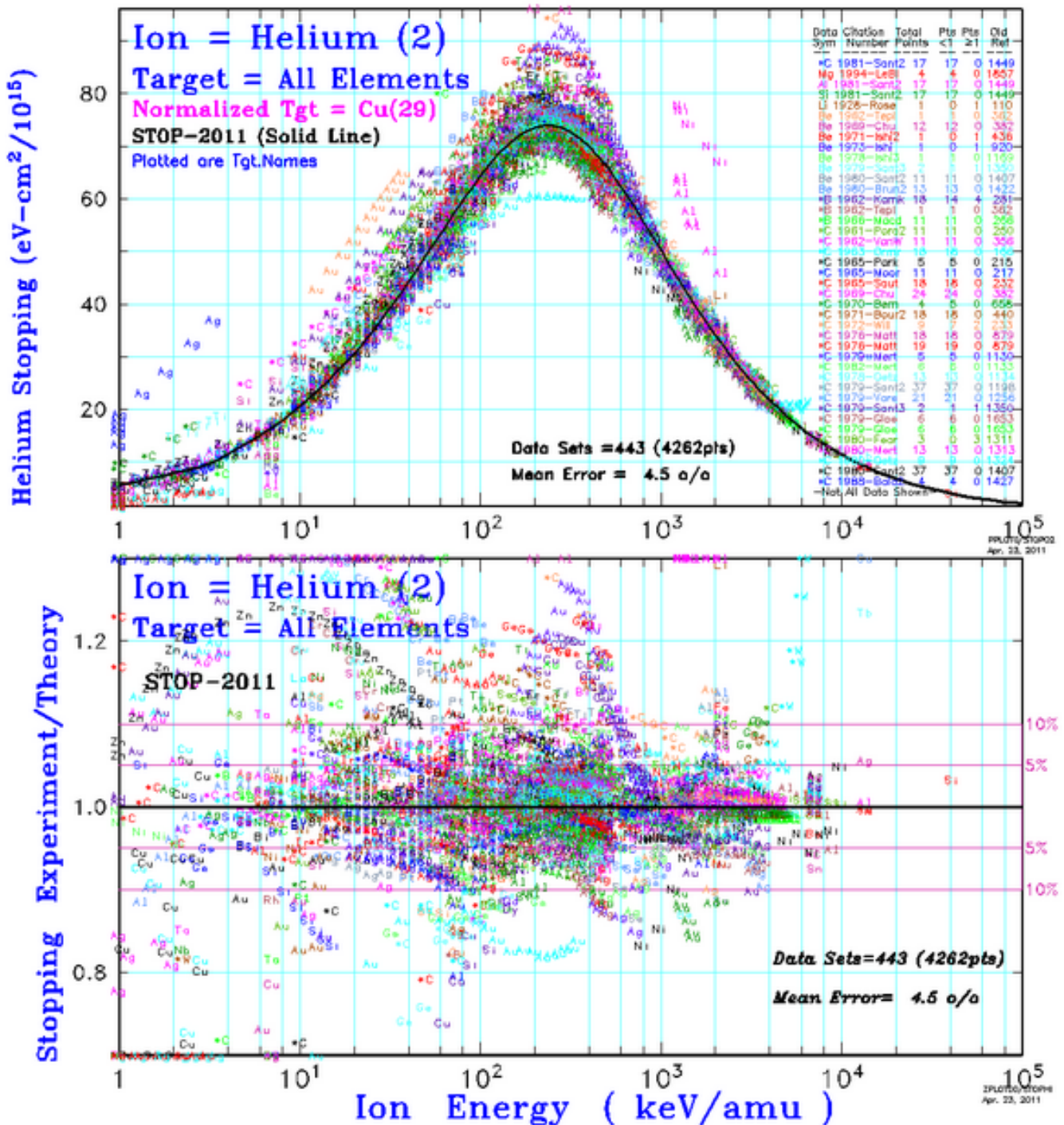


FIGURE A.2: Comparison of the theoretically calculated stopping power by TRIM (solid black line) and performed stopping power measurements for helium ions in different targets. The diagram is taken from the official SRIM/TRIM website [47].

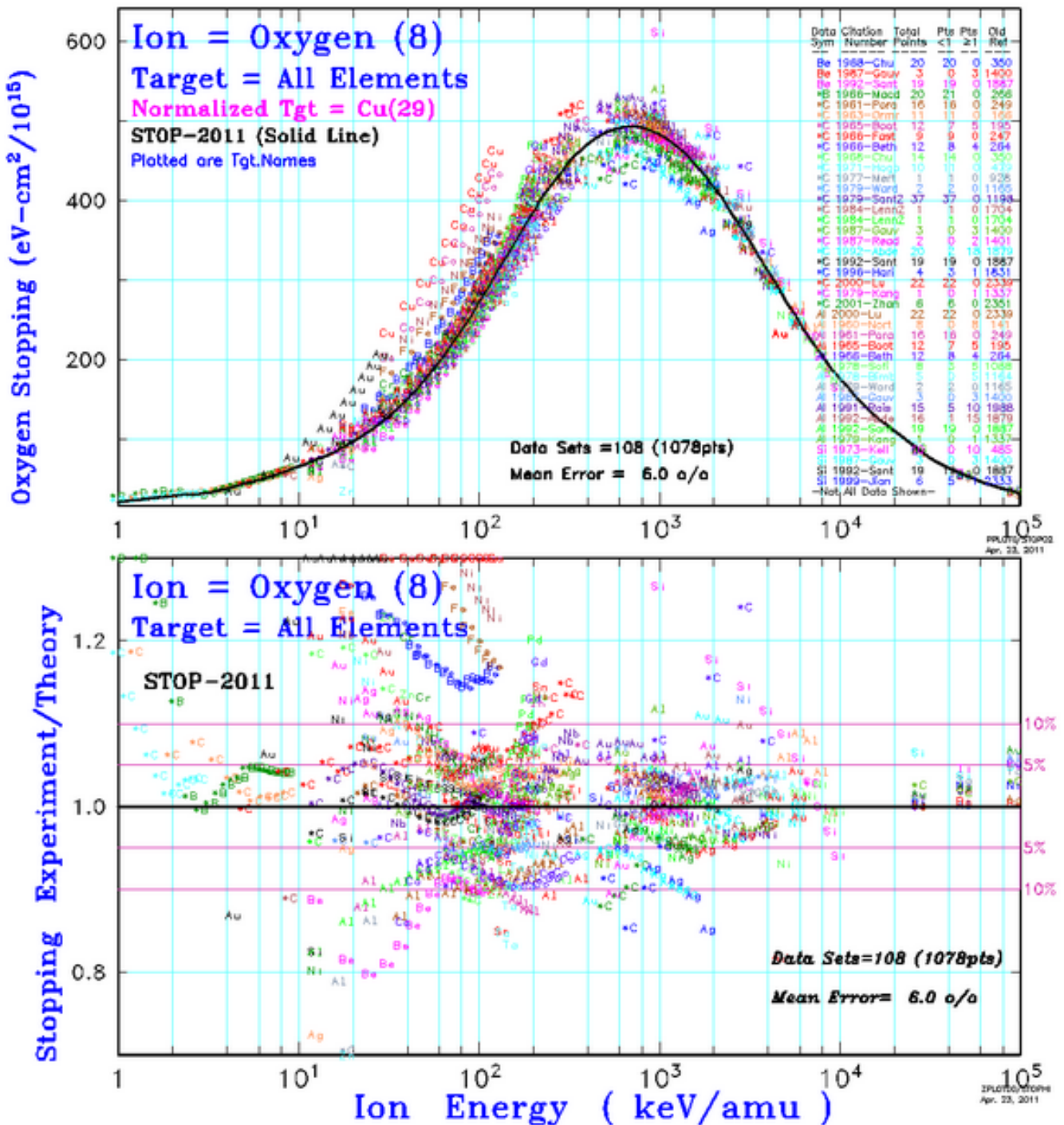


FIGURE A.3: Comparison of the theoretically calculated stopping power by TRIM (solid black line) and performed stopping power measurements for oxygen ions in different targets. The diagram is taken from the official SRIM/TRIM website [47].

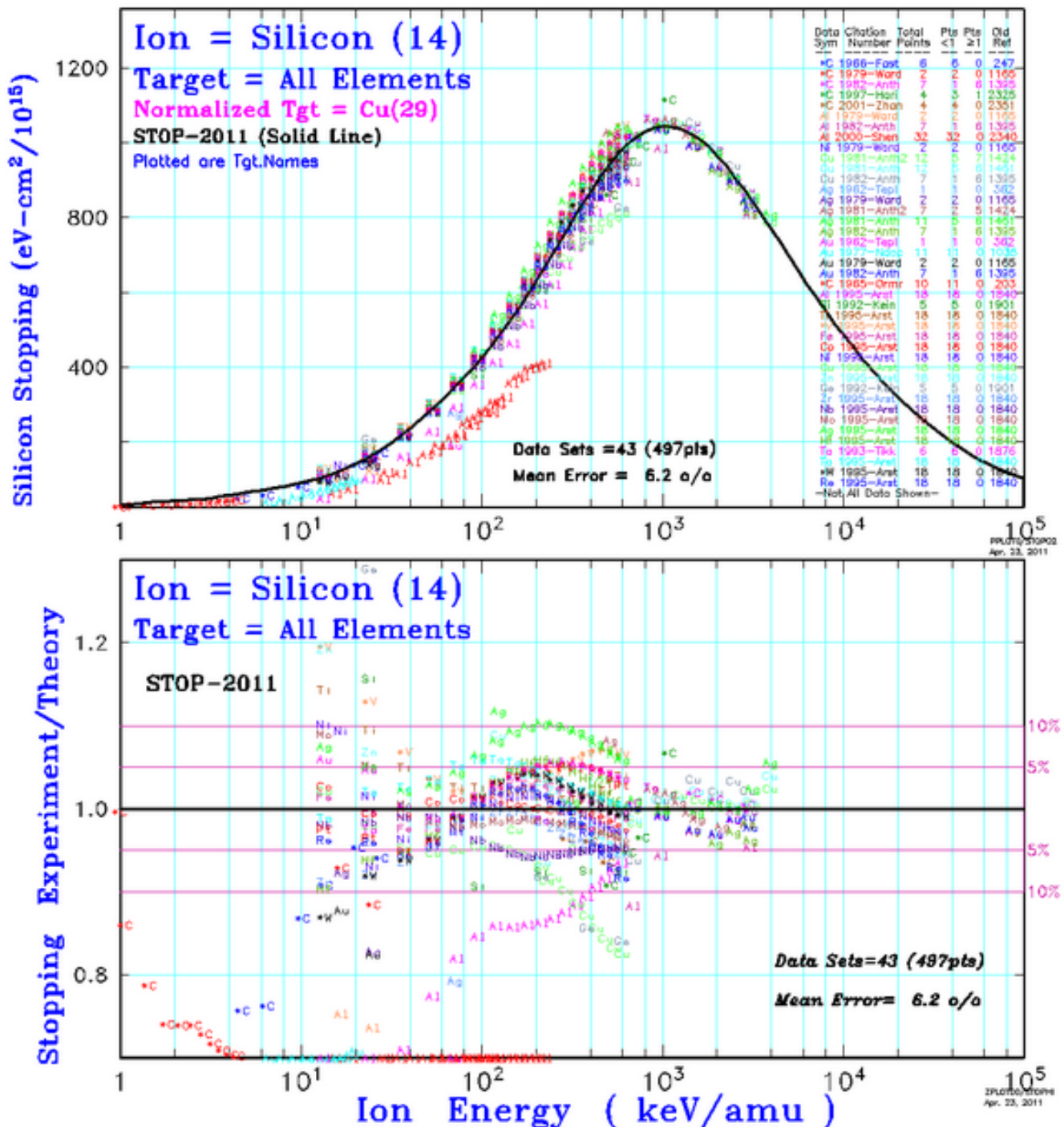


FIGURE A.4: Comparison of the theoretically calculated stopping power by TRIM (solid black line) and performed stopping power measurements for silicon ions in different targets. The diagram is taken from the official SRIM/TRIM website [47].

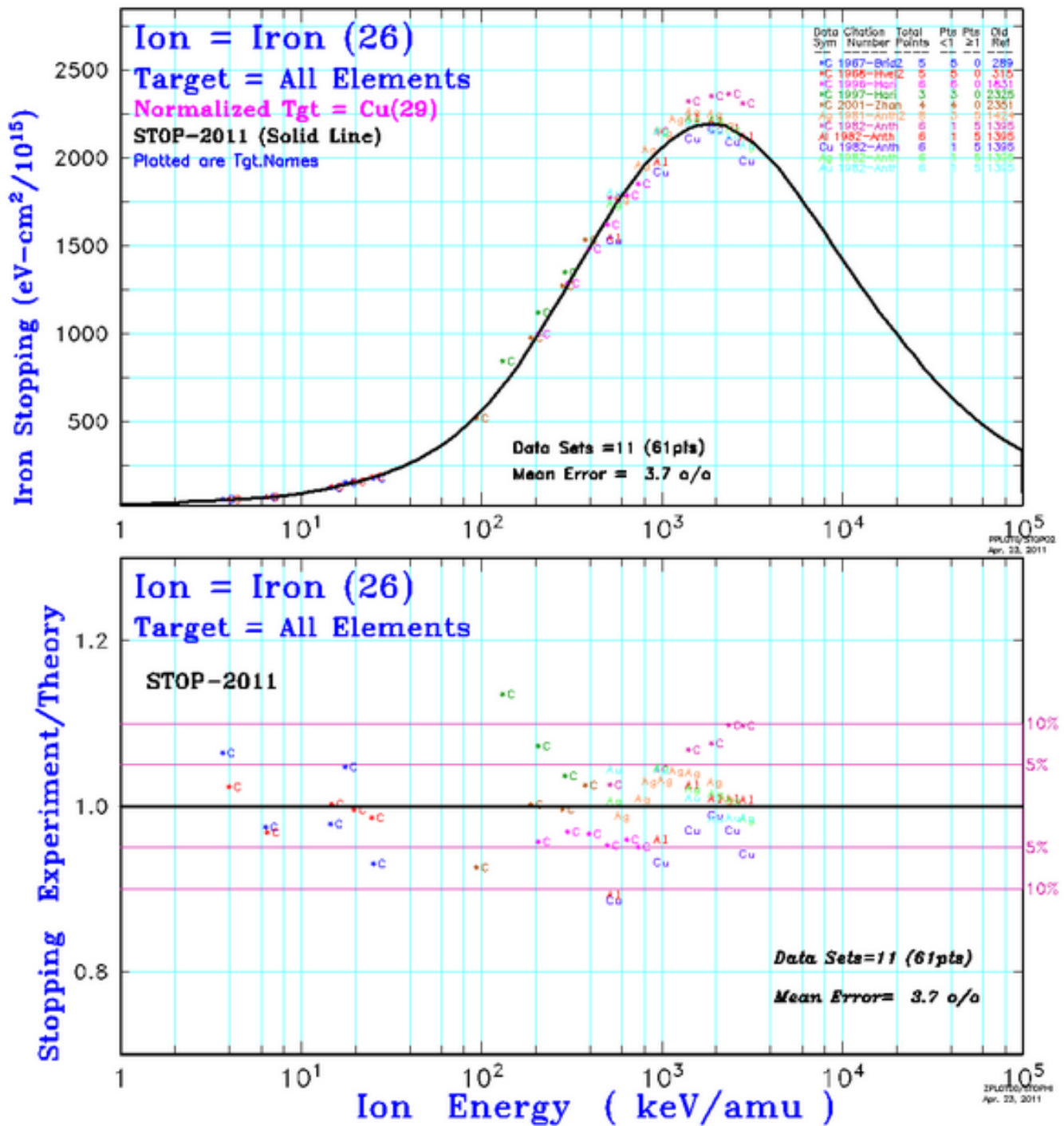


FIGURE A.5: Comparison of the theoretically calculated stopping power by TRIM (solid black line) and performed stopping power measurements for iron ions in different targets. The diagram is taken from the official SRIM/TRIM website [47].

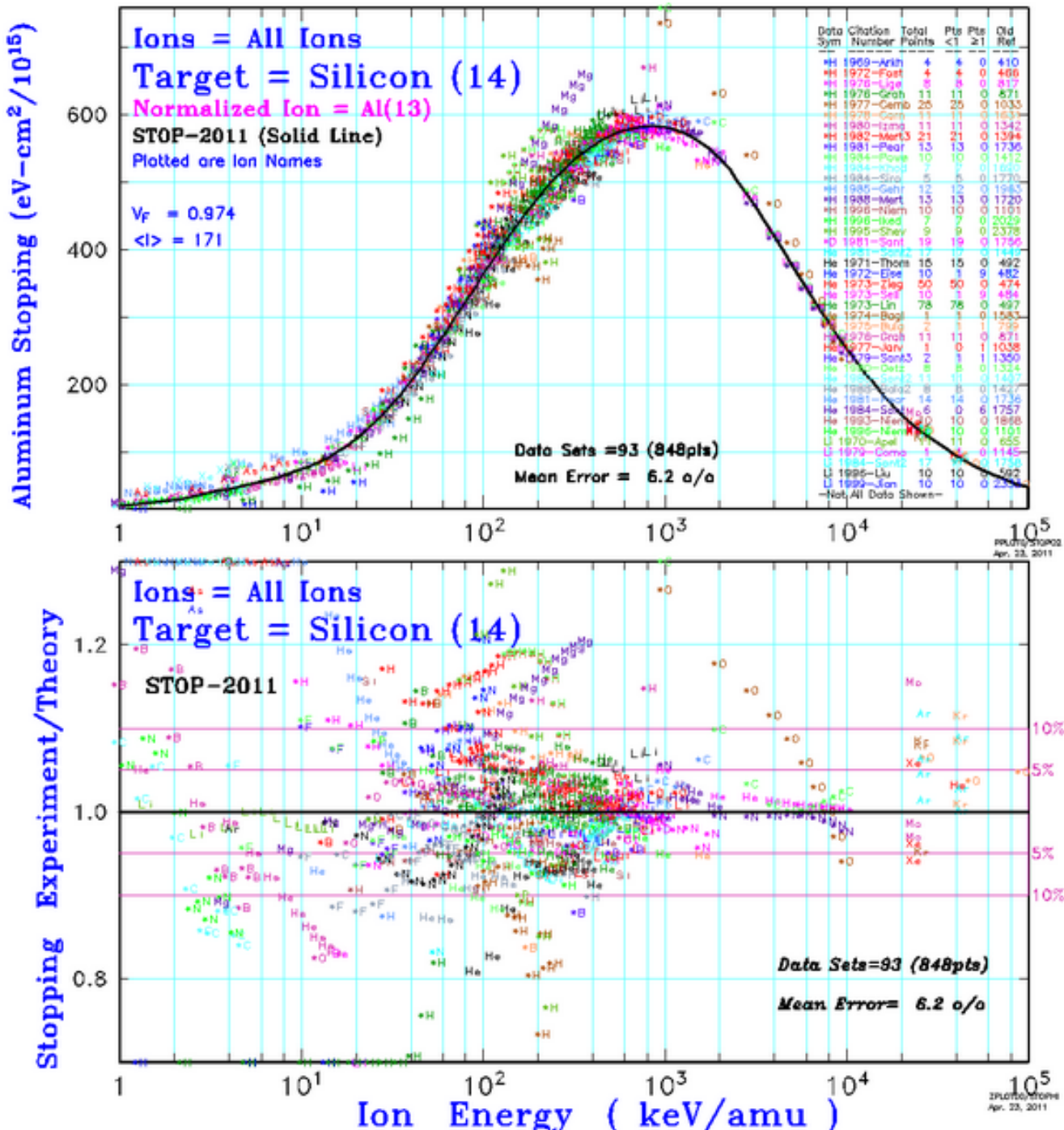


FIGURE A.6: Comparison of the theoretically calculated stopping power by TRIM (solid black line) and performed stopping power measurements for a silicon target and different incident ion species.

The diagram is taken from the official SRIM/TRIM website [47].

# Bibliography

- [1] L. Biermann, *Kometenschweife und Solare Korpuskularstrahlung.* Z. Astrophys., 29, 274 – 286, (1951)
- [2] K. I. Gringauz, V. V. Bezrukikh, V. D. Ozerov, and R. E. Rybchinskyi, *Study of the Interplanetary Ionized Gas, High Energy Electrons, and Solar Corpuscular Radiation by Means of Three Electrode Traps for Charged Particles on the Second Soviet Cosmic Rocket.* Soviet Physics Doklady, 5, 361 – 364, (1960)
- [3] M. M. Neugebauer, C. W. Snyder, *The Mission of Mariner II: Preliminary Observations. Solar Plasma Experiment.* Science 138: 1095–1096, (1962)
- [4] M. M. Neugebauer, C.W. Snyder, *Mariner 2 Observations of the Solar Wind. 1. Average Properties.* J. Geophys. Res. 71: 4469–4484, (1966)
- [5] S. J. Bame , A. J. Hundhausen, J.R. Asbridge, I.B. Strong, *Solar Wind Ion Composition.* Phys. Rev. Lett. 20: 393–395, (1968)
- [6] J. Geiss, F. Bühler , H. Cerutti, P. Eberhardt, C. Filleux, *Solar Wind Composition Experiment.* Apollo 16 Prel. Sci. Rep. NASA Spec. Publ. 315(14): 14.1–14.10, (1972)
- [7] P. Eberhardt, J. Geiss , H. Graf, N. Grögler, U. Krähenbühl, H. Schwaller, J. Schwarzmüller, *Trapped Solar Wind Noble Gases, Exposure Age and K/Ar-Age in Apollo 11 Lunar Fine Material.* Proc. Apollo. 11. Lunar Sci. Conf. 2: 1037–1070, (1970)
- [8] U. Feldman, et al., *Coronal Composition above the Solar Equator and the North Pole as Determined from Spectra Acquired by the SUMER Instrument on SOHO.* The Astrophysical Journal 505, pp. 999-1006, (1998)
- [9] A. B. Galvin, et al, *Solar Wind Composition: First Results from SOHO and Future Expectations.* Bulletin of the American Astronomical Society, Vol. 28, p.897, (1996)
- [10] P. Bochsler, *Minor Ions in the Solar Wind,* Astron. Astrophys. Rev. (2007)
- [11] G. Proelss, *Physik des Erdnahen Weltraums.* Springer Lehrbuch; 2. Aufl., S. 287-360, (2004)

- [12] U. Feldman, E. Landi, N. A. Schwadron, *On the Sources of Fast and Slow Solar Wind.* Journal of Geophysical Research 110 (A7): A07109.1–A07109.12. (2005)
- [13] S. Bravo; G. A. Stewart, *Fast and Slow Wind from Solar Coronal Holes.*, The Astrophysical Journal, Volume 489, Issue 2, pp. 992-999, (1997)
- [14] T. Sakao, R. Kano, N. Narukage, J. Kotoku, T. Bando, E. E. DeLuca, L. L. Lundquist, S. Tsuneta, L. K. Harra, Y. Katsukawa, et al. *Continuous Plasma Outflows from the Edge of a Solar Active Region as a Possible Source of Solar Wind.* Science, 318, (2007a), 1585, (2007)
- [15] R. von Steiger, N. A. Schwadron, L. A. Fisk, J. Geiss, G. Gloeckler, S. Hefti, B. Wilken, R. F. Wimmer-Schweingruber, T. H. Zurbuchen, *Composition of Quasi-Stationary Solar Wind Flows from Ulysses/Solar Wind Ion Composition Spectrometer.* Journal of Geophysical Research, Volume 105, Issue A12, p. 27217-27238, (2000)
- [16] R. F. Wimmer-Schweingruber, *Physik VI, Plasmaphysik und Extraterrestrische Physik, Teil II - Extraterrestrische Physik, Skriptum zur Vorlesung.* Sommersemester 2008 und 2011, [http://www.ieap.uni-kiel.de/et/people/wimmer/teaching/Phys\\_VI/Phys\\_VI\\_teil\\_2.pdf](http://www.ieap.uni-kiel.de/et/people/wimmer/teaching/Phys_VI/Phys_VI_teil_2.pdf), Dezember (2014)
- [17] S. Suess (NASA/MSFC), *Sun's spiraling magnetic field from a vantage point 100 AU from the Sun.*, <http://spaceweather.com/glossary/images/spiralfield.jpg>, December (2014)
- [18] E. N. Parker, *Dynamics of the Interplanetary Gas and Magnetic Fields.* Astrophys. J, 128, 664 – 676, (1958)
- [19] E. Marsch, *MHD Turbulence in the Solar Wind.* Physics of the Inner Heliosphere, Vol. 2: Particles, Waves and Turbulence, Vol. 20 of Physics and Chemistry in Space, Springer (1991b), pp. 159–241, (1991)
- [20] E. Marsch, *Kinetic Physics of the Solar Wind Plasma.* Physics of the Inner Heliosphere, Vol. 2: Particles, Waves and Turbulence, Vol. 20 of Physics and Chemistry in Space, Springer (1991a) pp. 45–133, (1991)
- [21] E. Marsch, K.-H. Mühlhäuser, R. Schwenn, H. Rosenbauer, W.G. Pilipp , F.M. Neubauer, *Solar wind protons: Three-Dimensional Velocity Distributions and Derived Plasma Parameters Measured Between 0.3 and 1 AU.* Journal of Geophysical Research (1982c), 87, 52–72, (1982)
- [22] W.I. Axford, J.F. McKenzie, *The Origin of High Speed Solar Wind Streams.* Solar Wind, Seven, (Eds.) Marsch, E., Schwenn, R., Proceedings of the 3rd COSPAR Colloquium

held in Goslar, Germany, 16–20 September 1991, Vol. 3 of COSPAR Colloquia Series, pp. 1–5, Pergamon Press USA, (1992)

- [23] W.I. Axford, J.F. McKenzie, *The Solar Wind*. in *Cosmic Winds and the Heliosphere*, (Eds.) Jokipii, J.R., Sonett, C.P., Giampapa, M.S., Space Science Series, pp. 31–66, Arizona University Press, Tucson, U.S.A (1997)
- [24] E. Marsch, *Kinetic Physics of the Solar Corona and Solar Wind*. Living Rev. Solar Phys., 3, (2006), 1. [Online Article]: cited [December 2014], <http://www.livingreviews.org/lrsp-2006-1> December (2014)
- [25] C.-Y. Tu, E. Marsch, *Two-fluid Model for Heating of the Solar Corona and Acceleration of the Solar Wind by High-Frequency Alfvén Waves*. Solar Phys., 171, 363–391, (1997)
- [26] E. Marsch, C.-Y. Tu, *The Effects of High-Frequency Alfvén Waves on Coronal Heating and Solar Wind Acceleration*. Astron. Astrophys., 319, L17–L20, (1997)
- [27] C.-Y. Tu , E. Marsch, *MHD Structures, Waves and Turbulence in the Solar Wind: Observations and Theories*. Space Sci. Rev., 73, 1–210, (1995)
- [28] B. Tsurutani, G. S. Lakhina *Some Basic Concepts of Wave-Particle Interactions in Collisionless Plasmas*. Reviews of Geophysics, Volume 35, Issue 4, p. 491-501, (1997)
- [29] W. Baumjohann, R. A. Treumann, *Basic Space Plasma Physics*. Imperial College Press, Revised Edition, p. 279-286 and p. 336, (2012)
- [30] M. Aschwanden, *Physics of the Solar Corona, An introduction with Problems and Solutions*, Springer, (2005)
- [31] L. Berger, *Systematic Measurements of Ion-Proton Differential Streaming in the Solar Wind*. Physical Review Letters, 106, 151103, 2011
- [32] S. Hefti, *Kinetic Properties of Solar Wind Minor Ions and Protons Measured with SOHO/CELIAS*. Journal of Geophysical Research, Vol. 103, No. A12, Pages 29,697–29,704, December (1998)
- [33] D. Hovestadt, M. Hilchenbach, A. Borgi, B. Klecker, P. Laeverenz and M. Scholer, H. Grünwald, W. I. Axford, S. Livi, E. Marsch, B. Wilken and H. P. Winterhoff, F. M. Ipavich, P. Bedini, M. A. Coplan, A. B. Galvin and G. Gloeckler, P. Bochsler, H. Balsiger, J. Fischer, J. Geiss, R. Kallenbach and P. Wurz, *CELIAS - Charge Element and Isotope Analysis System for SOHO*. Solar Physics, Volume 162, Issue 1-2, pp. 441-481, December (1995)
- [34] S. Hefti, *Solar Wind Freeze-in Temperatures and Fluxes Measured with SOHO/CELIAS/CTOF and Calibration of the CELIAS Sensors*. PHD Thesis, University of Bern, Switzerland (1997)

- [35] M. Aellig, *Freeze-in Temperatures and Relative Abundances of Iron Ions in the Solar Wind Measured with SOHO/CELIAS/CTOF*. PHD Thesis, University of Bern, Switzerland , (1998)
- [36] M. Stalder, *Auflösungsvermögen bei der Energiemessung von Silizium-Detektoren für Sonnenwind-Ionen und Berechnungen zur Mephisto Ionenquelle*, Diplom-Arbeit, Universität Bern, (2001)
- [37] M. Oetliker, *CTOF, A Solar Wind Time-of-Flight Mass Spectrometer with High Charge Resolution, Numerical Simulations and Calibrations*. PHD Thesis, University of Bern, (1993)
- [38] W. Brandt and M. Kitagawa, *Effective Stopping-power Charges of Swift Ions in Condensed Matter*, Physical Review 8 Vol. 25, Number 9, 1 May (1982)
- [39] J. F. Ziegler, J.P.Biersack, M.D. Ziegler, *SRIM The Stopping of Ions in Matter*, SRIM User Manual, SRIM Co., (2008)
- [40] A. Taut, *Pick-Up Ions at 1 AU*, Master Thesis, University of Kiel, Germany, (2014)
- [41] D. B. Reisenfeld, D.S. Burnett, R.H. Becker, T.H. Zurbuchen, *Elemental Abundances of the Bulk Solar Wind: Analyses from Genesis and ACE*, Space Sci. Rev., 130, 79-86, (2007)
- [42] J. Geiss, G. Gloeckler, R. von Steiger, H. Balsiger, L. A. Fisk, A. B. Galvin, F. M. Ipavich, S. Livi, J. F. McKenzie, K. W. Ogilvie, B. Wilken, *The Southern High-Speed Stream: Results from the SWICS Instrument on Ulysses*, Science, Vol. 268, 19, May (1995)
- [43] M. Oetliker, *Response of a Passivated Implanted Planar Silicon (PIPS) Detector for Heavy Ions with Energies between 25 and 360 keV*. Nuclear Instruments and Methods in Physics Research A 337, 145-148, (1993)
- [44] L. D. Landau, J. Exp. Phys. (USSR) 8, 201, (1944)
- [45] F. M. L. Almeida Jr., M. Barbi, *A Proposal for a Different Chi-Square Function for Poisson Distributions*. Nucl. Instr. Meth. A449, 383-395, (2000)
- [46] F. Ipavich, *Solar Wind Fe and CNO Measurements in High-Speed Flows*. Journal of Geophysical Research, Vol. 91, No. A4, Pages 4133-4141, April, (1986)
- [47] J. F. Ziegler, M.D. Ziegler, *Official SRIM Website*. <http://www.srim.org/>, December (2014)

## *Acknowledgements*

I would like to thank Prof. Dr. Robert F. Wimmer-Schweingruber for the interesting topic of this master thesis and for always having time and a friendly ear for my problems and questions. I thank Prof. Dr. Michael Bonitz for the interest in this work during and prior to my results talk. I would like to thank Dr. Lars Berger for the daily business of supervising my work, for many helpful discussions and that together with Dr. Christian Drews he made available the Python *dBdata class* with which many of the plots in this thesis were created. I thank my office colleague MSc. Andreas Taut for developing several useful python fit routines which were either directly used in this thesis or which could be extended by me to find solutions for the arising problems. I also thank Andreas for the many interesting scientific and non-scientific discussions we had together. I would like to thank Dr. Eckart Marsch for his comprehensive introductions to space plasma physics both in his lectures and in private discussions. Furthermore, I would like to thank all other members of the *Sonnenwind-Gruppe*: Dr. Verena Heidrich-Meisner, Dipl. Phys. Thies Peleikis, Dipl. Phys. Martin Kruse, MSc. Jia Yu and Dipl. Phys. Jan Steinhagen for the helpful and friendly atmosphere in the meetings but also in everyday life at the institute. I would like to thank Dr. Martin Hilchenbach and Dr. Heiner Grünwaldt for the helpful information about the CELIAS sensors during the meeting at the Max-Planck Institute for Solar System Research in August 2014.

I thank my fellow students of the first semester and who are now my friends Henning Lohf, Sebastian Zabel, Manuel Jung, Benthe Grun, Thorben Kewitz, Niklas Jepsen and Patrick Kühl for listening critically to all my talks and talk rehearsals during our studies and also for motivating or distracting me when physics became difficult. I would like to thank my girlfriend Alin Bähr for her love and patience even in times when I did not have so much time to share with her. I especially would like to thank my parents who, with their love and great care, gave me the possibility to study and who were always there for me.

**Erklärung gemäß Paragraph 9 Abs. 7. der Prüfungsverfahrensordnung der Christian-Albrechts-Universität zu Kiel für Studierende der Bachelor- und Master-Studiengänge**

Hiermit erkläre ich, dass ich die Masterarbeit selbstständig verfasst und keine anderen als die angegebenen Quellen und Hilfsmittel benutzt habe und die Arbeit in keinem anderen Prüfungsverfahren eingereicht habe.

Unterschrift:

---

Ort, Datum:

---